Topological chaos and chaotic mixing of viscous flows

Mohsen Gheisarieha

Dissertation submitted to the Faculty of the
Virginia Polytechnic Institute and State University
in partial fulfillment of the requirements for the degree of
Doctor of Philosophy
in
Engineering Mechanics

Mark A. Stremler, Chair
Hassan Aref
Daniel J. Inman
Mark R. Paul
Shane D. Ross

April 27, 2011
Blacksburg, Virginia

Keywords: Topological Chaos, Chaotic Mixing, Stokes Flow, Almost Invariant Sets,
Lobe Dynamics

Topological chaos and chaotic mixing of viscous flows

Mohsen Gheisarieha

ABSTRACT

Since it is difficult or impossible to generate turbulent flow in a highly viscous fluid or a microfluidic system, efficient mixing becomes a challenge. However, it is possible in a laminar flow to generate chaotic particle trajectories (well-known as *chaotic advection*), that can lead to effective mixing. This dissertation studies mixing in flows with the limiting case of zero Reynolds numbers that are called Stokes flows and illustrates the practical use of different theories, namely the *topological chaos theory*, the *set-oriented analysis* and *lobe dynamics* in the analysis, design and optimization of different laminar-flow mixing systems.

In a recent development, the topological chaos theory has been used to explain the chaos built in the flow only based on the topology of boundary motions. Without considering any details of the fluid dynamics, this novel method uses the Thurston-Nielsen (TN) classification theorem to predict and describe the stretching of material lines both qualitatively and quantitatively. The practical application of this theory toward design and optimization of a viscous-flow mixer and the important role of periodic orbits as "ghost rods" are studied.

The relationship between stretching of material lines (chaos) and the homogenization of a scalar (mixing) in chaotic Stokes flows is examined in this work. This study helps determining the extent to which the stretching can represent real mixing. Using a set-oriented approach to describe the stirring in the flow, invariance or leakiness of the *Almost Invariant Sets* (AIS) playing the role of ghost rods is found to be in a direct relationship with the rate of homogenization of a scalar. The mixing caused by these AIS and the variations of their structure are explained from the point of

view of geometric mechanics using transport through lobes. These lobes are made of segments of invariant manifolds of the periodic points that are generators of the ghost rods.

A variety of the concentration-based measures, the important parameters of their calculation, and the implicit effect of diffusion are described. The studies, measures and methods of this dissertation help in the evaluation and understanding of chaotic mixing systems in nature and in industrial applications. They provide theoretical and numerical grounds for selection of the appropriate mixing protocol and design and optimization of mixing systems, examples of which can be seen throughout the dissertation.

Dedication

For my parents.

Acknowledgments

I should state my special thanks to my advisor, Mark Stremler. I'm extremely grateful for your patience, for your knowledge and expertise in various scientific and technical areas, and for the freedom you gave me to explore many horizons of the astonishing world of nonlinear dynamics and mixing.

I'm also grateful for the help and constructive comments I received from Virginia Tech professors Hassan Aref, Shane Ross, Mark Paul, Ali Nayfeh and Daniel Inman and for all they taught me about dynamical systems and physics of fluids through the courses. Being familiar with those materials was crucial for the progress of this research.

I thank (former) ESM students Pankaj Kumar, Piyush Grover and Alireza Karimi for valuable discussions about theoretical and technical issues of this research and Matthew Bokulic, Kellen Shain, Alec Calhoun and Anthony Nelson for their nice experimental images of line stretching.

This work received support from the National Science Foundation (NSF) grant number DMS-0701126.

Contents

List of Figures

List of Tables

1

Introduction

1.1 Applications and importance of laminar flow mixing

Fluid mixing is important in understanding a wide range of natural systems, from inside biological cells to the stellar interiors [32]. Mixing influences many common processes that rely on fluid flows such as chemical reactions and heat transfer. Also, from a technological and economic view, mixing is an important part of many industrial processes such as: food industries [6], biotechnology [10, 29], concrete preparation, polymer and melted glass blending [56], energy and power generation and processing of chemicals including paints, coatings, synthetic rubbers and pharmaceuticals. Petroleum refinement, which is a vast industry, uses fluid mixing in generating uniform temperature distribution, blending different crude materials or additives, maintaining homogeneity for uniform specification, crude oil enhancement and upgrading [41].

Generating a turbulent flow, for instance by rotating an axial impeller in a vessel or stirring coffee using a spoon, is the most common approach to getting the appropriate fluid mixing in many applications. Turbulent mixing has been studied individually or as a component of other research works, a few of the related articles are [28, 21, 57]. However, it is not always physically possible or economically reasonable to generate turbulence. In many applications including those in the food, glass and polymer

industries, the fluid can be highly viscous and the mixers work at low speeds [56]. There are other applications like some biological processes in which the mixing has to be accomplished at low Reynolds numbers in order to keep the shear stress at low levels [10, 29].

Microfluidics as a rapidly developing branch of science and technology, is another arena for laminar flow mixing. Mixing is an important part of the process in microchemistry, microbiology, disease diagnosis and genetics [68, 35, 10]. In microfluidic systems usually the small apparatus dimensions impose small Reynolds numbers i.e. laminar flows. Mixing is an important part of the process in these systems. Since turbulent flow is often impossible in micromixers, many applications rely on diffusion. Diffusion by itself is usually uneconomic because of being slow and inefficient but some types of stirring or layering can be done to make it economic. For example the main stream of two fluids A and B can be divided into many substreams so that the fluid layers come in contact with each other and an $ABABABAB...$ order is formed, making faster diffusion possible [11, 12]. Micromixing can be enhanced passively (that is, with no induced energy from outside) by using channels with specific designs to enhance mixing, or actively (that is, with added energy) by using stirrers, lid driven flow or electrokinetics [68, 35].

One important approach for mixing in laminar flows that is becoming more popular is generating chaotic particle trajectories [3, 4, 51, 50]. This approach can result in surprisingly fast homogenization and mixing of viscous and slow flows as it can be observed throughout this dissertation. Similar to the layering of miscible fluids for diffusion enhancement, chaos causes the trajectories of particles of different miscible fluids to become layered up to very small scales. This layering due to stretching and folding of material lines happens at an exponential rate as a characteristic of chaotic systems, making it possible to design fast and efficient mixing systems while performing at low speeds or small dimensions.

1.2 Chaotic advection

Mixing in general consists of three steps, the first step being stretching of the substance in one direction and attenuation in another direction and the second step, folding the material upon itself [51, 50, 66]. These two steps are due to bulk motion of fluid. In miscible fluids, molecular diffusion is the third step. The stretching and folding mechanism of chaos can be a greatly effective tool for enhancing mixing in the first and second steps [4, 50]. In all the aforementioned applications where mixing has to be accomplished at low Reynolds numbers, and diffusion by itself is not fast enough, generating chaotic laminar flows is a reasonable approach [68, 43, 15]. It is well known that laminar flows can produce chaotic Lagrangian trajectories of passive particles, the theory being introduced by Aref under the name of "chaotic advection" [3]. Passive particles can be the fluid particles or particles of a second tracer fluid; they neither perturb the flow nor diffuse themselves. These particles move passively with the flow so that their dynamics is the same as that of the fluid elements. Thus, their equations of motion in Lagrangian form can be written as

$$\begin{aligned} \frac{dx}{dt} &= u(x,y,z,t), \\ \frac{dy}{dt} &= v(x,y,z,t), \\ \frac{dz}{dt} &= w(x,y,z,t), \end{aligned} \tag{1.1}$$

where u, v and w are cartesian components of the fluid velocity field $\mathbf{u}$. This dissertation studies incompressible flows at vanishing Reynolds numbers, known as Stokes flows. The velocities u and v are taken to be time-periodic nonlinear functions; therefore the system of equations 1.1 is a three-dimensional dynamical system capable of having chaotic solutions [3]. For a two-dimensional incompressible flow a streamfunc-

tion ψ exists so that

$$\begin{aligned} \frac{dx}{dt} &= -\frac{\partial \psi}{\partial y} \\ \frac{dy}{dt} &= \frac{\partial \psi}{\partial x} \end{aligned} \tag{1.2}$$

which resembles the structure of Hamilton's equations of motion with ψ acting the role of Hamiltonian. The Hamiltonian (ψ) is periodically time-dependent, which means that the dynamical system, while having an area-preserving stroboscopic map of the plane, is not generally integrable.

Chaotic advection, after being introduced by Aref in 1984, has been studied and utilized as a subtopic of fluid mechanics in many theoretical and experimental research works. Its immediate application is study of transport and mixing in Stokes flows, a few examples of which are the eccentric journal bearing flow [38, 9] or more generally the rod-stirring mixers (the "batch" stirring devices) [9, 27, 31, 25, 30, 24], different variations of the cavity flow [15, 40, 62, 13, 65] and pulsed source-sink devices [37, 63]. As micro-systems started to gain scientific and technological popularity, a great application of chaotic advection appeared in micro-mixing. As mentioned before, most micro-fluidic flows are laminar, making the mixing a challenge. However advancements have been achieved in this field by generating chaotic particle trajectories using a variety of methods. A few examples are: passive mixing in microchannels [43], manufacturing of polymer micro-films [81], mixing in microvascular networks [69], a biofluidics stirrer built based on the source-sink flow [22] and an inline microfluidic mixing channel [64].

This dissertation studies the chaotic mixing of viscous flows using two categories of the mentioned flows as example systems or case studies: the rod-stirring systems (in which rods with prescribed velocity stir the flow) and a double-lid-driven cavity flow (flow in a rectangular domain driven by moving belts on the top and bottom) [65]. It will be illustrated in details that these systems, while operating at very low speeds and

dimensions, can produce efficient mixing using chaotic advection of passive particles.

1.3 Topological chaos and the Thurston-Nielsen Classification theorem

Chaotic advection of passive particles leads to chaotic stretching of material lines which itself is an important step of a mixing process [51, 50, 9]. The novel approach introduced by Boyland *et al.* (2000) [9] explains the stretching and folding of material lines in chaotic flows from a topological point of view. Their method, using the Thurston-Nielsen classification theorem [75], gives a powerful tool for predicting and analyzing existence and amount of chaos in stirring systems. This method is only based on the topology of motion of boundaries and does not depend on any detailed fluid flow calculations.

In order to characterize a periodic 2-dimensional n-stirrer motion e.g. the motion of n rods in Fig. 1.1) topologically, it can be represented by a physical braid on n strands as Fig. 3.18 shows for some example protocols. A *stirring protocol* defines the prescribed motion of rods with certain topology and geometry [9]. (Fig.3.18). The physical braid representing a stirring protocol consists of the stirrer trajectories in the (2+1)-dimensional space-time of the form $(x(t), y(t), t)$ for one period of the system (T), in which $x(t)$ and $y(t)$ are the coordinates of a rod at time t. T is the time required for all the stirrers to go back to their original position (Fig.3.18). From a topological point of view, only interchanges of strands in the braid matter. In order to have a mathematical description of the physical braid, a letter σ_i is assigned to each clockwise interchange of strands i and $i+1$ and a letter σ_i^{-1} to their counter-clockwise interchange. Composition of these letters as a braid word for multiple interchanges of strands represents the physical braid of the stirring protocol. In a 2-dimensional image of a physical braid such as the one shown in Fig. 3.18, interchanges of the strands and their sign could be determined by over- and under-crossings of the curves

showing the strands.

Moving the internal stirrers with certain topologies of stirrer trajectories in the (2+1)-dimensional space-time can braid the flow in a way that a significant complexity called "topological chaos" is obtained. Topological chaos is the complexity built in the flow due to topology of boundary motions, or equivalently "the complexity that cannot be removed by continuous deformation of the shape of the fluid region or by any fixed stirrer motion" [9]. Existence and amount of this complexity can be predicted by the Thurston-Nielsen classification theorem (hereafter TNCT).

In the context of fluid stirring the TNCT can be stated as follows. A combination of stirrer motions, i.e. a braid, generates a mapping from the fluid domain to itself, which is isotopic (continuously deformable) to one of the following three classes:

(i) Finite order: the n^{th} iterate is the identity. In this kind of motion, the material lines are stirred in a topologically trivial way in the sense that they can be deformed back to their original position by continuous deformation of the boundaries while the stirrers are fixed in place but they are allowed to rotate. All the n-strand braids with $n < 3$ generate finite order mappings.

(ii) Pseudo-Anosov: topologically chaotic cases where the motion is complex enough to prevent the stirred material line from going back to its original position by continuous deformation of the boundaries while the stirrers are fixed in place but they are allowed to rotate. In these cases chaotic Lagrangian trajectories exist and the theorem guarantees a quantitative lower bound of stretching rate (λ_{TN}) for non-trivial material lines[1].

(iii) Reducible: the mapping domain consists of sub-domains that show either finite order or pseudo-Anosov behavior.

In order to use the theorem to find the class and the lower bound of stretching for a protocol, the mapping generated by the protocol's braid can be stated by ma-

[1] A non-trivial line encircles or joins two of the stirring rods, joins one of the rods to the wall, or connects two wall locations while encircling one rod [9].

trices. For each braid letter there is a matrix representation and the braid word is mathematically characterized by the multiplication of matrices corresponding to its braid letters. According to the conclusions of TNCT, when the largest eigenvalue of the braid matrix of the protocol is a real number greater than one, the braid is pseudo-Anosov and there exists at least one material line with a stretching rate equal to or greater than this number. Otherwise, the braid is finite order, and no lower bound of stretching is guaranteed for this case [9].

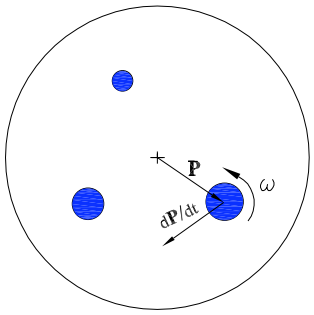

Figure 1.1: Generic rod-stirring device ("batch stirring device")

The approach of Boyland *et al.* has been used in a variety of research works to study line stretching of chaotic mixing systems from the topological view and to optimize these systems (see for example [80, 70, 71, 72, 24]). It has been extended to "ghost rods" [31, 62, 73, 14, 65] (see section 1.6), spatially periodic mixers [25] and three dimensional flows [14].

Chapter 3 illustrates in detail how this method is applied to a variety of rod-stirring protocols that are industrially and dynamically interesting (Fig.1.1) and the practical use of this abstract theory in the design and analysis of stirring protocols is studied. Also chapter 6 presents a mixing optimization scheme for finding the optimum sequence of some given protocols and applies this scheme to a 3-rod stirring system as an example.

1.4 Numerical solution of Stokes flows

This dissertation studies the stirring problem of highly viscous fluids that cannot be mixed by generating a turbulent regime. The corresponding Reynolds numbers are usually very small. In the limit of a vanishing Reynolds number, and considering an incompressible Newtonian fluid, the fluid motion is a Stokes flow with the streamfunction $\psi(z, \bar{z})$ satisfying the biharmonic equation: $\nabla^4\psi = 0$ [39]. With $z = x + iy$ denoting the coordinates in the complex form, the velocity field is given by $u + iv = -2i\frac{\partial\psi}{\partial\bar{z}}$ which is the same as Eq.1.2. The solution has to satisfy the no-slip boundary conditions at the outer boundary of the domain and the boundaries of the stirring rods when solid rods stir the flow.

For the rod-stirring system of chapters 3 and 6 (Fig.1.1), the solution developed by Finn *et al.* in [26, 27] is used. Placing rotlet and Stokeslet singularities at the center of each rod and using the circle theorem to satisfy the boundary condition at the outer boundary, Finn *et al.* have presented a series solution for the stirring device of Fig. 1.1 of the form

$$\psi(z, \bar{z}) = \sum_{i=1}^{mn} A_i f_i(z) + \bar{A}_i \bar{f_i}(z) \tag{1.3}$$

for any instant of time. In the above equation m is the number of rods and n is the number of required terms in the series to get accurate results. In order to track the passive fluid particle trajectories, the ODEs 1.2 should be integrated. It is evident from these nonlinear non-autonomous advection equations that the flow is generally non-integrable and capable of generating chaotic trajectories [3]. When the boundary conditions are periodic in time (e.g. all the flows studied in this dissertation), the velocity field is periodic and it is enough to determine it for one period of the flow.

For the cavity flow of chapters 4 and 5, the solution developed by [65] and [13] based on the scheme of [49] is used. For the chosen boundary conditions, this solution of the biharmonic equation is a closed-form solution (Eq. 4.4). These solutions enable

tracking of passive particles as well as non-trivial material lines consisting of passive particles. The material line is initially represented by a number of particles. Because of the exponential divergence of trajectories in chaotic systems, the distance between adjacent particles grows very fast. For line tracking simulations, in order to see the line's fine structures and accurately calculate the length of the stretched line, a point-insertion algorithm is needed to maintain the distance between adjacent points on the line below a desired minimum.

1.5 Chaos and mixing measures

The numerical solution for the systems considered here, makes it possible to calculate the topological entropy [1, 2] and the largest lyapunov exponent [52] as two major measures of complexity in a flow. For the systems that the stretching of material lines is exponential i.e.

$$\frac{L_{t+t_0}}{L_{t_0}} \simeq \lambda^{\frac{t}{T}}, \tag{1.4}$$

with T denoting the period of the flow. λ is the stretching rate of the system [51]. Once the stretching is simulated numerically, the topological entropy of the flow can be calculated directly from the stretching rate as

$$h = \ln(\lambda), \tag{1.5}$$

(see [70]) or equivalently

$$L_{t_0+nT} \simeq L_{t_0} e^{hn}. \tag{1.6}$$

h is always larger than the topological lower bound (h_{TN}) predicted by TN theorem for the corresponding braid.

Lyapunov Exponent (LE) is another measure of chaos in a system that is defined as [5, 67]

$$\sigma(\mathbf{x}) = \lim_{t\to\infty, d(0)\to 0} \frac{1}{t} \ln \frac{d(t)}{d(0)} \tag{1.7}$$

for a trajectory $\mathbf{x}$ and a nearby trajectory with an initial distance $d(0)$ from $\mathbf{x}$. Physically, $\sigma(\mathbf{x})$ is the exponent with which two adjacent particles separate from each other. The value of $\sigma(\mathbf{x})$, computed for a large but finite time, depends slightly on the trajectory, therefore an average of $\sigma(\mathbf{x}_i)$ for a grid of initial conditions is considered as the Lyapunov exponent (LE) of the system.

The length of a stirred non-trivial material line is dominated by the stretching in the most unstable directions so that the converged stretch rate represents the exponential divergence of particles of the unstable foliation. While in the calculation of LE, the trajectory travels all over the chaotic sea, and the result is an average of stretching for the whole area including the stable and unstable foliations [23]. As a result, the value of LE is always lower than h_f and a smaller difference between the two numbers (larger LE) is a sign of more uniformly distributed stretching.

The TNCT (section 1.3) quantifies the chaos in a flow in terms of line stretching. In order to associate the stretching results to fluid mixing, the homogenization of passive scalar represented by a dense box of particles advected by the flow [18, 45, 53, 66] can be simulated and measured. Simulation of stirring of a box of particles gives a numerical visualization of the experimental homogenization of a blob of dye in the viscous fluid that is closer to the 'real' mixing than simulation of line stretching. The experimental streak of dye is a dense *blob* of particles and gets stirred for a finite number of periods; similar to the mentioned simulation. Whereas in the numerical simulation of stretching, a *line* of particles is usually tracked for a few periods (due to expensive computation) and in the computation of the Poincaré section *one particle* is tracked for a very long time.

The most common mixing measure in this context is the intensity of segregation which uses the variance of concentration of the tracer substance [18]. Practical implementation of this measure depends on the coarse-graining scale of the domain and cannot capture the effect of stirring in small scales. The newly developed multi-scale mixing measures, such as mix-norm and mix-variance, average the homogeneity of the

concentration field over various scales [45]. They do not depend on a choice of coarse-graining scale and they succeed in capturing the stirring efficiency when diffusion is negligible.

Two important aims of this dissertation are to observe the relationship between chaos and mixing and to investigate the relationship between the analysis of TNCT and the actual flow stretching. For these comparisons and for evaluation of the performance of various mixing systems of this research, the above-mentioned chaos and mixing measures are used. Chapter 2 is dedicated to the details of calculation and important parameters of the concentration-based measures of homogeneity.

1.6 Ghost rods

Depending on the specific dynamics of any stirring system, different periodic orbits may exist in the phase space, namely in the type of centers, hyperbolic and parabolic periodic points of the Poincaré map. These points, while being passive and determined by the flow itself, can play the role of stirrers and are called "ghost rods" [31, 62, 72, 73]. They braid the flow and introduce topological complexity in the system (Fig. 3.11). Parabolic and hyperbolic points and centers (elliptic islands) have different effects on the rate of mixing [30, 72]. These effects on the mixing efficiency of various stirring systems in chapters 3, 4 and 5 are studied by numerical simulation of stretching and homogenization and by analysis of the transport via invariant-manifold structures. In chapter 3, it is shown that by geometric modification of rods and their motion and without changing the topology of motion of solid rods, the periodic-point structure of the flow can be changed and the mixing efficiency of the stirring system can be enhanced. In a recent development [65], it has been shown that another type of ghost rod like structures may also be recognized in chaotic flows using a set-oriented approach, namely Almost Invariant Sets (AIS). Chapters 4 and 5 show that the AIS play different important roles in understanding and analysis of chaotic mixing.

1.7 Transport and mixing via lobe dynamics

Mixing in a dynamical system is closely connected to the concept of transport [51, 80]. In the view of lobe dynamics the phase space consists of different regions separated by stable and unstable manifolds of hyperbolic points [59, 77, 7, 78] and in order for mixing to happen the passive particles should be *transported* between the regions. Studying the structure of these regions, their boundaries and the mechanism of transport through these boundaries helps to understand the details of the different mechanisms behind chaotic mixing.

As it was mentioned before, periodic points in the flow's Poincaré map can play the role of ghost rods in stirring the flow. In chapter 4 it is shown that some ghost rods can also act like obstacles that impede the mixing. From the point of view of lobe dynamics, periodic orbits play another important role in transport: segments of their stable and unstable manifolds define boundaries of different regions in the phase space. The particles can cross these boundaries and transfer from one region to a neighboring region only under special circumstances and via special gateways (lobes) [77]. In chapter 5, this fact is used to explain different rates of homogenization for different systems.

Lobe dynamics has been used to explain transport and mixing in different dynamical systems. Some examples are: the flow in an eccentric journal bearing [38], flows with aperiodic time-dependency like Rossby wave flow [44], oscillating vortex pair [58], and oceanographic, coastal and atmospheric flows (see for example [55, 16, 36, 79]). Transport via lobes is not confined to mixing problems. For example in dynamical astronomy, transport between different regions of phase space can be studied quite similarly [19].

Fig. 1.2 is the generic figure for transport via lobes. Following Wiggins [77], let p_i and p_j denote two hyperbolic periodic points of the flow and $W^s(p_i)$ and $W^u(p_j)$ denote the stable manifold of p_i and the unstable manifold of p_j respectively. As it is

proved in [77], under one iteration of the flow the only points that can transfer from R_1 to R_2 are those inside the *lobe* $L_{1,2}(1)$ shown in Fig. 1.2. Similarly, the only points that can transfer from region R_2 to R_1 under one iteration of the flow are those inside the *lobe* $L_{2,1}(1)$. The Stokes flow of Eq. 1.1 is area-preserving, thus the lobe area is always mapped to another lobe of the same area. Therefore the transport of material per iteration of the flow between the regions R_1 and R_2 can be simply equated to the lobe area. In order for homogenization to happen, the particles need to get caught in one of the lobes so that they can be transported to other parts of the domain.

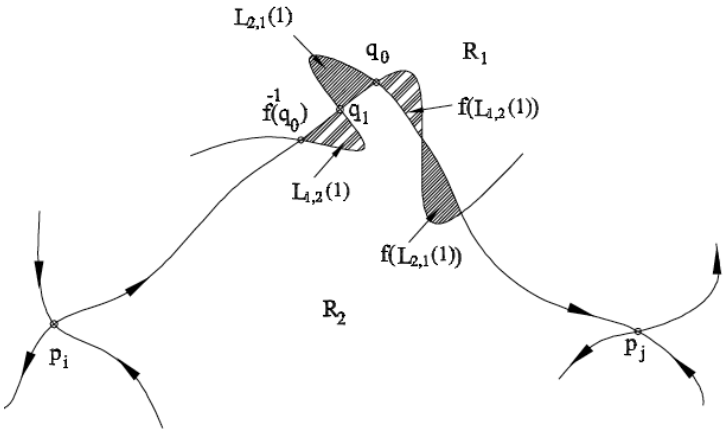

Figure 1.2: Schematic figure of invariant manifolds of two periodic points p_i and p_j, the pip and the lobes.

This mechanism of transport is illustrated for the lid-driven-cavity flow of chapter 5. It is shown that the special configuration of periodic points and structure of their manifolds cause slower homogenization in some systems. Using lobe dynamics, the fluctuations in the rate of mixing from the view point of geometric mechanics are explained.

1.8 Layout of the dissertation

Chapter 2 explains some of the concentration-based mixing measures and shows the effect of different parameters on these measures in the evaluation of performance of

mixing systems. These measures are used in the rest of the dissertation to study the correspondence between chaos and mixing in various chaotic mixing systems.

Calculation of the stretching rate using a solution of the flow field, as presented in chapter 3 for various systems, requires thousands of processor-hours even for the cases that the flow field is known. However, the topological analyses of the TNCT provide a great inexpensive tool for prediction of chaos and stretching in mixing systems. Without knowing the details of the fluid dynamics of the system, this theorem enables estimation of the stretching rate only based on the topology of boundary motions. Chapter 3, using rod-stirring devices as example systems, investigates the extent to which the topological predictions of the TNCT can be used in the selection and design of the optimum mixing protocols. In particular that chapter addresses the following question: how does it matter in practical or 'real' mixing systems to use stirring protocols that are identified as pseudo-Anosov by the TNCT?

As explained in this introduction, the stretching rate or equivalently the topological entropy is widely used to measure the chaos in mixing systems. Chapter 4 investigates the relationship between stretching in terms of the topological entropy and the 'real' mixing in the chaotic systems, using a cavity flow as an example system. It uses a set oriented approach to explain the stretching and mixing caused by almost invariant sets (AIS) playing the role of ghost rods. In that chapter, it is discovered that the 'leaky' AIS are the optimum type of stirrers. Unlike the solid rods or periodic points, these objects, while stirring the flow, get resolved in the flow themselves and do not produce unmixed or slowly-mixing regions around themselves, causing the highest rates of mixing in these systems.

In chapter 5, it is shown that the behavior of the recently introduced ghost rods, the AIS, can be explained by lobe dynamics theory. In particular, the strange two-rate decay observed in chapter 4 is estimated using the geometric view of lobe dynamics.

Chapter 6 presents two schemes for the selection of the optimum stirring protocol based on the distribution of the scalar, for systems that are capable of performing

multiple protocols. It is shown that using an optimized combination of different stirring protocols, rather than solely using one of them, can effectively enhance the mixing.

2

Concentration-based measures of homogenization

In the design of a mixing device it is usually favorable to homogenize an initially segregated state at the highest possible rate. Through (expensive) line tracking simulations, it is possible to observe the patterns of stretching for a few periods of a flow and calculate the topological entropy. However, normally in a mixing application the passive material is initially a highly concentrated blob of particles rather than long, infinitesimally thin line and this blob gets stirred for a large number of periods. In order to investigate mixing and to associate stretching with mixing, the homogenization of a box of many passive particles, resembling a blob of passive scalar advected by the flow, can be simulated. This enables calculation of the concentration distribution which is originally segregated but becomes uniform over time as chaotic advection spreads the particles in the chaotic sea. The level of homogeneity as measured by one of the various concentration-based measures as described below, provides information regarding the correlation between the homogenization and stretching results. This simulation can be seen as a numerical investigation of the flow's mixing behavior without diffusion. Some artificial diffusion is involved in these calculations through coarse-graining of the domain. However, accurate incorporation of diffusion is not the purpose of this dissertation and needs a separate study.

Concentration calculations have been widely used in the evaluation of mixing (see

for example [18, 17, 53, 66, 30]). This chapter aims to provide instructions for the use of these mixing measures for comparison of different systems or a single system in different situations. This comparison is application-dependent; for example in some applications the short-term mixing matters, in some the long-term. In some applications the power usage is important, while in others the speed is of primary importance.

2.1 Concentration variance and multiscale measures

The most common mixing measure in this context is the intensity of segregation which is based on the variance of concentration of a tracer material [18]. In order to calculate the concentration variance numerically, an initially dense blob consisting of many passive particles is advected for a number of periods of the flow. After partitioning the domain of interest into an appropriate number of equal-sized bins, the discretized concentration field can be defined as

$$c(x_i, y_i) = \frac{n_i}{A_b}, \tag{2.1}$$

where n_i denotes the number of particles inside the i^{th} bin, which is centered at (x_i, y_i). The side length of a bin is denoted by d and its area is equal to $A_b = d^2$. Any other constant can be used instead of A_b for the sake of simplification. The variance of this function (CV) is calculated as

$$CV = \frac{1}{A}\int_D (c(x,y) - \bar{c})^2 dA = \frac{1}{N_b}\sum_{i=1}^{N_b}(c_i - \bar{c})^2, \tag{2.2}$$

in which D is the test window and $\bar{c}$ is the mean value of c_i and N_b is the number of bins. As the flow advects the particles, the particles get spread over the chaotic sea and the concentration becomes more uniform in the chaotic sea. If the Poincaré section possesses elliptic islands, in the absence of diffusion, no particles will enter

the islands. When the CV is calculated over the whole domain, it represents both the effect of the size of the chaotic area (or equivalently the negative effect of elliptic islands in which mixing is slow) and the effect of homogenization inside the chaotic area. It is also possible to calculate the CV for the chaotic region without including the bins inside the elliptic islands so that we can measure the mixing solely due to homogenization inside the chaotic sea.

Practical implementation of this measure depends on the coarse-graining scale of the domain and it cannot capture the effect of stirring in smaller scales. Also, in the limit of calculation with infinitesimally small bins, the concentration field is a continuous function, and its variance $\int (c(\mathbf{x}) - \bar{c})^2 d\mathbf{x}$ does not decay under the area-preserving flow of Eq. 1.2 (see [45] for details). In the CV calculation, the discretization of the domain via the bins adds some artificial diffusion to the system in order to make the tracer homogenization observable via calculation of concentration variance. This makes the measure, somehow arbitrary and unable of capturing the effects of stirring in small scales.

The recently developed multi-scale mixing measures, mix-norm and mix-variance [45] and the multi-scale mixing efficiencies [60], average the homogeneity of the concentration field over various scales.

The mix-variance (MV), one of the multiscale measures, is defined as follows. Let the average of the function $f(\mathbf{x}) = c(\mathbf{x}) - \bar{c}$ over any area D of scale s centered at location $\mathbf{p}$ in the domain be given by

$$d(\mathbf{p}, s) = \frac{\int_D c(\mathbf{x}) d\mathbf{x}}{Area(\mathbf{p}, s)}. \tag{2.3}$$

The average of this function over the domain for a fixed s is

$$\phi(s) = (\int d^2(\mathbf{p}, s) d\mathbf{p})^{\frac{1}{2}}, \tag{2.4}$$

and the average of $\phi(s)$ over all possible scales s is defined as the $Mix - Variance$

$$\Phi = (\int_0^1 \phi^2(s)ds)^{\frac{1}{2}}. \tag{2.5}$$

It is proven in [45] that the Mix-Variance (MV) can be calculated as

$$MV = \sum_{j,k}^{\infty} \Lambda_{j,k} a_{j,k}^2, \tag{2.6}$$

which is the weighted sum of squared Fourier amplitudes of the deviation of the concentration field from its mean. $a_{j,k}$ are defined according to

$$c(x,y) - \bar{c} = \sum_{j,k}^{\infty} a_{j,k} e^{2\pi i(jx+ky)}, \tag{2.7}$$

and

$$\Lambda_{j,k} = \int_0^1 \frac{2J_1(s\pi\sqrt{i^2+j^2})}{s\pi\sqrt{i^2+j^2}} ds \tag{2.8}$$

in which J is Bessel function of the first kind.

The multiscale measures have been applied for theoretical study of chaotic mixing in general Stokes flow ([46]) and in steady sources ([20]). However there has not been any reported attempt to use them in the numerical evaluation of mixing efficiencies for practical stirring systems. As a future direction for study, their use in measuring the n-rod stirring performance can be investigated. The performance of this measure for different prescribed distribution of particles and the correlation between the results of CV and MV can be studied. The next step would be developing the numerical method of calculation of the multiscale measures for a circular domain and a domain with holes.

2.2 Direct particle tracking method for concentration calculation

This dissertation uses the CV as a measure of homogenization for the example flows of the next chapters. As the first step for the calculation of any concentration-based measure, the concentration field can be calculated in different ways. The more common method is *direct* particle tracking as follows [53]. The domain of interest is partitioned into a number of bins, N_b. A large number of passive particles (N_{pt}) initially located in a small area representing a dense two-dimensional box of a tracer material are tracked under the advection of the flow. Using a larger number of particles gives a higher resolution and consequently a better accuracy for more periods of the flow. At any time step (here any period $t = k\tau$, $k = 0, 1, 2, ...$), the number of particles inside each bin, scaled by some factor for simplification, is defined to be the local value of the discretized concentration field (Eq.2.1).

Initially the particles are concentrated in a few bins so the concentration is high in the location of those bins and is zero elsewhere. While the flow advects the particles, they get spread over the chaotic sea and the concentration becomes more uniform. A completely homogeneous domain will have a zero CV and with appropriate scaling, at the initial segregated system the CV is equal to 1 so that the numbers are scaled relative to the initial state of the system. Fig. 2.1 shows the homogenization of the passive scalar and the CV decay diagram for the example system of chapter 4 with $\tau = 1$. In this calculation, 360000 passive particles are used and the side length of a bin is equal to $d = \frac{\pi}{60} \approx 0.05$. Also Fig. 2.2 shows the numerical simulation and the plot showing the results of this calculation for one million passive particles in the blob and with bins of side lengths of $d = 0.01$ for the 4-rod stirring system A_3 of section 3.2.2.

Since all the particles inside a bin are considered to be uniformly distributed in that bin, some artificial diffusion is introduced in the calculation of CV. Note that

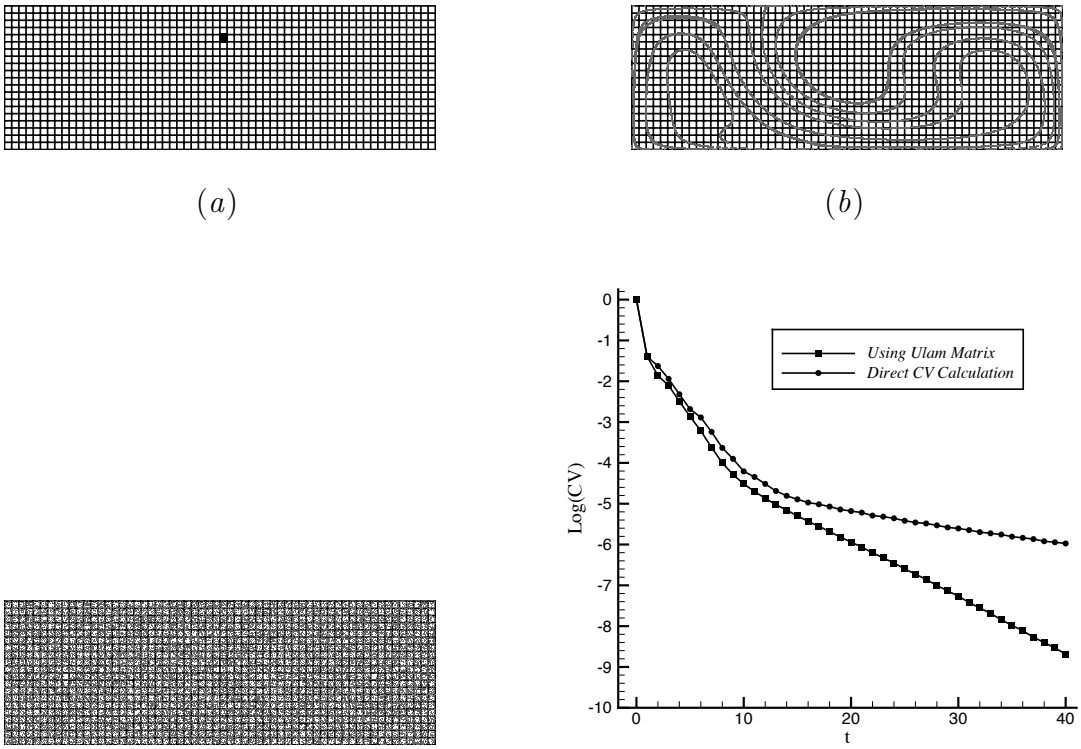

Figure 2.1: The cavity flow of chapter 4 with $\tau = 1$. Homogenization of an initially dense 2-D box of passive scalar for (a) 0, (b) 5, and (c) 40 periods of the flow. (d) The corresponding CV decay diagrams calculated by direct calculation and via Ulam matrix.

in the direct method of calculation, the discretization (coarse-graining) does not have any effect on the particle tracking part of the calculation and only appears in the calculation of the CV. In other words, directly tracking the location of particles is totally independent of the coarse-graining caused by binning the domain. The direct method is used for the rod-stirring systems of chapter 3.

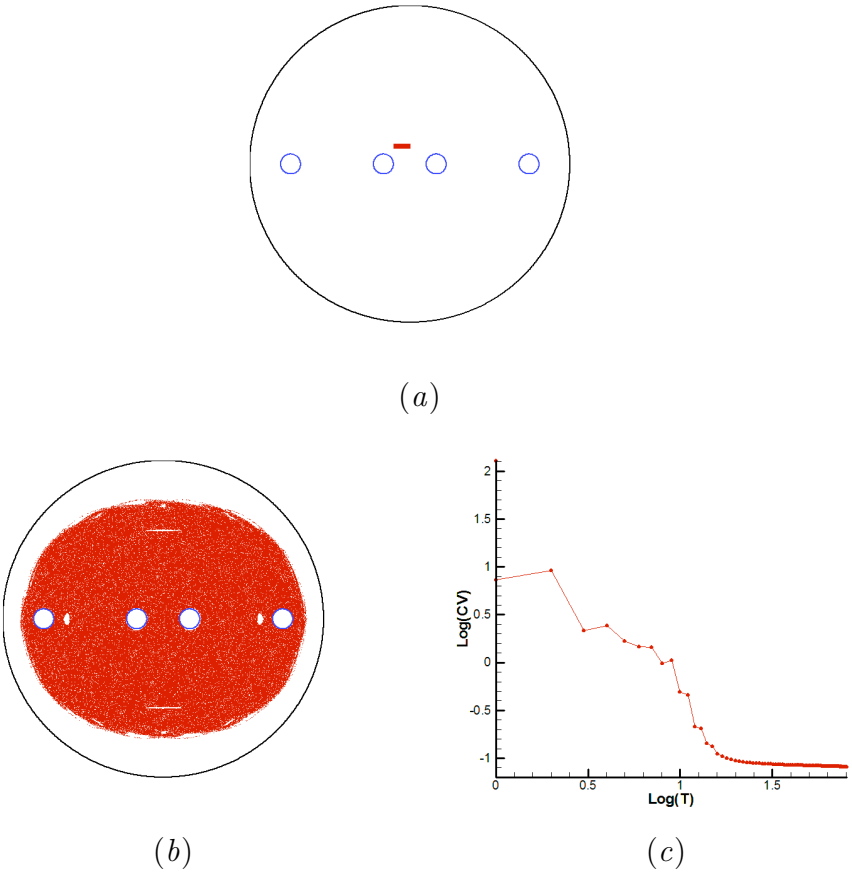

(a) (b) (c)

Figure 2.2: (a) The initial blob of scalar. (b) The blob, stirred for 40 periods of flow. (c) Log-log plot of CV decay for the 4-rod system A_3 of chapter 3.

2.3 Concentration calculation using the Ulam matrix

For the objectives of chapters 4 and 6, there is a preferred method of calculating the coarse-grained concentration field which uses the Ulam matrix P. This approach is

quite similar to the *mapping method* used in [61] for mixing analysis in systems like the cavity flow. This is a systematic method in which diffusion is taken into account in every period of the particle tracking and not only in the final CV calculation. The concentration at the location of each bin (cell), $c_i, i = 1, 2, ..., N_b$ is considered to be an entry of the concentration vector C. Each p_{ji} entry of the Ulam matrix P is equal to the fraction of the tracer material transferred from bin i to bin j after one period of the flow (Fig 2.3). In other words, $p_{ji} = \frac{N_{ij}}{N_{pt}}$ where N_{pt} is the number of particles initially located in each bin i and N_{ij} is the number of particles migrated from bin i to bin j in one period of the flow. It is then straightforward to see that the concentration vector evolves as

$$C_{n+1} = P.C_n$$

or

$$C_n = P^n.C_0 \tag{2.9}$$

In order to compute p_{ij} with desired accuracy, we need to track the location of a large

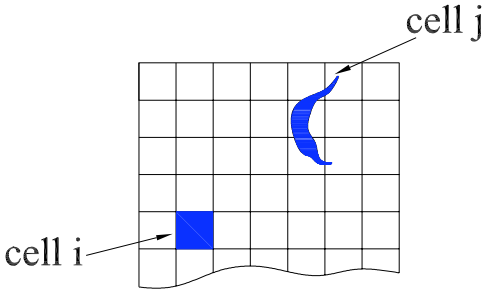

Figure 2.3: Computation of entries of the Ulam matrix. The square of tracer material is mapped to the curved drop after one period of the flow. An entry p_{ji} of the Ulam matrix is equal to the percentage of material in bin i that is mapped to bin j after a period.

number of particles (N_{pt}) initially located in bin i and count the percentage of this number that travels to each bin j. This has to be done for all the bins, $i = 1, 2, , N_b$; so we need to track $N_b.N_{pt}$ particle locations for one period of the flow. Once the

Ulam matrix is computed with the appropriate bin-size and accuracy, it is simple and fast to compute the concentration vector and CV using Eqs. 2.9 and 2.1, for any number of periods of the flow and for any desired initial distribution of passive scalar. Fig.2.1 includes the diagram of CV decay based on the concentration calculation via Ulam Matrix method.

2.4 Effect of parameters on CV calculation and diffusion considerations

In order to use the CV decay as a base of comparison of different protocols, the effect of different parameters on this calculation should be clarified. As will be discussed in section 3.1.2, locating the initial blob of particles in some regions leads to a higher initial rate of decay, while there are other regions of slower initial homogenization (Figs.3.8 and 3.9). This difference can be explained by the action of invariant manifolds and their lobes on transport (see section 5.1). As Fig.2.4 shows, using the Ulam method of concentration calculation, the number of particles resembling the scalar, N_{pt}, and the coarse-graining scale, d, also affect the CV calculation. At the initial segregated states a small N_{pt} works but in order to observe the concentration decay in the well-homogenized states, a larger N_{pt} is needed [53]. $N_{pt} = 360000$ particles per bin gives enough resolution to observe the decay till 20 time units for the fastest cases (e.g. the cavity flow with $\tau = 0.85$ in chapter 4). After that limit the decay stops and a constant 'tail' is seen. As proved in [53] and Figs.2.5 and 2.4 illustrate, this tail is an artifact of numerical computation and at the limit of $N_{pt} \to \infty$ the homogenization continues with its exponential pace. Therefore in the analyzes of the subsequent chapters the tail is ignored.

In direct calculation of concentration, values of CV displayed in Fig.2.5, converge to the same numbers after a long term homogenization if the number of particles and the bin size are chosen so that $N_{pt}d^2$ remains constant i.e. if N_{pt} varies conversely

proportional to the bin area. For a big enough N_{pt} when varying the N_{pt}, CV decay is the same for initial periods but for higher periods the curves with smaller number of particles diverge sooner. Varying d while N_{pt} is kept constant, causes a shift in the CV diagram which is approximately constant during the initial stages but diverges when the second part begins. This is the effect of artificial diffusion as explained in the following.

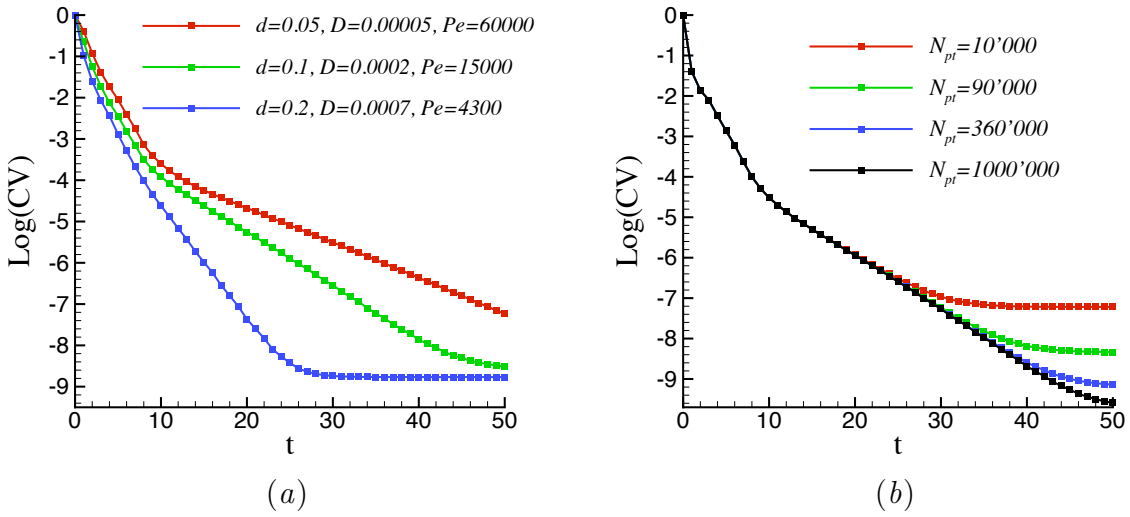

Figure 2.4: Effect of parameters on CV calculation using the Ulam-matrix method: (a) effect of bin-size (and the equivalent diffusivity and Péclet number) on CV decay. More diffusivity causes faster homogenization. (b) effect of number of particles per bin (N_{pt}) on CV decay. As $N_{pt} \to \infty$, the artificial 'tail' disappears.

The coarse-graining scale (bin-size) is a numerical representative of diffusivity, so that choosing bigger bins is physically equivalent to assuming a more diffusive system. On the other hand, since a single concentration value is assigned to each bin, choosing smaller bins clearly leads to more resolution in the evaluation of the local concentration field. Fig. 2.4 (left) shows the effect of variations of bin-size on the decay of CV. As it is expected, larger bin (higher diffusivity) causes higher rate of homogenization. In order to estimate the implicit diffusivity of CV calculations, an analogy with the definition of the diffusion is employed in the following. For the

no-flow case, the concentration evolves according to the diffusion equation

$$\frac{\partial c}{\partial t} = D\nabla^2 c, \tag{2.10}$$

with $c = c(x, y, t)$ denoting the concentration field and D denoting the diffusivity. Let a highly concentrated scalar located at a point be diffused by this equation with a specific diffusivity D for a certain amount of time $\triangle t$. The 'effective' area that the scalar occupies after $\triangle t$ is a reasonable approximation of the bin area of the coarse-graining corresponding to the same diffusivity and $\triangle t$. Using Fourier transform, the diffusion equation is integrated with the initial scalar distribution $c(x, y, 0) = \delta(x)\delta(y)$, ($\delta$ being the Dirac delta function) and assuming $\lim_{x\to\pm\infty, y\to\pm\infty} c(x, y, t) = 0$. The result is

$$c(x, y, t) = \frac{1}{4\pi^2}\int_{-\infty}^{\infty}\int_{-\infty}^{\infty} e^{-Dt(\omega_1^2+\omega_2^2)} e^{i(\omega_1 x+\omega_2 y)} d\omega_1 d\omega_2. \tag{2.11}$$

Since the coarse-graining in Eq. 2.9 is effective at every period ($t = k\tau, k = 1, 2, ...$), $\triangle t$ is chosen to be τ. So $c(x, y, \tau)$ should be calculated. The concentration decays as (x, y) moves away from the origin independent of the direction, i.e. c is only a function of $r = \sqrt{x^2 + y^2}$ and t. Figure 2.6 shows $c(r, \tau)$ for $\tau = 1$ and $D = 5 \times 10^{-5}$. The cut-off distance r_c is the effective radius of the circular area occupied by the diffused blob of particles so the corresponding side of a square bin, d, is equal to $\sqrt{\pi r_c^2}$. r_c is determined by the cut-off concentration which here is chosen to be %1 of concentration at $r = 0$; i.e. $\frac{c(r_c,\tau)}{c(0,\tau)} = 0.01$. This estimation for a bin size of $d = \pi/60$ (as used for the cavity flow in chapter 4) and $\tau = 1$ gives a diffusivity of about 5×10^{-5}. The *Péclet number* (Pe) for the range of coarse-graining scales used in this dissertation is thus of order of 10^4. Pe is the ratio of the rate of advection to the rate of diffusion and is defined as the product of the *Reynolds number* and the *Schmidt number*: $Pe = Re.Sc = \frac{LV}{\nu}\frac{\nu}{D} = \frac{LV}{D}$.

The direct concentration calculation tracks the particles without diffusion but

uses the coarse-graining in the calculation of the variance at any time step (Eq. 2.1). Therefore, depending on the corresponding time step the $\triangle t$ in the above analogy changes and the diffusivity changes accordingly. Since $\triangle t$ in this method is mostly larger than that for the Ulam-matrix method, the corresponding diffusivity is in overall, smaller than that method.

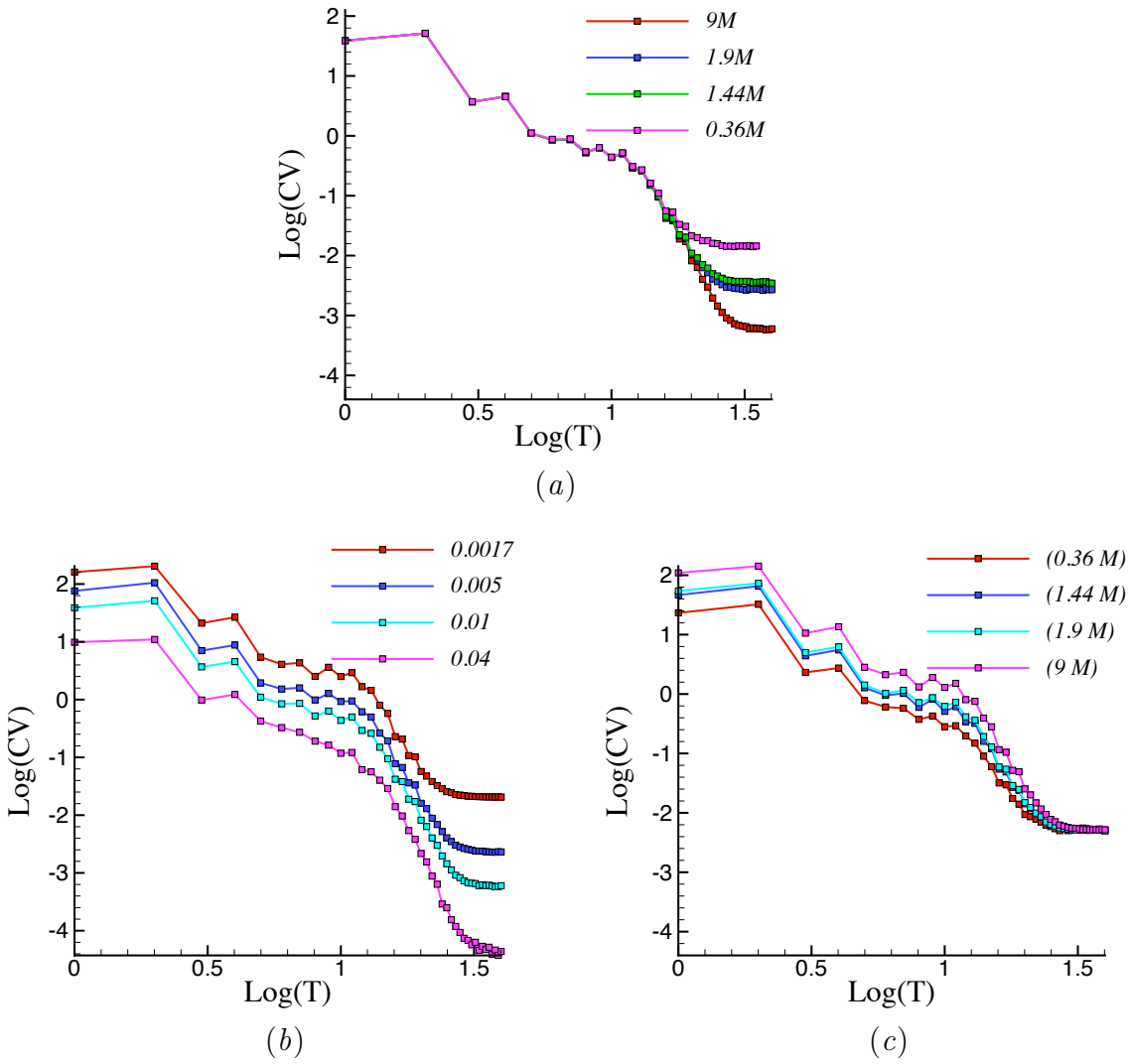

Figure 2.5: Log-log plots of concentration variance decay using direct method for the 4-rod system of Fig. 2.2 using different parameters in the calculation. d and N_{pt} represent the bin-size and the number of particles consisting the initial blob respectively. (a) $d = 0.01$, varying N_{pt}. (b) varying d, $N_{pt} = 9million$. (c) $N_{pt}d^2 = constant = 100$.

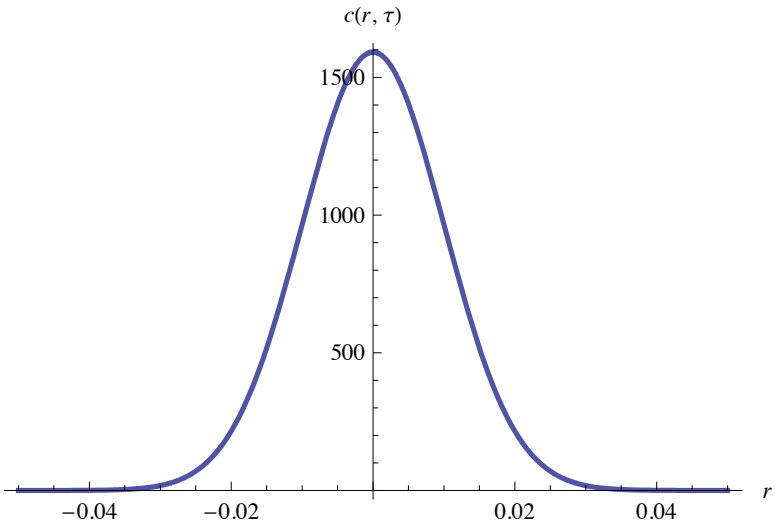

Figure 2.6: $c(r,\tau)$ for $\tau = 1$ and $D = 5\times10^{-5}$. The effective radius of the circular area occupied by the initially point-wise passive scalar after 1 period of the flow is $r_c \approx 0.03$. The equivalent bin-side is equal to $\sqrt{\pi r_c^2} \approx \pi/60$ which is used for all the CV calculations of chapter 4.

3

Topological chaos and mixing in rod-stirring systems

This chapter is dedicated to the study of mixing in periodic Stokes flows where physical rods stir the flow using an outside power source. All the protocols considered here are variations of the generic system shown in Fig.1.1. The outer boundary is kept stationary and the internal rods are the only moving boundaries. In some protocols considered here the rods have an angular velocity around their geometric center while they are translating on a circular path around prescribed fixed centers. In others they only translate. In all systems the motion of rods is enforced by some prescribed periodic velocity function so that trajectories of the rods and thus the flow are periodic. A period of the system is defined as the time needed for all the rods to go back to their original position. The topological chaos generated by these protocols in a Newtonian fluid is studied and the practical use of the Thurston-Nielsen classification theorem (section 1.3) in these systems is examined. It will be seen that in some cases the exponential stretching is not only due to physical rods but also due to the periodic points of the flow playing the role of passive or "ghost" stirrers.

The rod-stirring protocols of this chapter are extracted from industrial taffy pulling mechanisms. These protocols produce relatively high rates of stretching. Protocols A and B of Fig. 3.18 have the same topology of motion as common three- and four-prong taffy pulling devices. In protocol A two pairs of rods rotate with the same

Figure 3.1: A three-rod taffy pulling mechanism. [picture by H. Greenside www.phy.duke.edu]

angular velocity around two different centers located on the x axis. In B two rods rotate with opposite angular velocity around two centers located symmetrically on the right and left of the central fixed rod. Taffy pullers are designed to repeatedly stretch and fold a viscoplastic substance, usually using three or four rods or prongs. As it will be illustrated with numerical simulations and comparison to the topological theory, this process causes rapid separation of nearby points that leads to exponential stretching of lines. A three-rod taffy pulling mechanism is shown in Fig.3.1, in which two rods rotate with the same angular velocity around two centers located on the left and right side of a fixed rod. The 3-rod stirring protocols studied here are derived from this industrial mechanism.

3.1 Discussion on the role of topological chaos and ghost rods in 3-rod systems

This section considers stirring and mixing of a two-dimensional Stokes flow in a circular domain due to the motion of three rods. Two similar protocols are discussed that are expected to give significantly different results based on the topology of their braid representations and predictions of the Thurston-Nielsen classification theorem

(TNCT) [9] (see section 1.3). In order to associate the stretching results to fluid mixing, the homogenization of a passive scalar advected by the flow is studied and the correspondence between the decay of concentration variance of the scalar and the stretching results is discussed.

The basic stirring protocols studied in this section are described in Fig. 3.2. In section 3.1.4 other protocols are derived from these main systems by varying the geometric parameters of the rod motions. In order to characterize the periodic 2-dimensional 3-stirrer motions topologically, it is represented by a physical braid on 3 strands as explained in section 1.3. The physical braid representing a stirring protocol consists of the stirrer trajectories in the (2+1)-dimensional space-time of the form $(x(t), y(t), t)$ for one period of the system (T), in which $x(t)$ and $y(t)$ are the coordinates of a rod at time t. T is the time required for all the stirrers to go back to their original position (Fig. 3.3). From a topological point of view, only interchanges of strands in the braid matter. In order to have a mathematical description of the physical braid, a letter σ_i is assigned to each clockwise interchange of strands i and $i+1$ and a letter σ_i^{-1} to their counter-clockwise interchange. Composition of these letters as a braid word for multiple interchanges of strands represents the physical braid of the stirring protocol. In a 2-dimensional image of a physical braid such as the one shown in Fig. 3.3, interchanges of the strands and their sign could be determined by over- and under-crossings of the curves showing the strands.

Braids can be mathematically represented by matrices. Following the method of [9], the matrix representation of σ_2 (Fig. 3.4) is

$$M_2 = \begin{bmatrix} 1 & 0 \\ 1 & 1 \end{bmatrix}, \tag{3.1}$$

For σ_2^{-1}, σ_1 and σ_1^{-1} the matrix representations are

$$M_2^{-1} = \begin{bmatrix} 1 & 0 \\ -1 & 1 \end{bmatrix}, M_1 = \begin{bmatrix} 1 & -1 \\ 0 & 1 \end{bmatrix} and\, M_1^{-1} = \begin{bmatrix} 1 & 1 \\ 0 & 1 \end{bmatrix}, \tag{3.2}$$

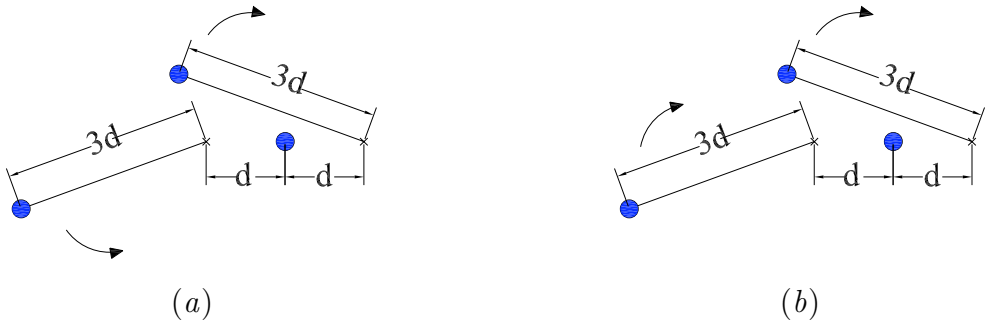

(a) (b)

Figure 3.2: (a): In protocol $PA1$ two rods rotate with the same angular velocity but in opposite directions around two centers located symmetrically on the right and left of the central stationary rod. (b): In protocol $FO1$ the two moving rods rotate in the same direction.

respectively.

As Fig. 3.3 shows, the braid of protocol $PA1$ is composed of the following interchanges of the strands. First the two right strands interchange in a clockwise sense which is denoted by a σ_2 letter; then the two left strands interchange two times in a counter-clockwise sense which is denoted by $\sigma_1^{-1}\sigma_1^{-1}$; then the two right strands again interchange in a clockwise sense which is denoted by a σ_2. Therefore the braid word representing protocol $PA1$ is shown by $\sigma_2\sigma_1^{-1}\sigma_1^{-1}\sigma_2$ and is represented by the product of the corresponding matrices:

$$M_{PA1} = M_2 M_1^{-1} M_1^{-1} M_2 = \begin{bmatrix} 3 & 2 \\ 4 & 3 \end{bmatrix} \tag{3.3}$$

According to the TNCT, M_{PA1} represents a pseudo-Anosov protocol for which chaotic particle trajectories are guaranteed and there exists at least one material line with a stretching rate of equal to or bigger than the biggest eigenvalue of M_{PA1}, $\lambda_{TN} = 3 + \sqrt{8} \simeq 5.83$.

In the same way it can be seen that the protocol $FO1$ is the result of respective action of σ_2, σ_1, σ_1 and σ_2 (Fig.3.3) and is represented by the product of the corresponding matrices as

$$M_{FO1} = M_2 M_1 M_1 M_2 = \begin{bmatrix} -1 & -2 \\ 0 & -1 \end{bmatrix}. \tag{3.4}$$

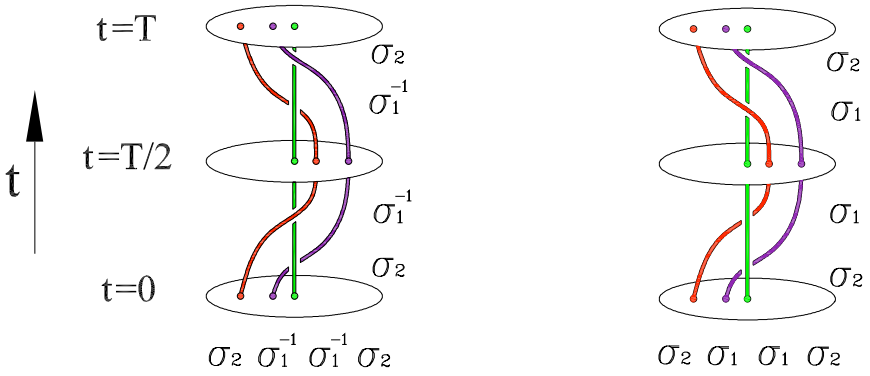

Figure 3.3: Physical braids and braid words for (A) the stirring protocols $PA1$ and (B) $FO1$. The braid consists of the trajectory of the stirrers over one period of motion in (2+1)-dimensional space-time. The disks show the fluid domain at different instants of time. The braid letter for each interchange of stirrers is written on its right and the braid word for each protocol is written at the bottom.

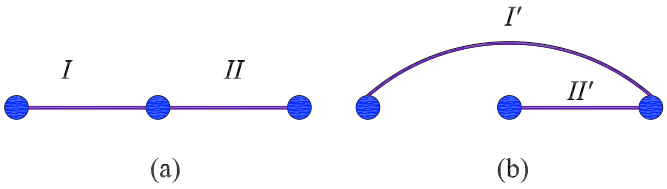

Figure 3.4: Transformation of material lines under σ_2.

Since the eigenvalues of the matrix representation of protocol B do not include a real number greater than one, it is of finite order type, and exponential stretching is not guaranteed for it.

Comparing the results of a numerical simulation to the lower bounds predicted by TNCT, this chapter discusses how the predictions of this theorem can be helpful in selecting high stretch-rate stirring protocols.

In the limit of a vanishing Reynolds number, and considering an incompressible Newtonian fluid, a motion of the stirrers generates a Stokes flow with the streamfunction $\psi(z, \bar{z})$ satisfying the biharmonic equation: $\nabla^4\psi = 0$ [39]. With $z = x+iy$ denoting the coordinates in the complex form, the velocity field is given by $u+iv = -2i\frac{\partial\psi}{\partial\bar{z}}$. The solution has to satisfy the no-slip boundary conditions at the outer boundary and on the boundaries of the rotating rods. Placing rotlet and Stokeslet singularities

at the center of each rod and using the circle theorem to satisfy the boundary condition at the outer boundary, Finn *et al.*(2003) have presented a series solution for the stirring device of Fig. 1.1 of the form [27]

$$\psi(z,\bar{z}) = \sum_{i=1}^{mn} A_i(t_k) f_i(z) + \overline{A_i}(t_k)\overline{f_i(z)} \tag{3.5}$$

for any instant of time, $t_k = \frac{kT}{N_s}$ where N_s is the number of time steps in one period. In the above equation m is the number of rods and n is number of terms in the series that are required to get accurate results. Since the rod motions are periodic in time, the velocity field is periodic and it is enough to determine it for one period. The coefficients $A_i(t_k)$ are calculated by applying the boundary conditions on the boundary of rods $j = 1, 2, ..., m$,

$$u(x,y,t) + iv(x,y,t) = U_j + iV_j + i\Omega_j(z - p_j), \tag{3.6}$$

in which $U_j + V_j$ and Ω_j are the given translational and angular velocity of the j-th rod. The boundary condition at the outer boundary is already satisfied by the circle theorem [27].

In order to track the passive fluid particle trajectories, the ODEs

$$\begin{aligned} \frac{dx}{dt} &= \frac{\partial\psi}{\partial y}(x,y,t), \\ \frac{dy}{dt} &= -\frac{\partial\psi}{\partial x}(x,y,t), \end{aligned} \tag{3.7}$$

should be integrated in discrete form. A fourth-order Runge-Kutta algorithm with parameters $Ns = 150$ and $n = 12$ gives converged results in most cases. Since the velocities obtained from the series 3.5 are nonlinear, it is evident from the nonlinear non-autonomous advection equations (3.7) that the flow is capable of generating chaotic trajectories [3]. This solution enables tracking of passive particles as well as non-trivial material lines consisting of passive particles. A material line is initially represented by a number of particles. Because of the exponential divergence of tra-

jectories in chaotic systems, the distance between adjacent particles grows very fast. In order to see the line's fine structures and calculate the length of the stretched line accurately we use a point insertion algorithm similar to the one in [27] to maintain the distance between adjacent points on the line below a desired minimum.

3.1.1 The pseudo-Anosov 3-rod protocol, $PA1$

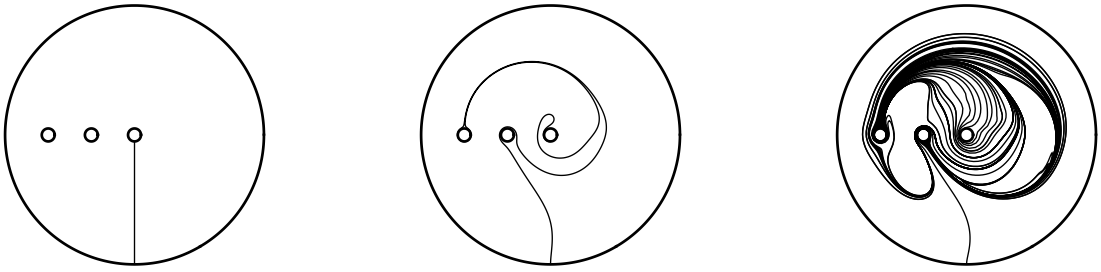

Figure 3.5: Numerical simulation of line stretching in the 3-rod stirring system $PA1$. Images of a non-trivial material line stretched for (a) 0, (b) 1 and (c) 3 periods of motion. The length of the stretched line after 1 period is $L_1 \simeq 7.5L_0$ and after 3 periods it is $L_3 \simeq 289.1L_0$.

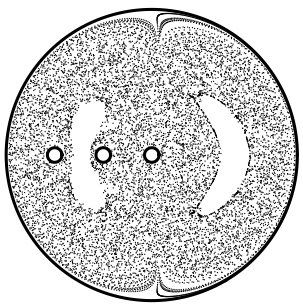

Figure 3.6: Poincaré section for the 3-rod system $PA1$.

We simulate the advection of non-trivial material lines consisting of passive fluid particles under the flow of system $PA1$. The geometric parameters are chosen according to Fig. 3.2 with $d = \frac{1}{6}$ and the radius of the cylindrical domain scaled to 1.

Images of different stages of stirring are shown in Fig. 3.5. A Poincaré section for system $PA1$, obtained by tracking a single particle trajectory for 40'000 periods of flow, is shown in Fig. 3.6. The chaotic sea is relatively large. This is the area that will be perfectly mixed after (theoretically) infinite periods of the flow. Other than the chaotic sea that is extended to the outer boundary of the domain, two crescent shape regular regions can be seen in the Poincaré section as well.

The stretching of a material line shown in Fig. 3.5 demonstrates how the structure of the Poincaré section is generated. As time goes on the stretched material line resembling a streak of dye in system $PA1$ fills the whole domain except two crescent shape regions on the right and left side of the center. The upper half of the domain ($y > 0$) is filled sooner by the filament and the lower half needs more time to be filled. The resulted heart shape is directly related to the path of the two moving rods and the fact that they rotate in opposite directions relative to each other. Long-term effects of these behaviors are observable in the Poincaré section of the flow. The Poincaré section confirms that after a long time, the mixed blob of dye will fill the fluid domain up to the outer boundary, except for the islands. In this picture the particles close to the boundary exhibit slow, nearly regular motion as it can be anticipated from the zero-velocity boundary condition on the wall [30]. These properties are in some aspects connected to the topology of motion of rods while some of them are consequences of specific dimensions and geometries involved and can vary for a single topology of motion of solid rods. In section 3.1.4, using different geometries of rod motions, this fact is discussed with more illustrations.

When the stretching of a material line is exponential, i.e. Eq. 1.6 holds, the topological entropy as a measure of chaos in the system is defined to be the exponent h. The above numerical simulation gives $h_{flow} \simeq 1.764$, while the topological entropy predicted by TNCT, the logarithm of the largest eigenvalue of the matrix representation of the braid (3.9), is $ln(3+\sqrt{8}) \simeq 1.763$. The agreement between the theoretical prediction and the actual flow entropy confirms that TNCT offers a valuable estimate

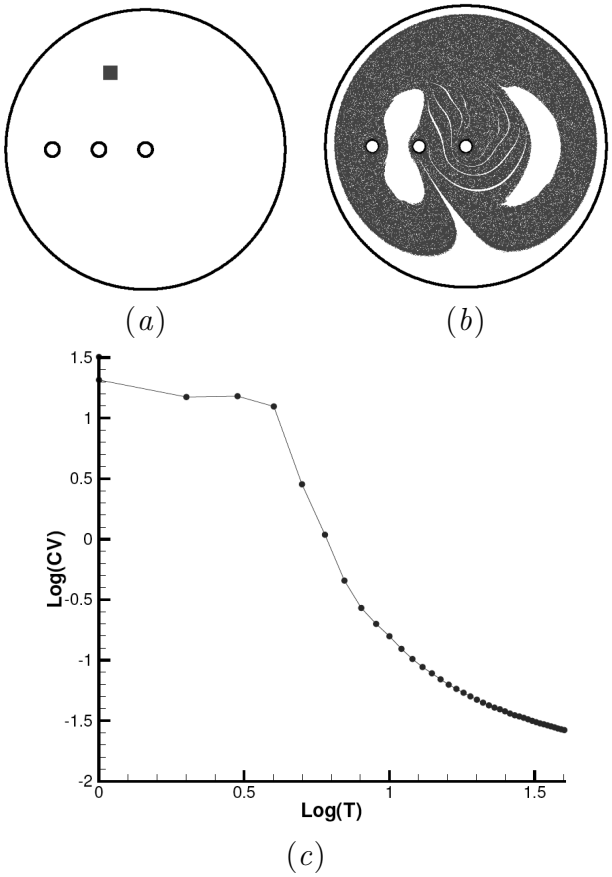

Figure 3.7: (a) The initial box of passive particles, (b) the stirred box after 20 periods of motion of the rods and (c) log-log plot of CV decay for system $PA1$.

of the stretching capability of the pseudo-Anosov system $PA1$ simply based on the topology of motion of rods, which does not require having a numerical simulation of the fluid flow.

3.1.2 Decay of concentration variance

Simulated homogenization of a blob of dye in system $PA1$ is illustrated in Fig. 3.7. There are different parameters that affect the calculation of CV and need to be tuned so that the results can be used as a measure of mixing and a basis for comparison of different systems. Investigations of section 2.4 show that $N_{pt} = 360'000$ and $d = 0.025$ can be used to calculate CV as a basis of comparison. Fig. 3.8 shows how CV decay in protocol $PA1$ depends on the location of the initial blob. It suggests that the three

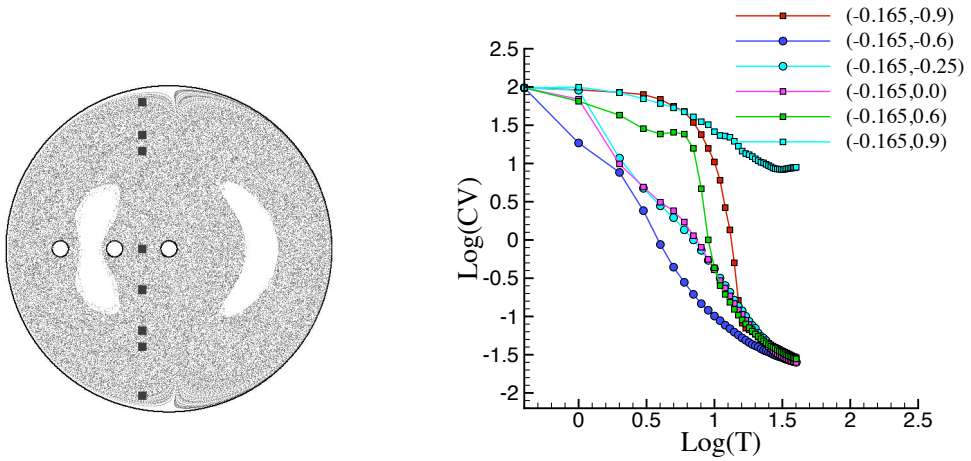

(a) (b)

Figure 3.8: Effect of initial location of the blob (a) on CV calculation (b). The legend for the CV diagram indicates the location of center of initial blob for each case.

following different regions can be recognized in a chaotic sea:

1. There is a region surrounding the central area of the chaotic sea, and locating the initial blob in this region produces the fastest short-term decay.

The approximate location of this region for protocol $PA1$ is $R_1 = \{(x, y)| - 0.25 < x < 0.25, -0.6 < y < 0\}$. The decay is approximately algebraic.

2. For a region far from the center and neighboring the outer boundary, considerable decay initiates only after a long time (about 30 periods). The approximate location of this region is $R_2 = (r, \theta)|r > 0.8$.

3. If the initial blob is chosen to be located in the rest of chaotic sea complementing R_1 and R_2, the initial decay is slower than in R_1 and faster than in R_2. After some periods of flow, a faster decay compensates the (so far) slow decay, and the concentration variance will eventually converge to that for R_1. Fig. 3.9 demonstrates how this happens for the case when the initial blob is located at $(-0.165, 0.6)$. Before period 7, even though the particles are concentrated in a small filament and causing large CV values, the filament has been stretched and the particles are homogenized inside it. Therefore after getting sucked into the heart of the mixing region during period 8, CV decay is faster than initial periods of homogenization of a blob initially

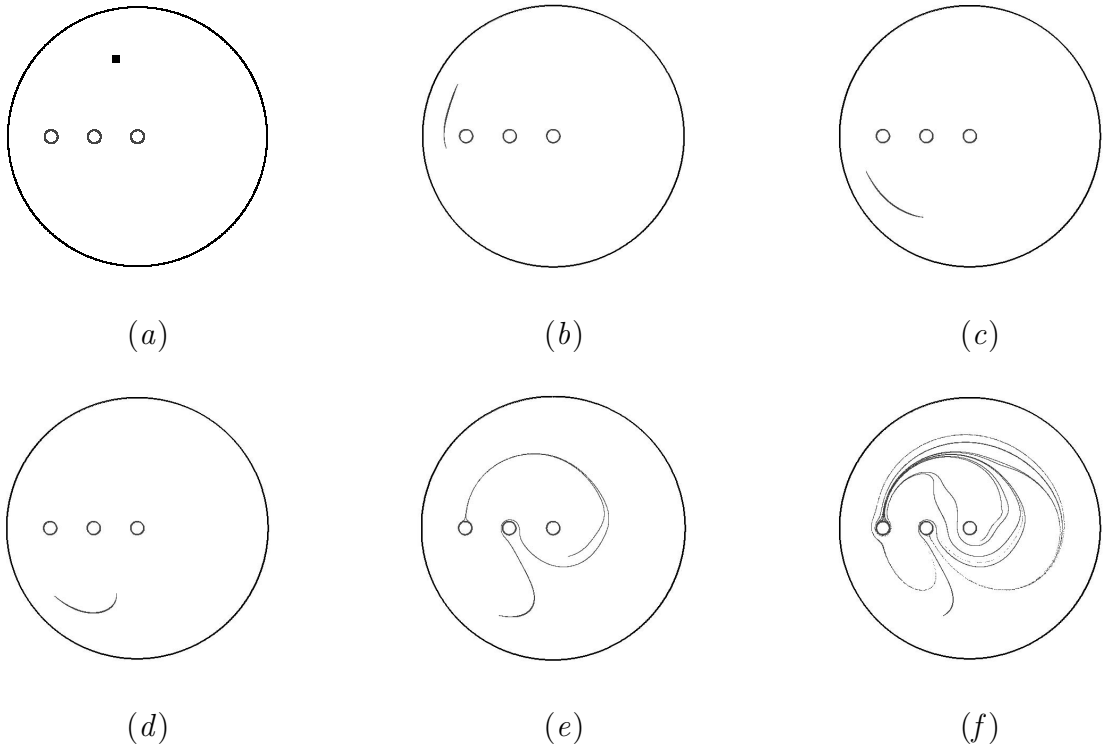

Figure 3.9: Step by step homogenization in system $PA1$, for a blob of dye that is not initially located in regions R_1 or R_2. The stirred blob is shown after (a) 0, (b) 3, (c) 5, (d) 6, (e) 7 and (f) 8 periods of the flow. The sudden decay of concentration after the 7^{th} period compensates for the initial slow decay.

located in region R_1.

As the CV diagrams show, initially the decay is faster due to exponential stretching and fast expansion of the mixing area. After 30 periods the decay becomes slower when the particles get homogenized inside the already occupied region. The overall trend is algebraic which is considered slow in comparison with an ideal exponential decay [54]. According to previous investigations by Gouillart *et al.* [30] the algebraic decay is the result of slow dynamics due to the zero velocity condition at the wall. The property of having a heart-shaped stretching figure that is extended to the no-slip wall is directly connected to the topology of motion of rods and the fact that their direction of rotation is opposite to each other. In the next section we study a system whose chaotic sea is protected from the no-slip wall.

3.1.3 The finite order counterpart of system $PA1$

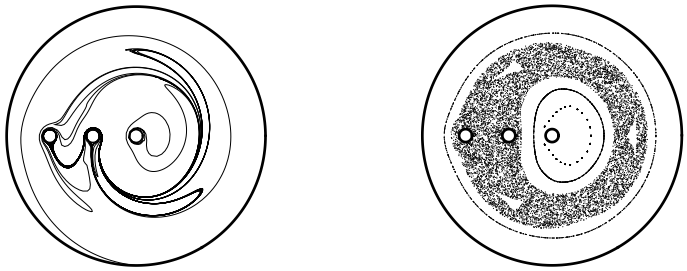

(a) (b)

Figure 3.10: Numerical simulation of system $FO1$. (a) The same initial material line as the one in Fig. 3.5 (a) stretched for 3 periods. (b) Poincaré section of the system generated by tracking a point in the chaotic sea and 3 points in different regular regions.

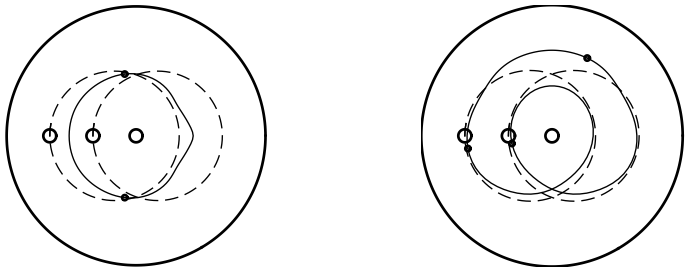

(a) (b)

Figure 3.11: Solid rod trajectories (dotted lines) and periodic orbits or 'ghost rod' trajectories (solid lines) in the $FO1$ system. (a) a pA 5-rod system composed of a period-2 orbit and the three solid rods for which $h_{TN} = 1.529$; (a) a pA 6-rod system composed of a period-3 orbit and the three physical rods for which $h_{TN} = 1.656$.

As explained earlier, for protocol $FO1$ (see Figs. 3.2 and 3.3), the eigenvalues of the corresponding matrix (Eq. 3.4) do not include a real number greater than one. Thus according to the TNCT it represents a *finite order* protocol for which topological chaos is not guaranteed. However the flow topological entropy calculated by numerical simulation of stretching (Fig. 3.10) is equal to 2.00 which is surprisingly greater than that of the pseudo-Anosov counterpart (protocol $PA1$).

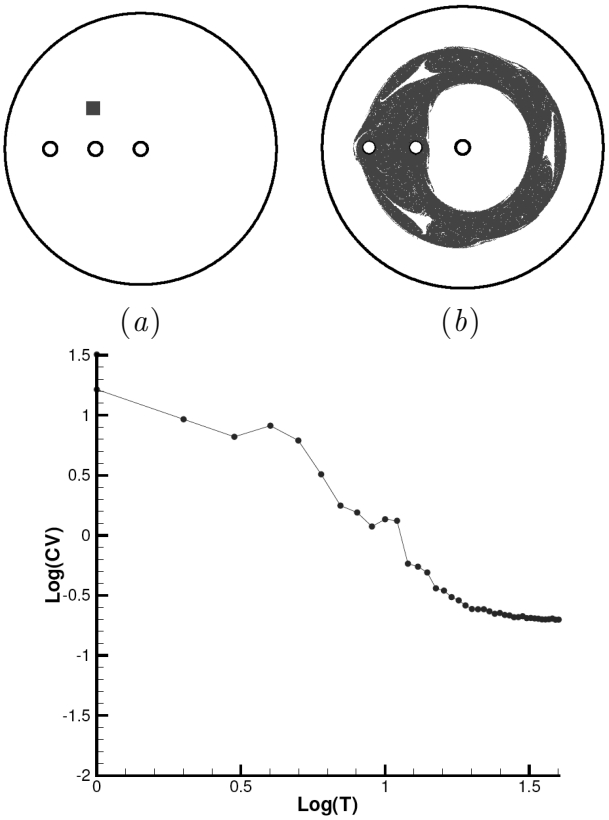

Figure 3.12: (a) The box of passive particles before stirring, (b) the stirred box after 20 periods of motion of rods and (c) log-log plot of CV decay for system $FO1$.

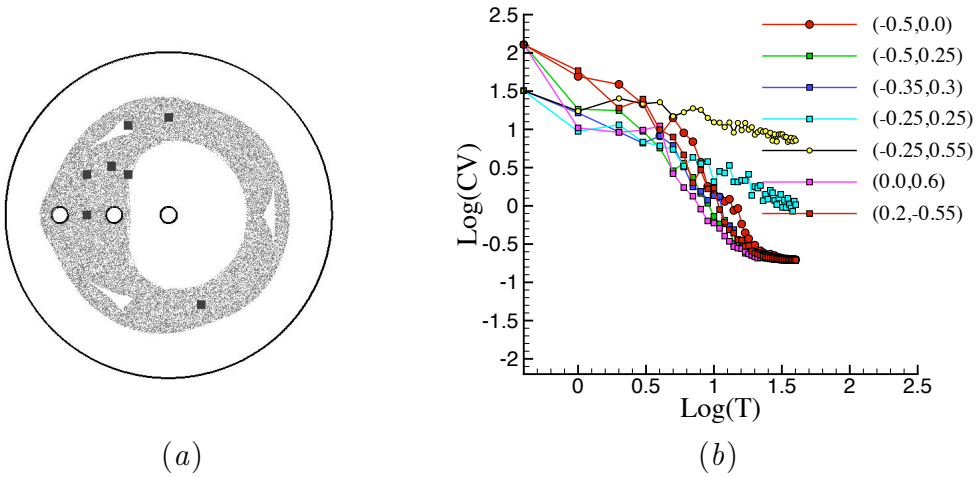

Figure 3.13: Effect of initial location of the blob (a) on CV calculation (b) for the finite order system $FO1$. The legend for the CV diagrams indicates the location of the center of initial blob for each case.

The surprising difference can be explained by the topological complexity produced by periodic points acting as 'ghost rods' [31]. There are several fixed points and period-1 points in the flow. However, the braid caused by any combination of these periodic points and the solid rods is always of finite order type. There are tens of period-2 and period-3 points in this flow. The braid caused by these periodic points together with the solid rods is examined here. Fig. 3.11 shows examples of period-2 and period-3 orbits of the flow that together with the solid rods cause a pseudo-Anosov type of braid. The TN lower bound of topological entropy produced by the braid of the resulting 5-rod and 6-rod protocols is demonstrated in the figure. The significantly large topological entropy of this flow is a result of the topological complexity caused by the combination of all the periodic points. Therefore combining different sets of these periodic points can lead to a closer estimation of the topological entropy of the flow using the TNCT. For example the 8-rod system obtained from the combination of the two sets of periodic points of Fig. 3.11 and the solid rods generates a pseudo-Anosov braid with $h_{TN} = 1.736$.

Fig. 3.13 suggests that for the finite order protocol, unlike the pseudo-Anosov protocol, different choices of initial blob, as long as they are located inside the chaotic sea, do not change the trend of decay. The two slower decay diagrams in the figure correspond to cases where the initial blob of particles is located at the verge of elliptic islands, so that a fraction of the particles are caught in the regular region. This might be related to the fact that the chaotic region in this flow is isolated from the no-slip walls and the stationary rod as the Poincaré section shows. More investigation of this observation is left for future work.

3.1.4 Geometric variations of the 3-rod protocols

The stretching patterns, e.g. the crescent shape islands of system $PA1$ and the large central island and the outer elliptic ring of system $FO1$, are results of specific dimensions and geometries involved and, as Figs. 3.14 and 3.15 show, they can be

changed by varying geometric parameters while the topology of motion of the solid rods is preserved. Furthermore, a review of mixing measures reported in table 3.1 shows how these geometric changes influence the mixing efficiency of the system. As a geometric constraint, the centers of rotation of the moving rods are located symmetrically on the left and right side of the central stationary rod, and the arm of rotation is the same for both rods. All dimensions for systems PAi and FOi are identical for the same i. Systems PAi and FOi, $i = 1, 2, 3$ are planned so that at $t = 0$ the rods are located equally spaced along the x axis, and the varying parameter is the distance between the rods at $t = 0$.

Poincaré sections show the shape of the region that a blob of particles initially placed in the chaotic sea will occupy after very long (theoretically infinite) time of running the system. Using a larger arm of rotation for the moving rods, or equivalently a smaller distance between the outer rod and the wall reduces the area of slow dynamics near the wall in systems PAi as a comparison of the Poincaré sections for $PA2$ and $PA3$ suggests (see Fig. 3.14). Consequently the Lyapunov exponent and the rate of CV decay increase. However because of the large distance between the rods in that case, emergence of regular islands becomes unavoidable. In systems FOi, if using larger rotation arms (see Fig. 3.15) causes the distance between the stationary rod and the rod next to it to become larger. As a result, an elliptic island emerges around the stationary rod and the island acts as a large rod. However, the size of the regular region next to the outer boundary so overall the chaotic sea gets bigger and CV decay is improved.

One can observe the trend of change in mixing measures and elliptic islands and modify the geometry toward an optimized mixing system. Improved systems $PA5$ and $FO4$ are attained using this procedure with the aim of minimizing the size of elliptic islands (unmixed regions) and simultaneously maintaining the mixing efficiency (based on the CV decay) at a high level. Using the information about variations of trend of CV decay for different initial conditions (sections 3.1.1 and 3.1.3), an average

Figure 3.14: Numerical simulation of different geometric variations of 3-rod pseudo-Anosov system $PA1$. First to fifth row belong to systems $PA1$, $PA2$, $PA3$, $PA4$, $PA5$ respectively. (a) images of the non-trivial material line of Fig. 3.5(a) stretched for 3 periods of the flow. (b) Poincaré sections. (c) the blob of particles (Fig. 3.7(a)) stirred for 20 period of the flow..

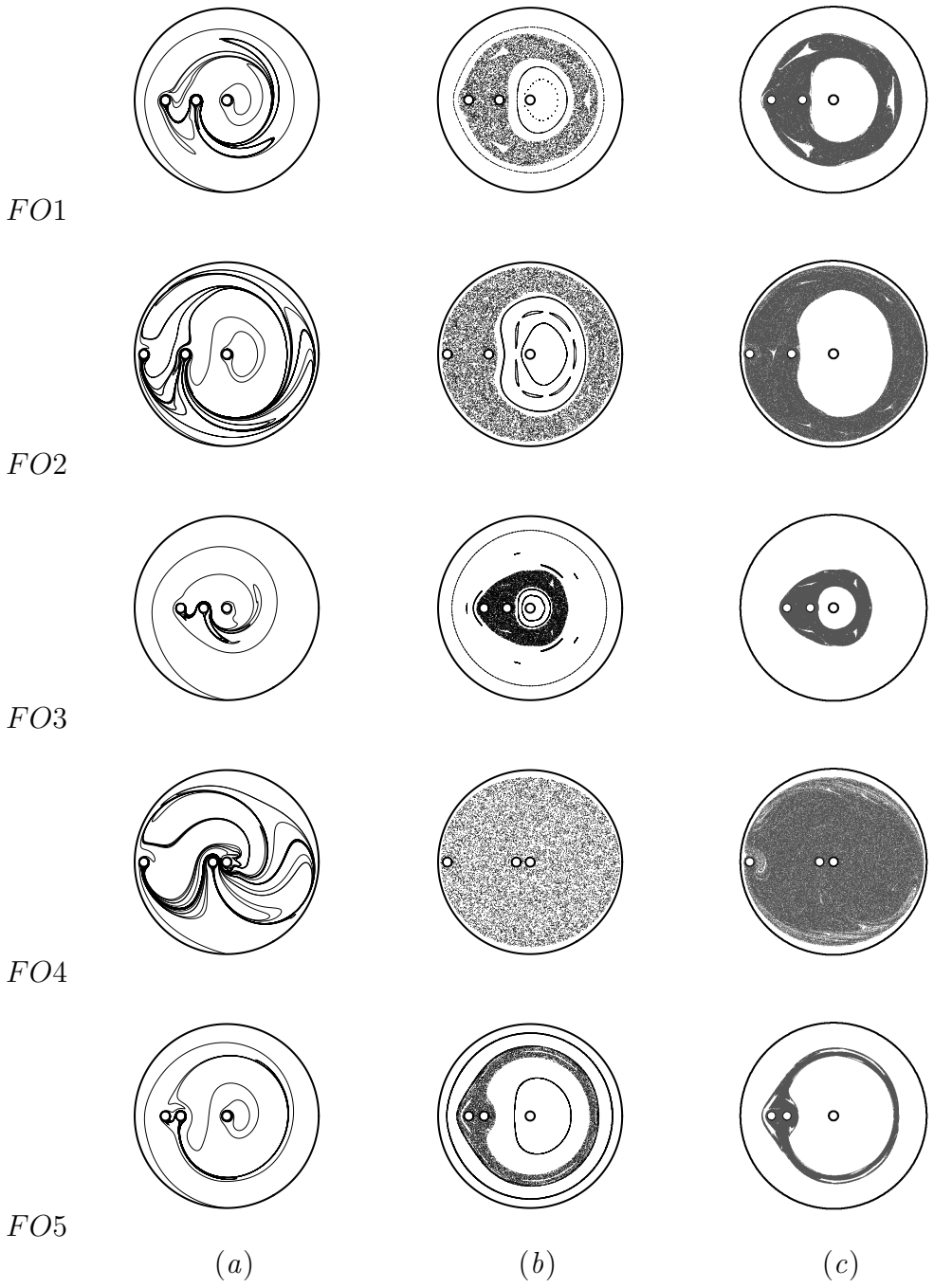

Figure 3.15: Numerical simulation of different geometric variations of 3-rod pseudo-Anosov system $FO1$. First to fifth row belong to systems $FO1$, $FO2$, $FO3$, $FO4$, $FO5$ respectively. (a) images of the non-trivial material line of figure 3.5(a) stretched for 3 periods of the flow. (b) Poincaré sections. (c) the blob of particles (Fig. 3.12(a)) stirred for 20 period of the flow.

of CV for region R_1 is used as a representative of each protocol's mixing efficiency and a basis for comparison of different protocols. Initially the CV decay is fast while the exponential stretching is expanding the size of the occupied region, which mainly happens within the first 20 periods. Then the decay considerably decelerates while the particles are becoming homogenized inside the occupied area. Consequently, values of CV at the 20^{th} period, $CV(20)$, quantify the short term stirring speeds as well as the general homogenization capability of the systems.

Fig. 3.16 gives a summary of the results of calculation of concentration variance for all the studied protocols. Concentration variance at the 20^{th} and 40^{th} periods ($CV(20)$ and $CV(40)$) quantify the short term and long term CV decay speeds respectively. Fig. 3.7 system $PA1$ at 20^{th} period when the concentration variance is approximately 0.05. It can be considered as the state of being nicely homogenized inside the chaotic sea and a base for comparison of the amount of time and energy needed for mixing in different systems. In Fig. 3.16 the amount of time, $T(CV = 0.05)$, and energy, $E(CV = 0.05)$, needed for each protocol to reach this goal is illustrated. The power input required to run any of the systems can be calculated using the coefficients of the semi-analytical series solution [27]. We calculate the energy input for one period of flow for each system and use the energy input for one period of operation of system $PA1$ as the scaling parameter, E^*. Systems $FO1$, $FO2$, $FO3$ and $FO5$ have large enough elliptic regions to prevent them from reaching $CV = 0.05$ after any period of flow.

Images and information of Figs. 3.15 and 3.16 illustrate that perturbations change the stretching and mixing characteristics of the finite order systems significantly, so that the same topology can generate a very small chaotic region or make the entire domain chaotic, and it can produce a fast or slow homogenization. In other words, even though tuning the geometric parameters of the finite order protocol led us to a surprisingly fast and energy-efficient mixing in system $FO4$, the mixing characteristics are not robust. This mainly happens because the stretching and mixing depend on

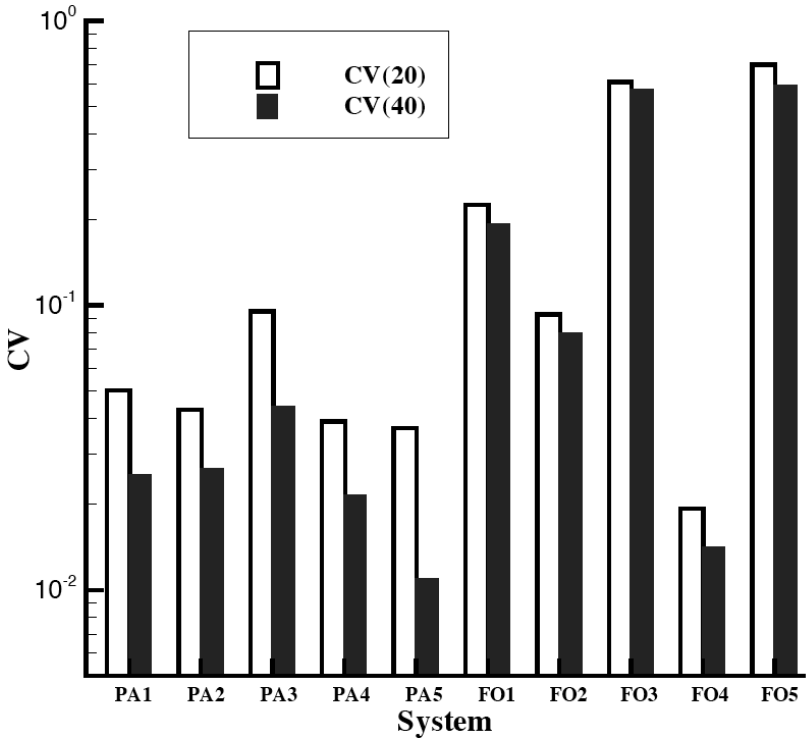

(a)

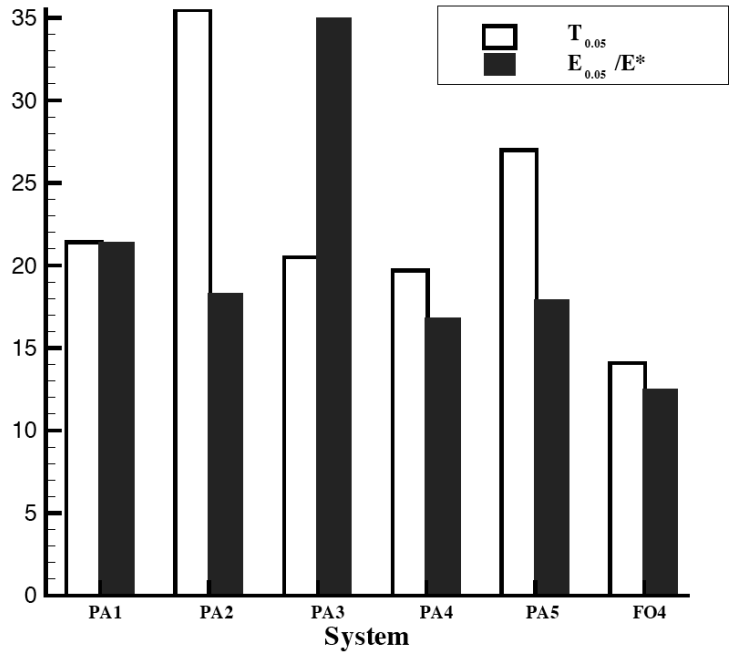

(b)

Figure 3.16: (a) Values of concentration variance for the different systems at the 20^{th} and 40^{th} periods of the flow. (b) The number of periods and the amount of (scaled) energy needed for each system to get to $CV = 0.05$. Systems $FO1$, $FO2$, $FO3$ and $FO5$ are unable to reach $CV = 0.05$ and thus are not shown.

Table 3.1: Measures of chaos for geometric variations of the pseudo-Anosov and finite order 3-rod systems.

System	h_{TN}	h_f	LE	$CV(20)$
$PA1$	1.76	1.76	0.66	0.047
$PA2$	1.76	2.09	0.71	0.038
$PA3$	1.76	1.76	0.48	0.095
$PA4$	1.76	2.04	0.65	0.047
$PA5$	1.76	1.90	0.57	0.027
$PA6$	1.76	2.09	0.49	0.154

System	h_{TN}	h_f	LE	$CV(20)$
$FO1$	0	2.00	0.63	0.244
$FO2$	0	2.20	0.70	0.096
$FO3$	0	1.83	0.68	0.603
$FO4$	0	2.10	0.82	0.021
$FO5$	0	1.91	0.53	0.703
$FO6$	0	1.59	0.34	1.855

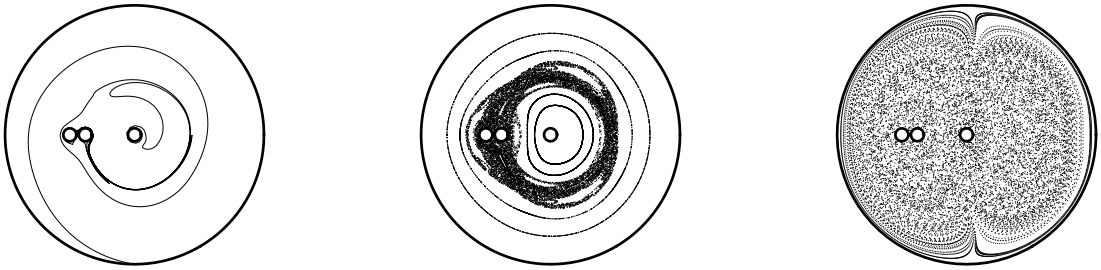

(a) (b) (c)

Figure 3.17: Numerical simulation of 'finite order' system $FO6$ and its pseudo-Anosov counterpart, $PA6$. (a) image of a non-trivial material line stretched for 3 periods of motion in $FO6$ and (b) Poincaré section for it. For this flow, $h \simeq 1.59$ and $LE \simeq 0.34$. (c) Poincaré section for system $PA6$ with $h \simeq 2.09$ and $LE \simeq 0.49$

the periodic orbits of the flow, and these orbits depend on the details of the fluid dynamics. On the other hand, in the pseudo-Anosov systems (Fig. 3.14) the mixing characteristics are mainly defined by the topology of motion of the solid rods, therefore they are more consistent and robust as long as the topology of motion is preserved. Overall comparison of the results shows that on average, the pseudo-Anosov systems have a better mixing efficiency in terms of the size of the chaotic area and the speed of homogenization.

With a finite order topology of solid rod motion, some geometries generate very poor stretching and mixing. The topological entropy of system $FO6$ (Fig. 3.17), $h \simeq 1.59$, is less than $h_{TN} \simeq 1.763$ predicted for the PAi protocols. In other words,

with the same topology of motion of solid rods that created the highly efficient system $FO4$, a system can stir less than any of its pseudo-Anosov counterparts. The chaotic region for the pseudo-Anosov counterpart of this system, $PA6$, fills the whole domain with no elliptic islands (Fig. 3.17). Its stretching rate ($h \simeq 2.09$) and homogenization ($CV(20) \simeq 0.154$) make it a much more efficient system compared to $FO6$.

In overall it can be said that the two three-stirrer braids of PAi and FOi are expected to give significantly different results based on the topology of motion of the solid rods. However, due to the existence of periodic points of the flow acting as 'ghost rods', under some conditions the topologically 'trivial', or finite order, protocol produces a larger stretching rate than does the pseudo-Anosov protocol. The existence and importance of these ghost rods is dependent on the specific system geometry, and the system may produce very low stretching rates and weak mixing characteristics when using the finite order protocol. In contrast, selection of a pseudo-Anosov protocol leads to a robust minimum for the stretching rate (as guaranteed by the TN theorem) as well as consistent mixing patterns. Overall comparison of the PAi and FOi ($i = 1, 2, ..., 6$) results show that also more effective mixing in terms of the speed of homogenization, the final accessible homogenization and the area of the mixing region (chaotic sea) happens in pseudo-Anosov systems relative to finite order systems. This case study confirms that even though periodic points are important players in producing complexity, examining the topology of motion of solid rods using the TN classification theorem prior to numerical simulation of the fluid flow is greatly advantageous in the selection of appropriate mixing protocols.

3.2 Other n-rod stirring systems

This section aims to study viscous flow mixing using different n-rod systems with protocols that are variations of the common three- and four-prong taffy pulling protocols (see the three-prong taffy machine of Fig. 3.1).

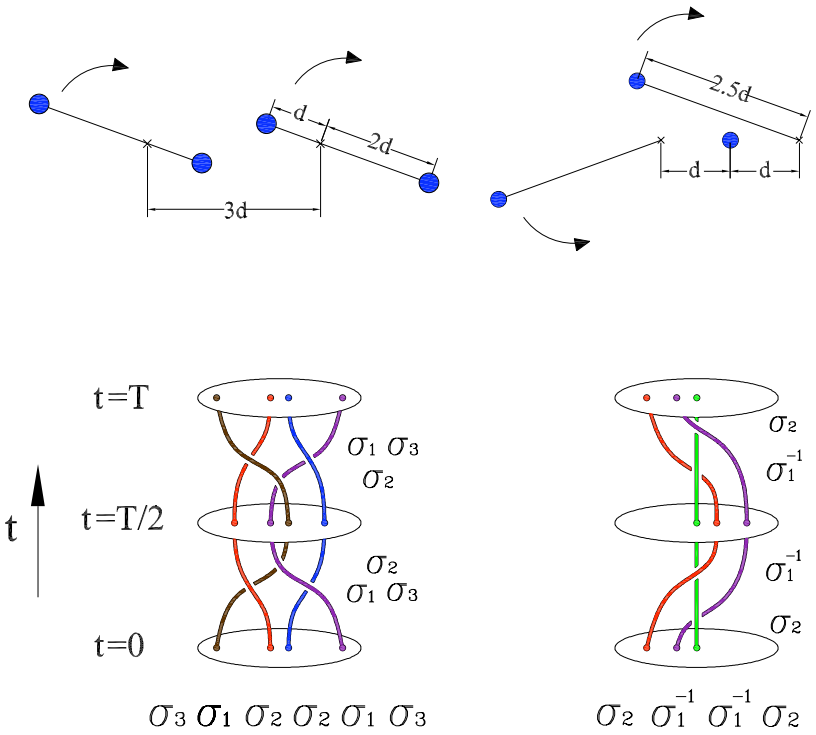

Figure 3.18: Up: stirring protocols of 4-rod system A (left) and 3-rod system B (right); down: their physical braids; braid letters for each crossing of the strands and braid word for each protocol are shown.

Fig. 3.18 shows two common taffy puller protocols studied here as fluid stirring systems and their corresponding braids. System B has the same topology of motion as $PA1$ (section sections) with $\lambda_{TN} = 3 + \sqrt{8} \simeq 5.83$. However, its dimensions are a little different from $PA1$ and are determined according to the experimental device of Fig. 3.27. The matrix calculation for the braid of protocol A involves 3×3 matrices. It is the result of respective action of σ_3, σ_1, σ_2, σ_2, σ_1 and σ_3 (Fig. 3.18). Following the method of Boyland *et al.* [9], the matrix representation for σ_1, σ_2 and σ_3 is respectively

$$M_1 = \begin{bmatrix} 1 & 1 & 0 \\ 0 & 1 & 0 \\ 0 & 0 & 1 \end{bmatrix}, M_2 = \begin{bmatrix} 1 & 0 & 0 \\ 0 & 1 & 1 \\ 0 & 0 & 1 \end{bmatrix} and\, M_3 = \begin{bmatrix} 1 & 0 & 0 \\ 0 & 1 & 0 \\ 0 & 1 & 1 \end{bmatrix}. \qquad (3.8)$$

Protocol A is represented by the product of the corresponding matrices:

$$M_A = M_3 M_1 M_2 M_2 M_1 M_3 = \begin{bmatrix} 1 & 4 & 2 \\ 0 & 3 & 2 \\ 0 & 4 & 3 \end{bmatrix}. \tag{3.9}$$

The biggest eigenvalue of M_A, $\lambda_{TN} = 3 + \sqrt{8} \simeq 5.83$, gives the stretching rate in the most unstable direction. Therefore this is a pseudo-Anosov protocol with the same TN stretch rate as the 3-rod system B. These numbers, calculated based on the topology of boundary motions, approximate the amount of complexity existing in the fluid motion.

For larger number of stirrers finding the corresponding matrices gets complicated. In order to find the braid word, a movie of the motion of rods (or ghost rods) in the domain over one period of the flow is prepared and all the over- and under-crossings that happen in one period are observed. There is a software created by T. Hall [33] which calculates the stretch rate of a given braid word. Using this software, it is possible to determine the TN class and TN topological entropy for protocols involving more than three stirrers.

3.2.1 Numerical simulation and computation of chaos measures for the n-rod systems

This section starts the study of topological chaos and mixing in n-rod stirring systems where $n > 3$, by comparing the mixing characteristics of the 4-rod protocol A with the 3-rod protocol B. Despite having different mechanical setups, protocols A and B have the same lower bound of stretching rate based on their braids. Here a numerical simulation of the flow is used to see the differences in stretching and mixing in these flows. Images of different stages of stirring of system A obtained by numerical simulation are shown in Fig. 3.19. Also the Poincaré section for this system, obtained by tracking a single particle trajectory for 50000 periods of flow, is given in the figure.

Both systems A and B (see Figs. 3.5 and 3.6 for stretching images and Poincaré

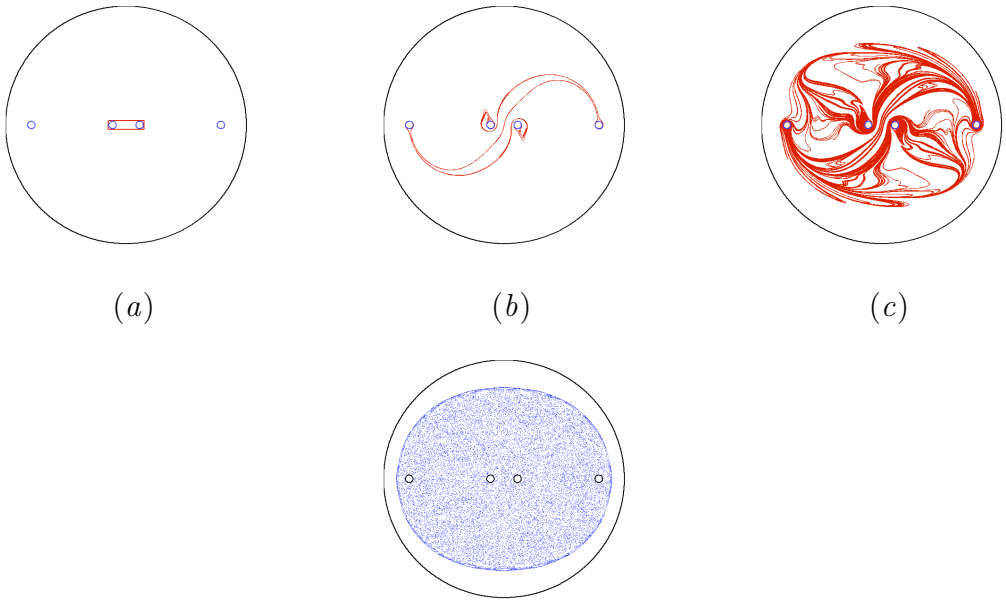

(a) (b) (c)

(d)

Figure 3.19: Numerical simulation of system A. Images of a non-trivial material line after being stretched for (a) 0 period with a length of L_0, (b) 1 period with a length of $L_1 \simeq 17.3L_0$ and (c) 5 periods with a legth of $L_5 \simeq 26632L_0$. (d) the Poincaré section.

section of system $PA1$ which is quite similar to system B) have a big chaotic region, the area that will be perfectly mixed after (theoretically) an infinite number of periods of motion. Regular regions of different shapes and sizes can be seen in the Poincaré sections as well. As time goes on the stretched material line (or equivalently the mixed blob of dye) in system B fills up the whole domain except for two crescent-shaped empty regions on the right and left side of the center. First the upper half of the domain ($y > 0$) is filled by the filament, while the lower half needs more time to be filled. The resulting 'heart' shape and cusp are directly related to the path of the two moving rods and the fact that they rotate in opposite direction relative to each other. The 4-rod system A shows a different behavior. There is a ring-shaped region next to the boundary that the stretched material line (or the simulated blob of dye) will never fill, so that the mixing area is isolated from the no-slip wall. There are four smaller regular regions inside the mixing region. In this system the simulated dye is equally distributed between the upper and lower halves of the domain.

Long-term effects of these behaviors are clearly seen in the Poincaré sections of the flows. The outer limit of the chaotic sea in system A is shown and four tiny elliptic islands are seen that are counterparts of the four "empty" regions observable in the stretching images. In contrast, the Poincaré section of system B confirms that after a long time, the simulated blob of dye will fill the fluid domain all the way to the outer boundary. The particles close to the boundary exhibit slow, semi-regular motion as can be anticipated from the zero-velocity boundary condition on the wall. Some of these properties are connected to the topology of the protocol, while some of them are results of the specific dimensions and geometries involved and can change for a single topology of motion of solid rods. For instance, if one changes the amplitude of the rotation of the rods in system B, with the same braid, it is possible to make the moving rods cover a portion of the crescent shape regions and reduce their size or eliminate them (Fig. 3.14). In section 3.2.2 we will see the effect of geometric perturbations on system A.

Stretching rate (λ) and topological entropy of the flow h_f are defined according to Eqs. 1.4 and 1.6 respectively. Fig. 3.20 shows the plot of the logarithm of the length of a non-trivial material line against the time period for both systems. The curve quickly converges to a straight line. h_f is equal to the slope of this line and $\lambda = e^{h_f}$. For system A, $h_f = 1.82$, and for system B, $h_f = 1.93$, while the TN prediction for the lower bound for both systems is $h_{TN} = 1.76$. Despite the 3% percent (system A) and 9% percent (system B) difference between the theoretical prediction and the actual flow entropy, it can be said that TN theorem gives a valuable estimate of the stretching capability of these systems simply based on the topology of motion of rods.

The largest Lyapunov exponent (LE) of the system is another measure of chaos shows the average of the rate at which nearby points separate (see section 1.5). Fig. 3.21 shows the calculation of LE for systems A and B. In this calculation the trajectory of a point and a second point in very small distance from it are tracked. At each time step, LE is obtained by taking the logarithm of the distance between the two

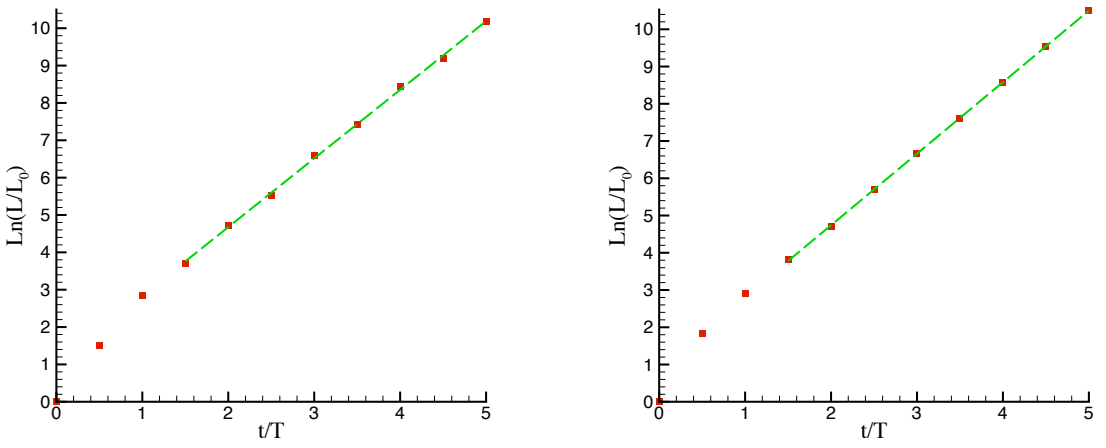

(a) (b)

Figure 3.20: Calculation of topological entropy (slope of the line) of the flow for (a) system A, $h_{f,A} \simeq 1.84$ and (b) system B, $h_{f,B} \simeq 1.92$.

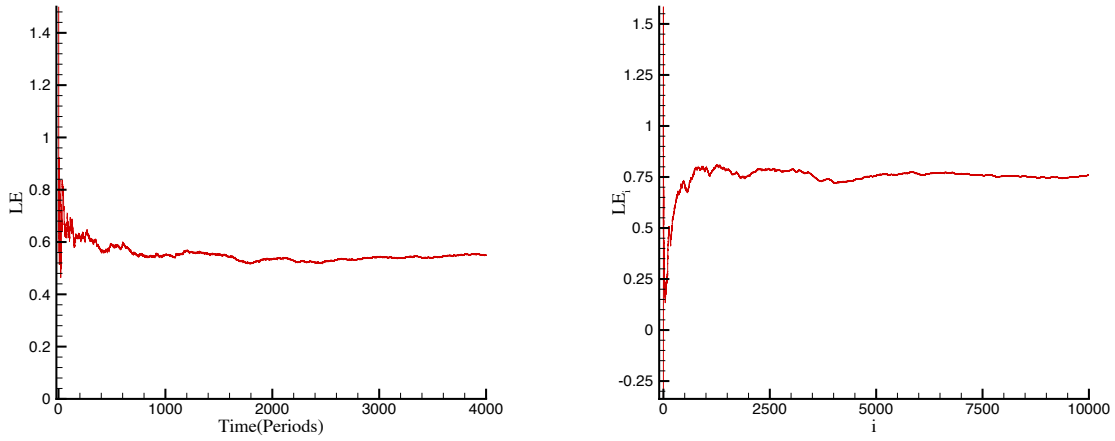

(a) (b)

Figure 3.21: Calculation of Lyapunov exponent of the flow for (a) system A, $LE_A \simeq 0.55$ and (b) system B, $LE_B \simeq 0.75$.

points scaled by the original distance. In order to be able to evaluate the exponential divergence, at each time step the second point should be redefined by scaling the new distance between the point by the original distance. For systems A and B, the values of LE converge after about 3000 an 5500 periods of the flow, respctively. The value of

LE is always lower than h_f and a smaller difference between the two numbers (larger LE) shows more uniformly distributed stretching (Table 3.2). Systems A and B have the same h_{TN}, while according to the numerical calculation of topological entropy of the flow, h_f, they generate different amounts of stretching. System B with only two moving rods, shows a larger stretch rate with a much more uniform distribution of the stretching over the chaotic region according to the values of the Lyapunov exponent and in agreement with stretching images of Figs. 3.14 and 3.19.

The stretching and mixing of other n-rod systems derived from protocols A and B are studied here. As the simulations of section 3.1.4 show, the finite order counterpart of system B with the two moving rods rotating in the same direction, normally has large unmixed or poorly mixed regions. However, this protocol can be converted to a pseudo-Anosov one only by adding two fixed rods as shown in Fig. 3.22. The mixing performance of the resulting 5-rod protocol, system C, with $_{TN} \simeq 2.12$ is investigated. The Poincaré sections and stretching images of section 3.1.4 suggest that in most FOi protocols, the central fixed rod does not play a role in stirring. Numerical simulation of the 2-rod finite order protocol D is accomplished to explore this fact with more details. The stretching performance of 8-rod system E constructed from two 4-rod protocols A is also investigated to observe how doubling the mechanism changes the stretching and mixing performance (Fig. 3.22).

Table 3.2: Measures of chaos for different n-rod systems

System	h_{TN}	h_f	LE
A	1.76	1.82	0.55
B	1.76	1.93	0.75
C	2.12	2.16	0.53
D	-	2.02	0.66
E	?	2.60	0.88

Fig. 3.23 shows the stretching patterns and Poincaré sections generated by protocols C, D and E and a summary of various chaos measures is given in table 3.2. By

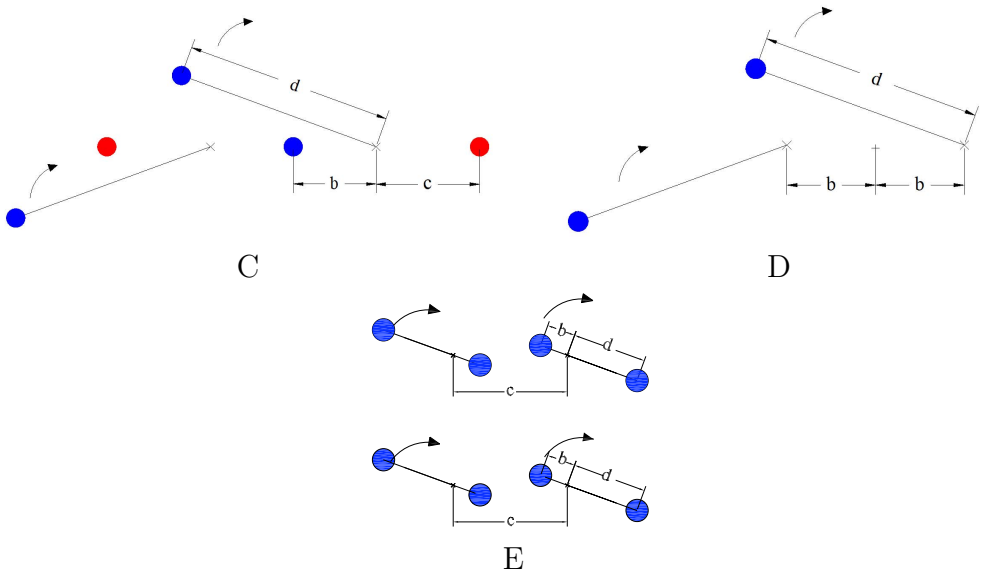

Figure 3.22: Protocols C, D and E (See the text for explanation).

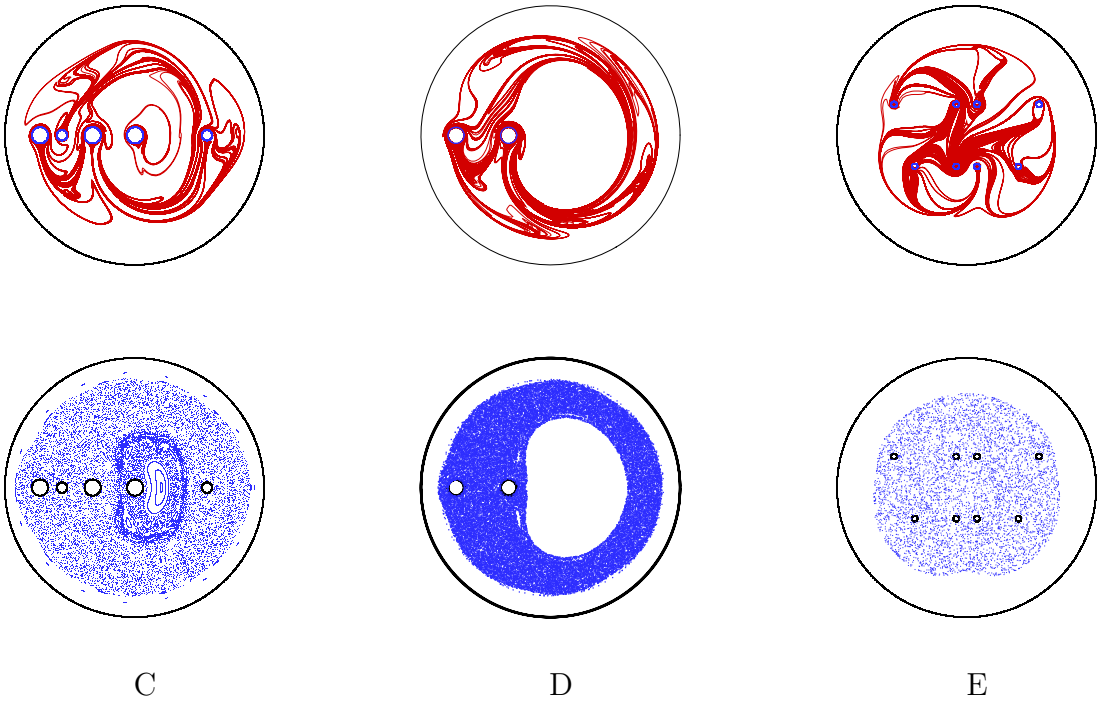

Figure 3.23: Numerical simulation of stretching for n-rod systems C, D and E (see description in text). Upper row: Images of a non-trivial material line stretched for 3 periods of flow. Lower row: Poincaré sections.

adding two (smaller) fixed rods to protocol $FO1$, this finite order protocol is converted to the pseudo-Anosov protocol C. These added rods cause a complicated mixture of

regular and chaotic dynamics around the central fixed rod. This braid generates a high rate of stretching, with $\lambda_{TN} \approx e^{2.12} \approx 8.33$. However, this stretching is much less uniform compared to the 3-rod $PA1$ protocol as its stretching image (Fig. 3.23) and a comparison of the Lyapunov exponents (table 3.2) illustrate. The 8-rod system E, composed of two copies of the 4-rod protocol A, generates a high rate of stretching, with $\lambda \approx e^{2.6} \approx 13.46$ and Lyapunov exponent $LE \approx 0.88$. Similar to system A and $FO1$, because of the same-direction rotation of rods, there is a regular ring-shaped region separating the chaotic sea from the outer boundary of the fluid domain. The simple 3-rod protocol B, while using only two moving rods and a fixed rod, generates a high amount of uniformity distributed stretching relative to other n-rod stirring systems.

3.2.2 Effect of geometric modifications on the 4-rod system

Figure 3.24: 4-rod system A_2, result of stretching of a material line after 7 periods and its Poincaré section.

Table 3.3: Chaos Measures for different 4-rod systems

System	h_{TN}	h_f	LE
A	1.76	1.82	0.55
A_2	1.76	1.81	0.68
A_3	1.76	1.83	0.72

As mentioned in the previous section, some of the properties of a stirring system

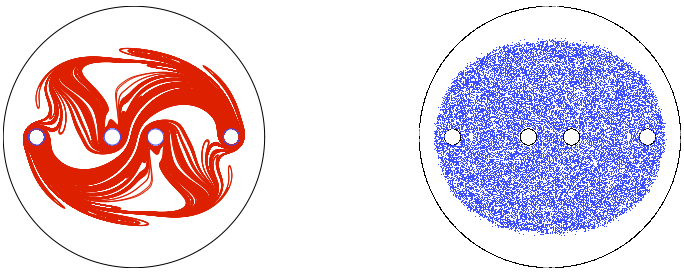

Figure 3.25: 4-rod system A_3 (see the text for explanation); stretching of a material line after 5 periods and the Poincaré section.

can be modified by changes in the geometric parameters of the system while maintaining the same topology. Geometric parameters of the 4-rod system A were chosen based on the available 4-rod experimental device of Fig. 3.26. Slight modifications in the parameters of the motion of rods (Figs. 3.24 and 3.25) can improve efficiency of this system. The arms of rotation of two of the rods are modified to obtain system A_2. System A_3 is the same as system A_2 but its rod diameters are larger. The stretching rate is almost unchanged in agreement with the fact that it is in direct relation with the topology of the rod motions. This consistency is further evidence that the stretching rate of pseudo-Anosov protocols is relatively robust against geometric perturbations. However a more uniform distribution of stretching is obtained in systems A_2 and A_3 relative to A which is evident from the stretching images and the values of Lyapunov exponent. See table 3.3 for a summery of different chaos measures for these 4-rod systems.

3.3 Rod-stirring experiments

Different experiments have been accomplished [1]. The 4-rod experimental device consists of an approximately foot-long rectangular container of glycerin (Fig. 3.26). Two pairs of rods are powered by two distinct motors. The flow is slow and approximately

[1] by colleagues in our research group: Alec Calhoun, Kellen Shain, Anthony Nelson and Matthew Bokulic

two-dimensional. A streak of dye is stirred with $Re \simeq 1$ in Glycerin. In the figure the experimental images are compared to the images of the numerical simulation at the same instants of time. The streak of dye is modeled with a small rectangle of passive fluid particles surrounding two of the rods which is a non-trivial material line. Since a semi-analytical solution is not available for a rectangular domain, the simulation assumes a circular boundary with the same area as the rectangular domain. In spite of this difference, and also the difference between the type of initial streak of dye in the experiment and the numerical simulation, a good agreement is observable.

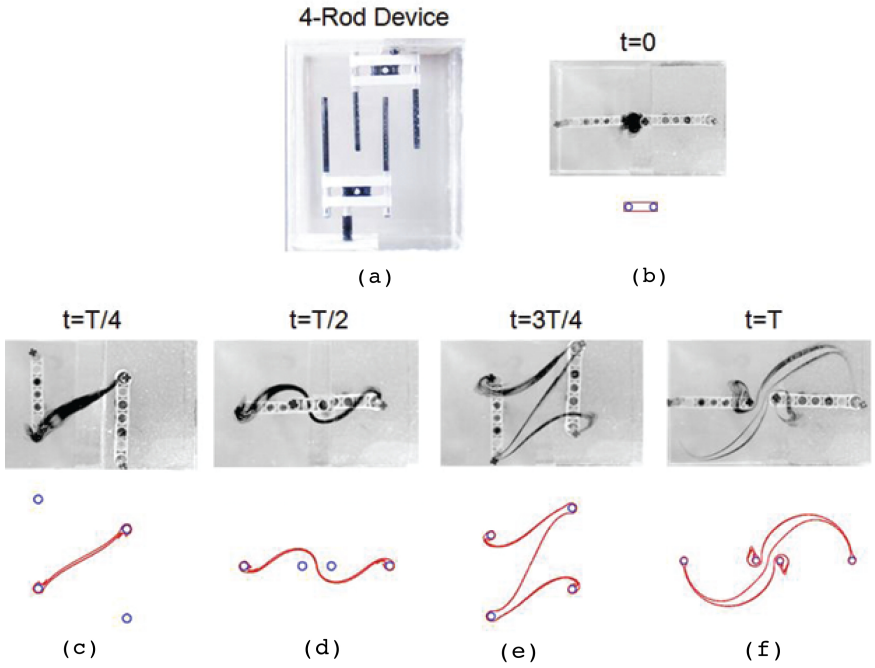

Figure 3.26: (a): The 4-rod system experimental device. The stirring experiment and comparison to the numerical simulation for (b) 0, (c) $\frac{1}{4}$, (d) $\frac{1}{2}$, (e) $\frac{3}{4}$, (f) 1 period(s) of motion.

Experimental stirring for the 3-rod system in a cylindrical device has been carried out as well (Fig. 3.27). Interestingly, images from the numerical simulation and the experiment at the fifth period share the same features even in very small details. In the experiment, some of the dye was initially placed in the left elliptic island which causes a slight difference between the experimental and numerical images in that

region of the domain. This portion of dye is not stretched and folded, in agreement with the fact that the dynamics is regular in the island.

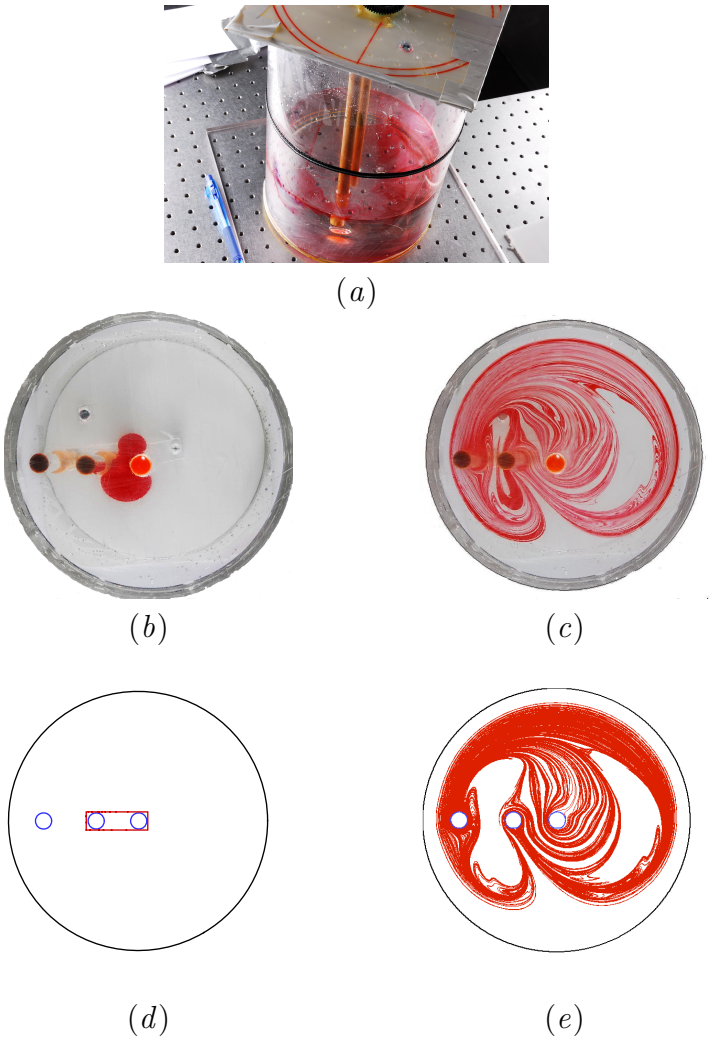

Figure 3.27: (a) The 3-rod system experimental device. (b) The initial blob of dye and (c) the blob stirred for 5 periods of the flow in the experiment. (d) The initial blob of dye and (e) the blob stirred for 5 periods of the flow in the numerical simulation.

4

Study of the relationship between stretching and homogenization via mixing in a lid-driven cavity flow

The topological entropy, or logarithm of the stretching rate, is a measure of chaos that can be stated as a characteristic number for a chaotic mixing system. However, high stretching rate is not always a sign of proper mixing. This chapter considers the homogenization which is the core objective of stirring, and studies the relationship between stretching and homogenization in chaotic Stokes flows. To illustrate this, a double-lid-driven cavity flow is used as an example, in which perturbing a parameter changes the nature and behavior of "ghost" stirrers and leads to variations in the topological entropy and the rate of homogenization. A set-oriented approach and lobe dynamics techniques are employed to explain the homogenization caused by stirring.

In this dissertation, the focus is on chaotic flows in which the particle trajectories are deterministically chaotic while the velocity fields are always periodic and therefore non-chaotic. Chaos causes the distance between every two initially neighboring points of the chaotic sea to grow exponentially. As a result, if the neighboring passive particles are attached together with a material line, the length of the line has to grow exponentially in the long-term. This chaotic stretching of material lines is the basis

on which the well-known measure of chaos for mixing systems, topological entropy, is defined. Now instead of the material line, if a box of passive material, like a drop of dye, is placed in the chaotic sea, the exponential separation of neighboring points spreads the particles in the domain and "homogenizes" the mixture. In miscible fluids, molecular diffusion completes the process of mixing [66, 30].

The stretching rate of a system in long term asymptotes to a number that is a characteristic of the system i.e. it is mainly independent of the initial position of the non-trivial material line. Stretching is the result of stirring caused by topology of motion of the boundaries [9] or ghost rods [31, 65], and therefore it can be measured using a limited amount of topological data without including any details of the fluid dynamics [9]. A chaotic flow always generates exponential stretching. However, there is no guarantee for higher stretching rate to be a sign of better mixing (chapter 3). Homogenization, on the other hand, is the objective of stirring, and with the help of diffusion, higher homogenization is always a sign of better mixing. A universal measure of homogenization is difficult to define and there has not been an abstract or topological way of prediction for that. One of the most common measures of homogenization is the concentration variance (CV) [18]. Decay of CV is not necessarily exponential for chaotic flows (see section 3.1.4 and [30]) and depends on the initial conditions and the parameters of calculation (see section 2.4 and [45]. However, by using CV decay rates it is possible to compare structurally similar systems (for example, systems formed based on the variations of a parameter) or compare the performance of a single system under different conditions, similar to the analysis of chapter 3.

Here the question arises: Is it possible to design for proper mixing based on the topological entropy? Or what is the relation between chaos and mixing? Good homogenization is a result of chaotic separation of neighboring points; hence there should be some correlations between the stretching and homogenization. However, there is not a direct mathematical correspondence between the two [53]. For two

reasons the homogenization in a high-stretching flow might be poor: first, existence of elliptic islands that are regions empty of chaos, and second, the dynamics can be slow or fast in different regions of the domain causing inhomogeneity (see section 3.1.2 and [30]). The reverse does not happen though: weak stretching could not be followed by fast homogenization.

This chapter studies the relationship between chaos in terms of stretching of material lines, and mixing in terms of homogenization of a passive scalar in the flow. The mixing behavior of different systems is explained based on the action of periodic points acting as ghost rods [31, 65] and using a set-oriented approach introduced in [65]. The chapter is structured as follows: section 4.1 describes the example system which is a variation of the cavity flow. Section 4.3 explains the method of evaluation of the homogenization and the trends of homogenization for different ranges of a parameter τ in the system. Section 4.4 investigates the correspondence between the homogenization and topological entropy. Section 4.5 uses the set-oriented approach to describe the mixing caused by ghost rods and explains the mixing behavior of this flow through the action of *almost invariant sets*.

4.1 The example system: a variation of the lid-driven cavity flow

In this study, the relationship between stretching and homogenization is observed using numerical experimentations on a chaotic laminar flow, for a suitable example which is appropriate for parametric study. This study also includes explanations for these observations based on the type and the role of "ghost rods" that are passive fluid particles responsible for stirring and generating chaos in some flows [31]. This example flow, streamlines for which are shown in Fig. 4.1, is a variation of the double-lid-driven cavity flow [65]. It is a time dependent two-dimensional Stokes flow in the rectangular domain $\{(x, y) : 0 < x < a, -b < y < b\}$ that is driven by velocity

boundary conditions on both bottom and top boundaries. On the bottom boundary

$$V(x,t) = \sum_{n=1}^{2} [U_n \sin(n\pi/a(x+\phi))], \tag{4.1}$$

with

$$\phi(t) = \{ \begin{array}{ccc} 2\pi & \text{for} & n\tau \le t \le (n+1)\tau/2 \\ 0 & \text{for} & (n+1)\tau/2 \le t \le (n+1)\tau \end{array} . \tag{4.2}$$

On the top boundary the velocity boundary condition is $-V(x,t)$. The flow pattern is

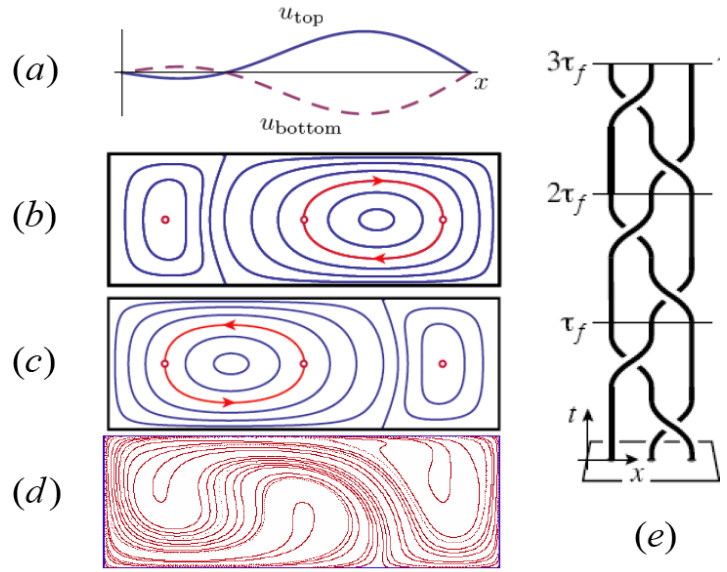

Figure 4.1: The double-lid-driven cavity flow for $\tau = 1.0$ adopted from [65]. Panels (a) show the velocity boundary condition for the first half period, (b) and (c) show the streamline structure with the points projecting the period-3 orbit for $n\tau < t < (n+1)\tau/2$ and $(n+1)\tau/2 < t < (n+1)\tau$ respectively. Solid circles mark points that are fixed and open circles mark points that move along the same streamline for the respective interval of time. (d) A material line initially along the x-axis stretched for three periods of the flow. (e) The topology of motion of the period-3 point generates a pseudo-Anosov braid as discussed in section 4.2.1.

reflected around $x = a/2$ every $t = n\tau/2$; therefore the velocity field is steady for each $\tau/2$ time-interval, and overall it is periodic with a period of τ. The streamfunction for a Stokes flow satisfies the bi-harmonic equation

$$\nabla^2\nabla^2\psi(x,y) = 0. \tag{4.3}$$

Following [48], an analytical solution for the velocity field can be found assuming a ψ of the form

$$\psi(x,y,t) = \sum_{n=1}^{2}(U_n C_n f_n(y)\sin(n\pi/a(x+\phi))). \tag{4.4}$$

Plugging this into 4.3 leads to

$$C_n = \frac{a^2}{2n\pi^2 b}[\frac{a}{2n\pi b}\sinh(\frac{2n\pi b}{a})+1]^{-1}, \tag{4.5}$$

and

$$f_n(y) = \frac{2\pi y}{a}\cosh(\frac{n\pi b}{a})\sinh(\frac{n\pi y}{a}) - \frac{2\pi b}{a}\sinh(\frac{n\pi b}{a})\cosh(\frac{n\pi y}{a}). \tag{4.6}$$

Then the Lagrangian particle trajectories are obtained from integrating

$$\begin{aligned} \frac{dx}{dt} = u(x,y,t) &= \frac{\partial\psi}{\partial y}, \\ \frac{dy}{dt} = v(x,y,t) &= -\frac{\partial\psi}{\partial x}. \end{aligned} \tag{4.7}$$

This is a two-dimensional, time-dependent dynamical system capable of becoming chaotic [3]. In order to study the chaos and mixing in this flow, the parameter τ is varied in the range of $[0.2,\ 2.0]$. In systems with small τ, the streamline pattern changes quickly, while systems with a large τ remain steady for a longer time. This study assumes a cavity with $a = 2\pi$ and $2b = 2\pi/3$ and with velocities $U_1 \approx 9.927856$, $U_2 \approx 0.841298U_1$. The selected aspect ratio and velocity ratio give a counter-rotating streamline pattern as Fig. 4.1 shows. With the chosen parameters in the flow and with $\tau = 1$, there is a period-3 point at the locations shown in Fig. 4.1 so that, for example in Fig. 4.1(a) the points at $(a, 0)$ and $(a + x_s, 0)$ lie on the same streamline and the point $(a - x_s, 0)$ is a fixed point. The period value $\tau = 1$ is a bifurcation point regarding the mentioned periodic orbits, as is explained in section 4.2.2.

4.2 Chaotic stretching of material lines

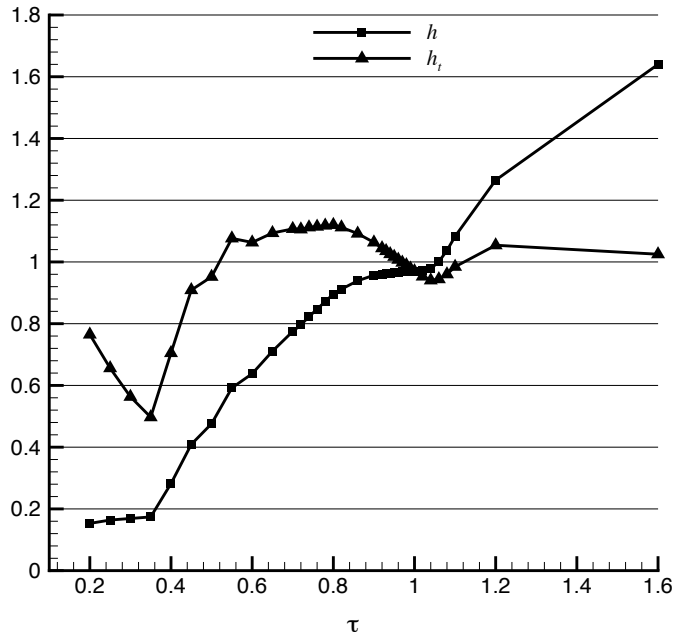

Figure 4.2: Topological entropy based on the elapsed number of periods (h) and based on the elapsed time (h_t).

Integrating equations 4.7 for any passive particle at the initial position (x_0, y_0) gives the Lagrangian trajectory of that particle and the location of the particle after any specified amount of time. Similar to computations of chapter 3, particle tracking leads to tracking of non-trivial material lines, visualizing the line stretching patterns and calculation of the stretching rate of different systems. For the example system of this chapter (see equations 4.4 through 4.7), a GSL (GNU Scientific Library) integrator is used with adaptive time step to track particles.

Tracking Lagrangian particle trajectories, also enables generating Poincaré sections for the flow with different values of parameter τ as shown in Fig. 4.7. The Poincaré section for $\tau = 1$ shows that except for three tiny regions, the rest of the domain consists of a chaotic sea. As it will be discussed in this section, these regions

are not elliptic islands but the dynamics are slow in them because of the type of periodic points existing at their centers. Therefore it can be said that a blob of particles will be distributed in the entire domain (i.e. homogenized) after sufficient time. For small τ (less than 0.65) there are larger elliptic islands in the Poincaré section that decrease the mixing area. In systems with τ slightly bigger than 1.0, three pairs of small islands appear which bifurcate from the three slowly mixing regions of $\tau = 1$. The size of these islands grows when τ is increased from 1 to 1.05, and then the size decreases until the islands are not visible in systems with τ greater than 1.3. The islands again appear for $\tau \geq 2$.

Stretching of non-trivial material lines advected by the flow are numerically simulated and the stretching rate for different τ is calculated. In this calculation a large number of particles form the material line and a point insertion algorithm is used to keep an appropriate resolution when the stretching causes the particles to move away from each other. Fig. 4.1 shows how an initially horizontal line is stretched after three periods of the flow. After sufficient periods of the flow, the stretching pattern is independent of the selection of the initial non-trivial line.

As described in section 1.5, the topological entropy is normally defined as the logarithm of the rate of stretching of a non-trivial material line defined per *period* of the flow: $h = Ln(\lambda)$ where $\lambda = L_{(n+1)}/L_n$ (L_n being length of the line advected for n periods of the flow) for a large enough n so that the stretching rate is converged to a constant number. However, since this work studies the mixing as the parameter τ changes, the amount of time that a system spends for the same number of periods varies. For applications in which the *time rate* of mixing is important, a new version of topological entropy

$$h_t = Ln(\lambda_t) \tag{4.8}$$

can be used where $\lambda_t = L_{(t+1)}/L_t$ (for a large enough t), is the rate of stretching per

time unit. With the definition 4.8, it is straightforward to conclude that

$$h_t = h/\tau \tag{4.9}$$

Fig. 4.2 shows the values of both h and h_t versus τ. Systems with larger τ use more time per period of motion to stretch the material lines. This behavior causes h to be a monotonically increasing function of τ, even though the nature and behavior of the ghost stirrers vary, as is studied in [65] and in sections 4.2.1 and 4.2.2. The entropy h is, to a large extent, generated by the topology of motion of the stirrers (see chapter 3 and [9]) while h_t is determined by both the topology and the value of the parameter τ. The entropy h_t compares the amount of stretching for the same amount of time in different systems and, unlike h, is not a monotonic function of τ. Studying the fluctuating behavior of h_t along with the variations in the rate of homogenization and behavior of the ghost rods is insightful in understanding the mixing in chaotic flows.

4.2.1 Topological chaos due to ghost rods

The stretching in the cavity flow can be explained in the context of topological chaos. Chaos in laminar flows often can be associated with the stirring caused by solid or ghost rods (see chapter 3 and [9, 31, 65]. Material lines are entangled by these stirrers and consequently are stretched. The topology of motion of these stirrers can be tuned so that a higher value of stretching is obtained. Also, the geometry of their motion can be tuned to give the optimal rates of homogenization (section 3.1.4). Since there is no physical stirrer in the cavity flow, we look for periodic points or elliptic islands that accomplish the stirring as ghost rods. Fig. 4.1 shows the trajectory of the parabolic period-3 points of the flow for $\tau = 1$. For the first half period ($0 < t < 0.5$), the left point is stationary while the other two switch positions. For the second half period ($0.5 < t < 1$), the right point is stationary while the two left points switch positions. The physical braid caused by motion of these points in the flow is shown in Fig. 4.1. Its mathematical representation is $\sigma_1^{-1}\sigma_2$, which using the matrices of section 3.1.1

and based on Thurston-Nielsen classification theorem, is a pseudo-Anosov braid with $h_{TN} = \ln(\frac{3+\sqrt{5}}{2}) \approx 0.962$. The calculated value of h for the flow with $\tau = 1$ is 0.97. Therefore, applying TNCT to the motion of these ghost rods predicts the stretching with a good agreement. Also, the stretching pattern shows that these periodic points are really pulling the material lines similar to physical stirrers.

When τ is increased beyond 1.0, the parabolic periodic point bifurcates to a set of two hyperbolic and two elliptic periodic points (Fig. 4.9). The whole set of four points travel together in the shadow of the path of the original parabolic point [65]. As the Poincaré section suggests, the dynamics inside and around the ghost rods are slow. However, as Fig. 4.2 shows, the stretching per period is monotonically increasing.

4.2.2 Almost invariant sets as ghost rods

Almost Invariant Sets (AIS) are macroscopic leaky structures preserved by the dynamics that divide the domain into different regions with relatively small amount of transport between them [19, 65]. Their space-time trajectories are periodic, making them capable of periodic braiding of the flow and generating topological chaos. Particle trajectories will eventually 'leak' from an AIS to the other one.

In order to identify the AIS, one needs to use the discretized Perron-Ferobenious transfer operator which is the same as Ulam matrix, P, introduced in section 2.3. The entries of the reversible Markov matrix, M, are defined as

$$m_{ij} = p_{ij}\frac{V_j}{V_i}, \tag{4.10}$$

in which V_i is the i^{th} element of the eigenvector of P corresponding to its largest eigenvalue [19]. Since all the points in the domain are mapped to points inside that are in the same domain, the largest eigenvalue is always 1. The AIS are the eigenvectors of M and the eigenvalue corresponding to each eigenvector is a measure of leakiness of the AIS. The set corresponding to the largest eigenvalue, 1, is the whole domain which is an invariant set. The AIS images in Fig. 4.7 show how the domain is

divided into almost invariant regions by the dominant AIS for systems with different τ.

There are two important properties associated with AIS: their corresponding eigenvalue and the physical braid generated by them in the flow. In the flows studied here, the AIS with very low eigenvalues are too leaky to act as stirrers, so only AIS corresponding to the dominant eigenvalues, except 1, are considered here as ghost rods. In some systems these dominant AIS move with a trivial topology so they are ineffective in generating topological chaos. In the systems that the second eigenvalue (μ_2) is close to 1 (approximately $\mu_2 > 0.9$ in this chapter's example system), often the corresponding AIS stir the flow effectively as ghost rods. On the other hand, from the view point of scalar homogenization, high-eigenvalue AIS act as obstacles impeding uniformity of scalar distribution whereas low-eigenvalue AIS smoothly mix with the rest of the domain allowing higher rates of homogenization. Fig. 4.8 (right) displays values of μ_2 for the studied range of τ.

Fig. 4.2 shows that systems with τ smaller than, but close to, 1 have a high topological entropy. More precisely, the topological entropy for $\tau > 0.92$ is higher than the TNCT estimate for $\tau = 1$ which is $h_{TN} \approx 0.962$. Since it is possible to explain the stretching for $\tau \geq 1$ using an understanding of topological chaos due to ghost stirrers, and the stretching images also suggest the same stirring effect by the periodic points, it is natural to look for ghost rods in the system with $\tau < 1$ as well. The periodic points for $\tau \geq 1$ no longer exist for $\tau < 1$. However, the shadow of their stirring effect can be seen in the stretching images (Fig. 4.7). The authors in [65] show that the topological chaos in these flows is generated as the result of the AIS playing the role of ghost stirrers. Especially in the absence of the periodic points ($\tau < 1$), these AIS are the only objects responsible for braiding the flow. The performance of AIS in mixing of systems with different τ is discussed in section 4.5. Details of their structure from the view point of geometric mechanics is studied in chapter 5.

4.3 Homogenization in terms of decay of concentration variance

In the design of a mixing device it is usually favorable to homogenize an initially segregated state at the highest possible rate. Through the (expensive) line tracking simulations, it is possible to observe the patterns of stretching for a few periods of the flow and calculate the topological entropy. However, normally in a mixing application the passive material is initially in the shape of a dense box of particles rather than an infinitesimally thin line and gets stirred for a larger number of periods. In order to visualize the actual mixing and to associate the stretching and mixing, the homogenization of a blob of passive scalar advected by the flow is simulated and the spatial variance of the concentration field, CV, is calculated as a mixing measure. Chapter 2 is dedicated to methods and parameters of computation of scalar homogenization and concentration-based measures.

This chapter uses one of the most common concentration-based measure of mixing, the intensity of segregation, which is based on the variance of concentration of a tracer material (section 2.1). It is defined as

$$\phi = \frac{CV}{CV_0}, \tag{4.11}$$

in which CV is the variance of concentration field,

$$CV = \frac{1}{A}\int (c(x,y) - \bar{c})^2 dA \approx \frac{1}{N_b}\sum_i (c_i - \bar{c})^2, \tag{4.12}$$

and $\bar{c}$ is the mean value of $\{c_i, i = 1, 2, ..., N_b\}$. Throughout this chapter $CV_0 = 1$, so $CV = \phi$ is used as the mixing measure. For a completely segregated state $CV = 1$, while for a perfectly homogenous state $CV = 0$.

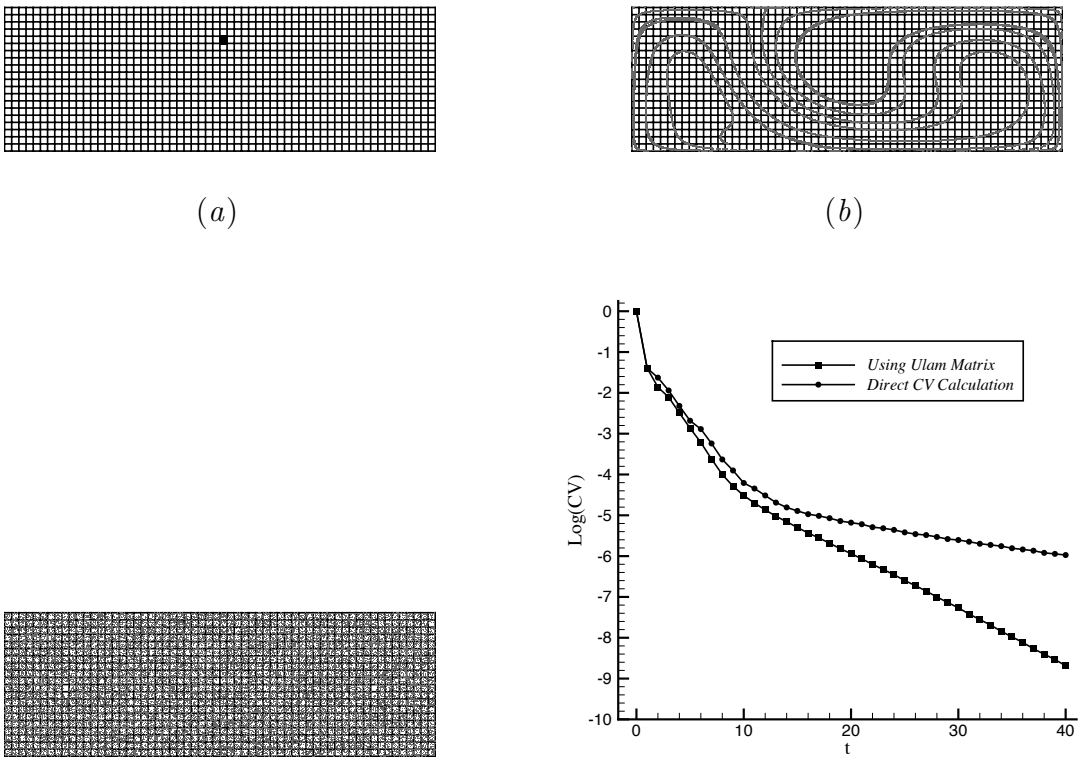

Figure 4.3: Homogenization of an initially dense 2-D box of passive scalar for (a) 0, (b) 5, and (c) 40 periods of the flow for $\tau = 1$. (d) The corresponding CV decay diagrams calculated by direct calculation and via Ulam matrix.

Initially the particles are concentrated in a few bins, causing high concentration in the location of those bins and zero concentration elsewhere. As the flow advects the particles, they get spread over the chaotic sea and the concentration becomes more uniform. Fig. 4.3 shows the coarse-graining used in this chapter for concentration calculations as well as the homogenization of a scalar and the CV diagrams using direct method (see section 2.2) and the Ulam matrix method (section 2.3) for the system with $\tau = 1$.

4.3.1 The mapping method and diffusion considerations

For the purposes of this study, the preferred method of evaluation of the coarse-grained concentration field is the Ulam matrix method (section 2.3), which is quite similar to the *mapping method* used in [61] for mixing analysis in systems like the cavity flow. After calculation of the Ulam matrix P, the concentration vector evolves as:

$$C_{n+1} = P.C_n,$$

or

$$C_n = P^n.C_0. \tag{4.13}$$

In all the computations of this chapter, square bins with side lengths of $d = a/120 = \pi/60 \approx 0.05$ are used. Using the method of section 2.4, it is possible to approximate the diffusivity corresponding to a specific bin size for systems with different τ. Table 4.1 shows the values for $d = \pi/60$. The *Péclet number*, Pe, which is the ratio of the rate of advection to the rate of diffusion, is on order of 10^4 for these flows. Pe is defined as the product of the *Reynolds number* and the *Schmidt number*; $Pe = Re.Sc = \frac{LV}{\nu}\frac{\nu}{D} = \frac{LV}{D}$.

The number of particles representing the scalar (N_{pt}) is another important parameter in the concentration calculation (Fig. 2.4). As discussed in section 2.4, for the initial segregated states, a small N_{pt} gives accurate results, but in order to observe the concentration decay in the well-homogenized states a larger N_{pt} is needed [53]. Here $N_{pt} = 360,000$ particles per bin is used, which gives enough resolution to observe the decay for 20 time units in the fastest cases ($\tau = 0.85$, see Fig 4.6). After that limit the decay stops and a constant 'tail' is seen that is an artifact of numerical computation. The actual homogenization continues at same exponential decay as before this tail. Therefore, the part of CV diagrams (Figs. 4.4 and 4.6) after this limit is not shown.

Table 4.1: Estimated diffusivity for different τ using $d = \pi/60$

τ	D
0.5	10^{-4}
1.0	5×10^{-5}
1.5	3.3×10^{-5}
2.0	2.5×10^{-5}

4.3.2 Trends of homogenization for varying τ

In this section, the method described in the previous section is used to simulate the homogenization of an initially dense scalar and compute $CV(t)$ for the range of $[0.2,\ 2.0]$. This information, along with the variations in topological entropy enable studying the correspondence between the rates of stretching and homogenization in this flow. For different τ the trend of CV decay varies as Fig. 4.4 shows in a summary. The diagrams show $Log(CV)$ as a function of time, so that a linear trend shows an exponential decay of CV. It can be seen that, while an exponential decay of CV is expected in ideal chaotic mixing systems [54], it is not always the case.

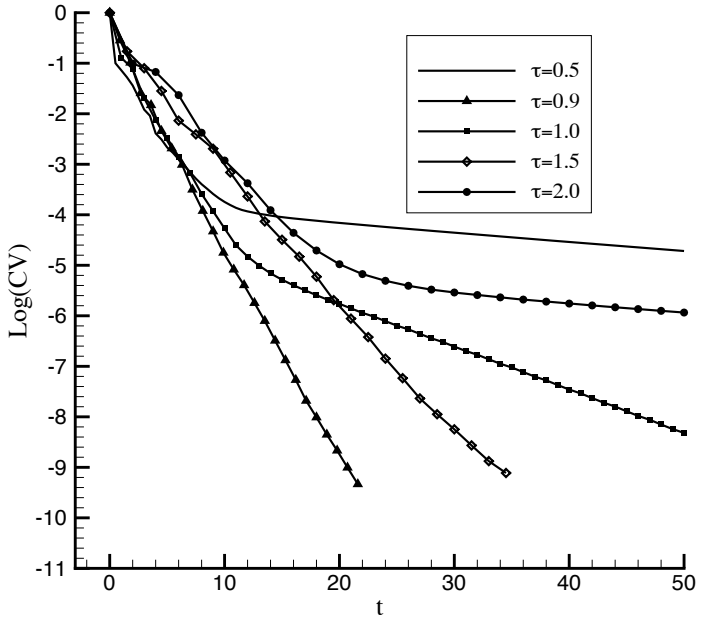

Figure 4.4: Different trends of homogenization for systems with different flow periods τ.

Four intervals of τ with different trends of homogenization can be distinguished:

For $\tau < 0.65$, elliptic islands are associated with a much bigger area in which the scalar enters very slowly (see the homogenization image for $\tau = 0.5$ in Fig. 4.7). The islands not only reduce the area of the chaotic sea, but they also cause slow dynamics around themselves so that it takes much longer for the scalar to approach them. This causes the decay in CV to be slow and almost algebraic (Fig. 4.5).

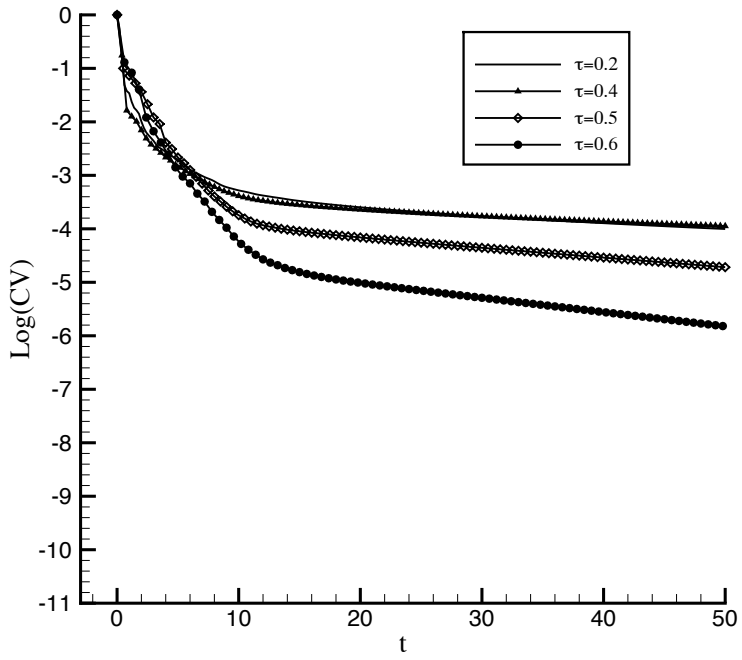

(a)

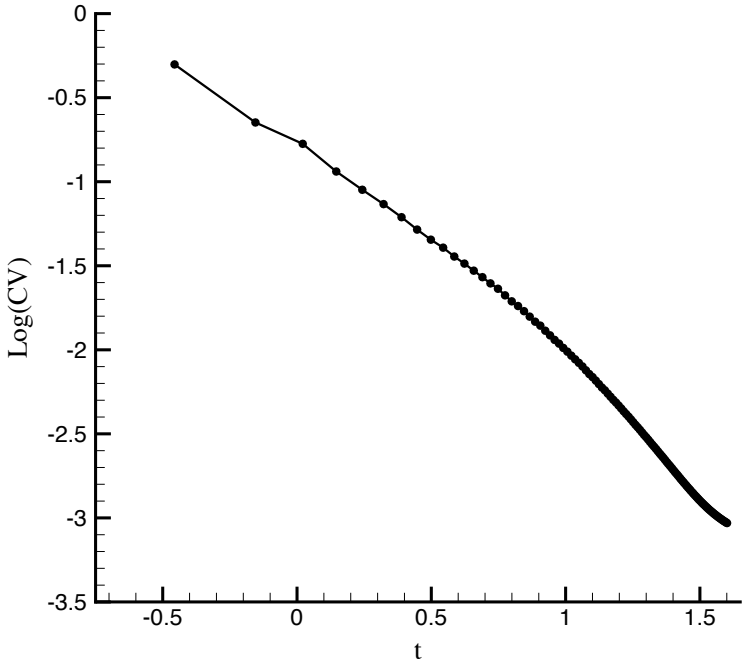

(b)

Figure 4.5: (a) CV decay diagrams. (b) Log-log diagram of CV decay for $\tau = 0.35$ as an example of a system for which the homogenization is almost algebraic.

For $0.65 < \tau < 1.0$, the scalar gets distributed all over the domain relatively quickly, and the decay is well fitted to an exponential trend (Fig. 4.6). As discussed in section 4.3.1, for these cases the number of particles used in the simulation is not enough to resolve further homogenization. Therefore, the diagrams are shown till that limit. The actual homogenization would continue to be exponential. The distribution of particles is not completely uniform, and in particular there are three regions that remain empty in the short term. However, the Poincaré sections show that these are not islands; they are 'soft' obstacles that get mixed with the rest of the domain quickly enough to allow an exponential decay of CV. In fact these regions act as stirrers as we will discuss more in the next section.

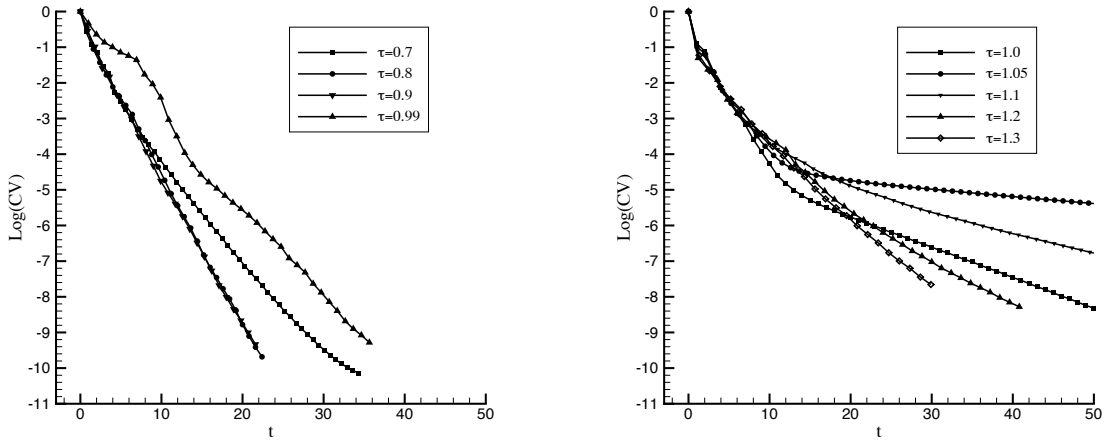

(a)

(b)

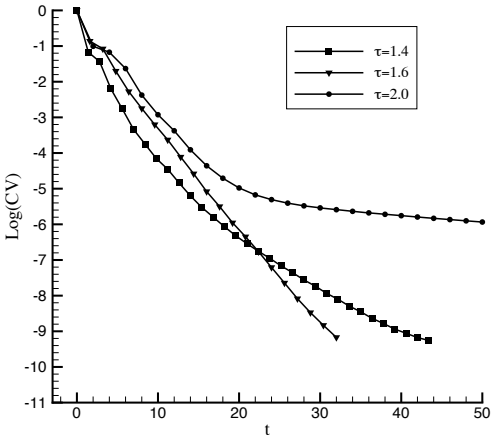

(c)

Figure 4.6: CV decay diagrams for $0.70 < \tau < 2.0$.

A significant change happens from $\tau = 0.99$ to $\tau = 1$. The CV decay for $\tau = 0.99$ is close to exponential and except some fluctuations, its overall trend is steady. On the other hand, the CV diagram for $\tau = 1$ shows an exponential decay for about 10 time units and, after a bend at this point, a slower exponential decay starts with a second, smaller exponent. The difference between $\tau = 0.99$ and $\tau = 1$, is that there are three tiny unmixed regions in the case of $\tau = 1$ that are permanent obstacles in the way of mixing and the dynamics around them is slow. This slow dynamics is

related to the period-3 parabolic point. For $\tau > 1$ the island breaks into two islands and the dynamics around the islands is slow. As τ increases, these islands diverge more. This causes the slow-dynamic region to grow and the rate of CV decay to drop so that a minimum happens around $\tau = 1.05$. For larger τ the distance between the islands has grown enough to allow homogenization in between them and the CV decay rate again grows. The trends of CV decay are similar for all $1 < \tau < 1.15$.

Another course of purely exponential decay resumes when τ exceeds 1.2 with variations in its rate until another bifurcation at $\tau = 2$ where a bent curve similar to that of $\tau = 1$ appears. Again, the highest rates of exponential decay in the interval $\tau\epsilon[1,\ 2]$ interval correspond to systems with no islands in their Poincaré sections, such as $\tau = 1.4$.

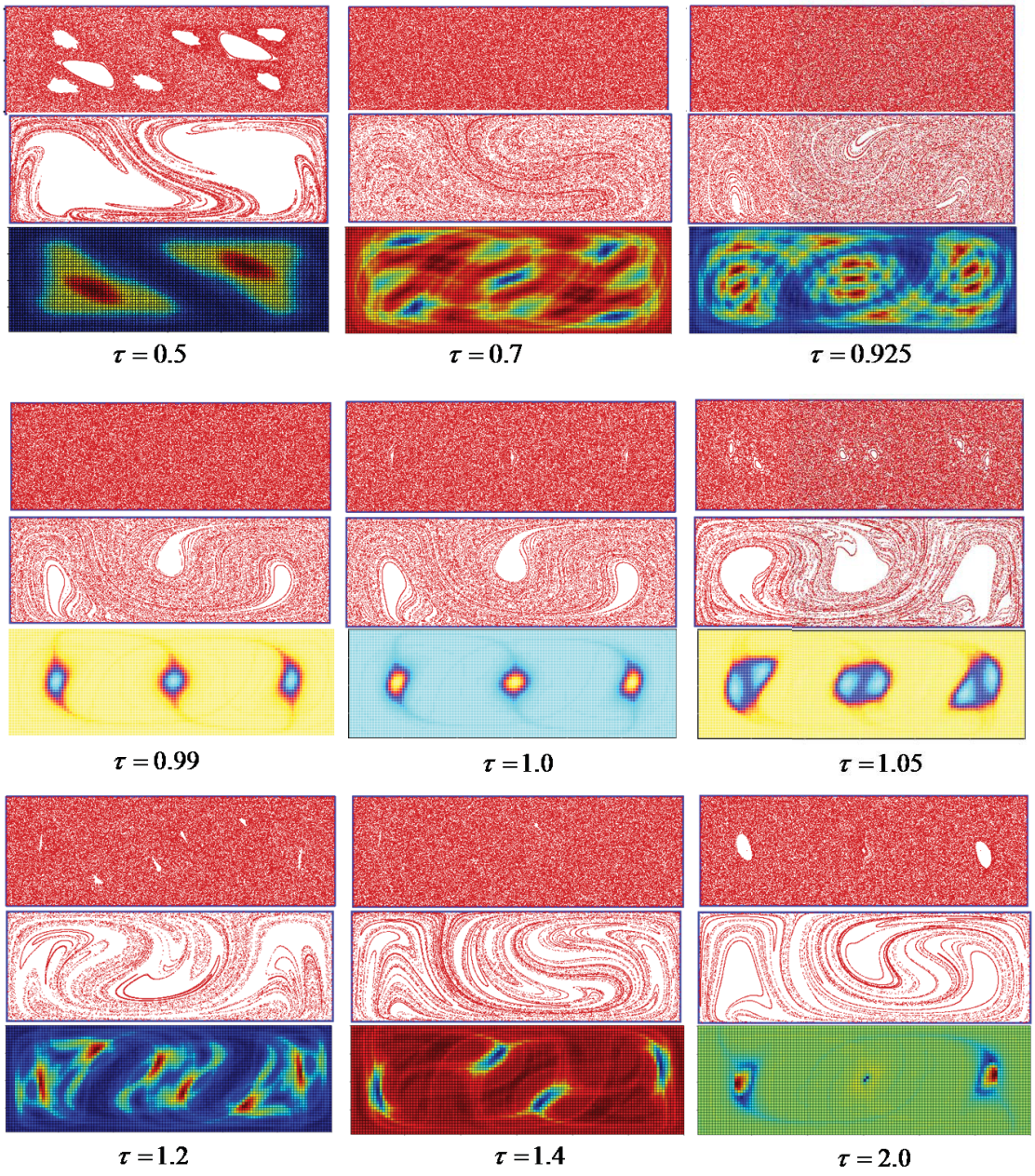

Figure 4.7: Poincaré sections (the first row for each τ), homogenization after 10 time units (the second row for each τ), and AIS structure (the third row for each τ) for example flows of different intervals of τ.

All systems with a fully chaotic Poincaré section show exponential CV decay, but the rates of decay vary. There are regions of slower and faster dynamics in the chaotic sea that cause the filaments of lower or higher concentration of scalar in the homogenization (see homogenization images of Fig. 4.7 for $\tau = 0.7$, $\tau = 0.9$ and

$\tau = 0.99$). On the other hand, in some systems with small islands (e.g. $1 < \tau < 1.15$) the decay is slower than exponential, even if the concentration is calculated over a fully chaotic window. This means that the islands can slow down the dynamics in the chaotic sea. This behavior is similar to the impeding effect of no-slip walls studied in [30]. These observations will be explained more using the set-oriented approach in section 4.5 and lobe dynamics in chapter 5.

4.4 Relationship between homogenization and stretching

Fig. 4.8 (a) enables a comparison between homogenization and stretching for the studied range of τ. The circular markers in this figure show the long-term behavior of concentration decay by displaying values of $Log(\frac{1}{CV(t=50)})$ which is called the Long-term Homogenization measure based on the elapsed time (LH from now on). A more homogeneous state corresponds to a smaller CV value, or larger $1/CV$ values. Therefore systems with larger values of LH cause more homogenization in 50 time units of the flow. The logarithm is used to avoid very small numbers. For other applications it is possible to define short-term measures and measures based on the elapsed number of periods as well. The square-shaped markers display topological entropy based on the elapsed time, h_t, as a function of τ (see section 4.2). Using this data we can examine the correlation between h_t and the rate of CV decay and determine to what extent the high/low stretching rates can be a sign of fast/slow homogenization in chaotic mixing systems.

For τ smaller than 0.65, as shown in Fig. 4.5, the homogenization is almost algebraic, mostly because of the large slow-dynamic area around the islands. Stretching is also considerably poor for τ smaller than 0.5, so the systems are weak in terms of chaotic stretching and the area of the chaotic domain, and this effect appears in both h_t and LH. For $0.5 < \tau < 0.65$, the stretching rate is growing but the islands are

still sizable, so the stretching is concentrated only in some parts of the domain (see $\tau = 0.5$ in Fig. 4.7). In other words, h_t is high but the stretched filaments are not well distributed, so that LH is still low.

For $0.65 < \tau < 1$, as the corresponding Poincaré sections also confirm, the dynamics in the whole domain is chaotic. The chaos causes the values of both h_t and LH to be relatively high. However, there are fluctuations: h_t is at its highest values for $0.65 < \tau < 0.85$, while LH is maximum for the range of $0.75 < \tau < 0.98$. If one looks for the optimal range of mixing as the parameter τ is varied, the answer would be the latter. However, chaos diagnostics using h_t would lead to the former range. There is obviously some overlap and correlation but it should be said that, for the sake of optimization, it is only possible to find the 'vicinity' of the optimal mixing by means of the topological entropy data alone. More investigation is required within this 'vicinity' to find the optimal system.

For $\tau > 1$ where the small islands start to appear in the Poincaré sections, the chaotic sea is not uniform anymore. The size of islands is small and has negligible influence on the CV calculation, but the dynamics around them is also slow so that it takes a long time for the scalar to reach the vicinity of the islands. Slow homogenization due to this slow dynamics continues until the minimum of LH is reached around $\tau = 1.05$. The slow dynamics causes h_t to decrease as well so that, in a complete agreement with LH, it also reaches its minimum around 1.05 and then starts to grow after this point. For $\tau > 1.05$, both measures increase with similar trends while the slow-dynamics regions between the tiny islands start to disappear, and both the Poincaré section and the scalar homogenization start to become uniform.

In summary, the variations in the h_t and LH diagrams show correspondence to a large extent for the following regions: $\tau < 0.5$, $0.75 < \tau < 0.85$ and $0.98 < \tau < 1.3$. Despite the local fluctuations in the values of both h_t and LH, for the same amount of time systems with bigger τ complete fewer periods of stirring. Therefore, the overall trend of both h_t and LH is descending with increase in τ, and their maxima in the

[1, 2] range of τ are smaller than their maxima in [0.2, 1] range. So it can be said that the global maxima for each of the measures happens in the [0.7, 0.95] range.

4.5 The set-oriented approach

Almost Invariant Sets (AIS), as explained in section 4.2.2, have been studied as ghost rods that stir the double-lid-driven cavity flow [65]. Here the same set-oriented approach is employed to study the mixing caused by these ghost rods and to find explanations for the mixing behaviors observed in sections 4.3 and 4.4. Fig. 4.8 (right) displays values of the second eigenvalue of the Markov matrix, μ_2, along with the LH measure of homogenization for the studied range of τ. The eigenvalue μ_2 is a representative of the invariance of the AIS so that higher μ_2 shows more invariance while lower μ_2 shows more leakiness of the corresponding AIS. For example for an island, $\mu_2 = 1$.

In systems with $\tau < 0.65$, a relatively large portion of the domain experiences slow dynamics, which corresponds to a high-eigenvalue AIS (see $\tau = 0.5$ in Fig. 4.7). The core of this region consists of smaller elliptic islands, with each island being surrounded by a bigger slow-dynamic area that keeps the tracer material in a smaller fraction of the chaotic sea, causing slow homogenization. In other words, there is a larger area around an island that is a part of the chaotic sea but that gets mixed much slower than areas of chaotic sea far from the islands. This area is almost invariant with $\mu_2 \approx 0.999$ so it is almost excluded from the mixing part of the domain. Fig. 4.5 illustrates that for $\tau = 0.35$ (as an example), the homogenization is almost algebraic, which is much slower than the anticipated exponential trend for ideal chaotic systems.

For systems in the interval $0.65 < \tau < 1$, the tracer material gets distributed in the entire domain relatively quickly and the decay is well fitted by an exponential trend (Fig. 4.6). As explained in [65], the AIS are playing the role of "ghost rods". Comparing the homogenization and AIS images of Fig. 4.7 (especially for $\tau = 0.7$

and 0.925) confirms that the scalar is stirred by these AIS. However these AIS are not too invariant ($\mu_2 < 0.98$) to slow down the mixing like solid obstacles, and soon they too become homogenized. These 'soft' rods are optimal stirrers; they stir the flow effectively while not being 'hard' obstacles in the way of mixing.

There is a sudden decrease in the rate of homogenization when τ approaches the bifurcation point at 1. At this point the nature of the ghost rods changes from *almost* invariant regions to periodic points that are *invariant* [65]. At $\tau = 1$ a period-3 parabolic point stirs the flow (Fig. 4.1). When τ exceeds 1, each of the parabolic points bifurcates to a set of two hyperbolic and two elliptic points (Fig. 4.9). There are two small islands associated with the elliptic points inside each set and the whole set travels together and stirs the flow like a single ghost rod. These sets, which are associated with a high eigenvalue AIS ($\mu_2 > 0.99$), act more as 'hard' rods or slow-dynamic areas toward which the material approaches very slowly. Therefore, the homogenization rate becomes significantly smaller than that for $\tau < 1$. Increasing τ causes a growth in the distance between the four points so that a larger high-eigenvalue, almost invariant region appears inside the flow and causes the rate of CV decay to decrease more. For $\tau > 1.05$ the four-point-sets mainly split into two couples, each consisting of an elliptic point and a hyperbolic point, and the distance between the couples starts to become large enough to allow homogenization between them (e.g. $\tau = 1.2$ in Fig. 4.5). The eigenvalue μ_2 starts to decrease and the 'soft' stirrers improve the homogenization rate. This break-up of the periodic points continues until τ exceeds 1.2, at which point the almost invariant sets start to break, and another course of exponential homogenization resumes as a result. Similar to the range $\tau\epsilon[0,\ 1]$, the highest rates of exponential homogenization in $\tau\epsilon[1,\ 2]$ range correspond to systems with no visible islands or 'hard' rods e.g. $\tau = 1.4$.

Fig. 4.8 (right) shows a high correspondence between the leakiness of the AIS and the long-term homogenization measure, LH. Almost with no exception for the range $\tau\epsilon[0.2,\ 1.4]$, lower eigenvalue, or equivalently higher leakiness of the AIS, is accompa-

nied by higher rate of homogenization. This observation, added to our discussion for different intervals of τ, shows that the set-oriented approach is an accurate method for the study and design of these mixing systems. For these flows, the highest rates of stretching and homogenization are obtained here when there are no solid rods, islands or periodic points (invariant objects) acting as stirrers, and the leaky AIS are playing the role of stirrers. These stirrers, unlike the other mentioned (ghost) stirrers, are invisible in the Poincaré section, meaning that they mix the flow without producing a slow-mixing area around themselves.

4.6 Conclusions

Stretching is mainly related to the stirrers' topology of motion, while homogenization is affected by the specific geometry of motion as well. Noting that it is important to look at the stretching based on the elapsed time units instead of periods, a remarkable correspondence between the decay of concentration variance and the time-rate of stretching is observed. Regions of low/high h_t are roughly correlated with regions of low/high LH. By using the powerful Thurston-Nielsen classification theorem, the amount of stretching can be well predicted by the topology of motion of the stirrers [9], and this stretching can be considered as a useful indicator of the quality of mixing. Evaluating the lower bound of stretching can be used as a start for analyzing and designing chaotic-mixing systems. Once the parameters of the system are determined for a region of high stretching, the detailed optimization will require other more expensive tools, mainly through accurate simulation of the fluid flow. Even though the regions of favorable CV decay are not exact matches of regions of high h_t, from the design point of view it is advantageous to know the approximate range of optimal mixing.

The set-oriented approach proves to be an accurate method for predicting the mixing behavior of the chaotic systems. The previous study by Stremler *et al.* [65]

shows that the AIS are responsible for generating topological chaos in the double-lid-driven cavity flow, especially when there are no periodic points performing as ghost rods. The highest rates of mixing (by far) are obtained when the stirrers are the leaky low-eigenvalue AIS instead of periodic points that are invariant sets. The rate of mixing closely follows the corresponding eigenvalue. Considering the fact that in the computation of the almost invariant sets, it is only necessary to track less than 1% of the number of particles needed for homogenization simulations, it is a considerably less expensive tool for study of mixing systems.

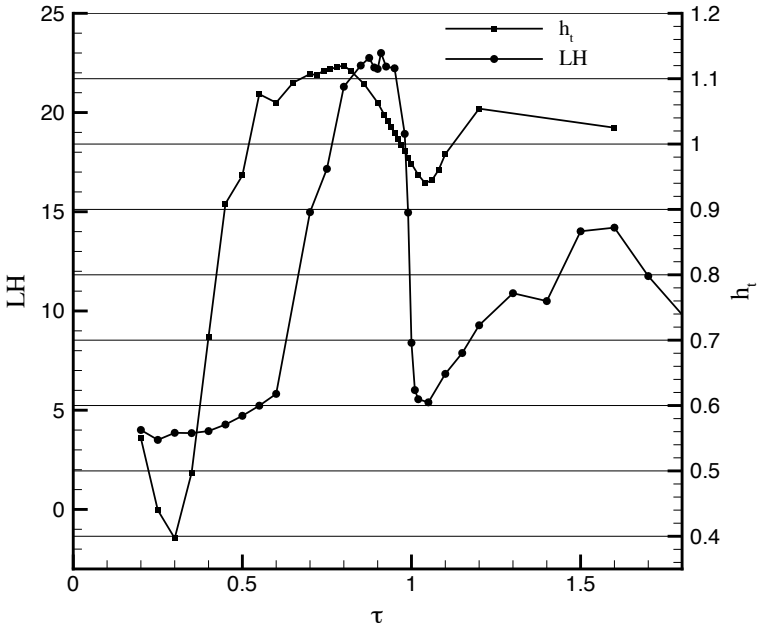

(*a*)

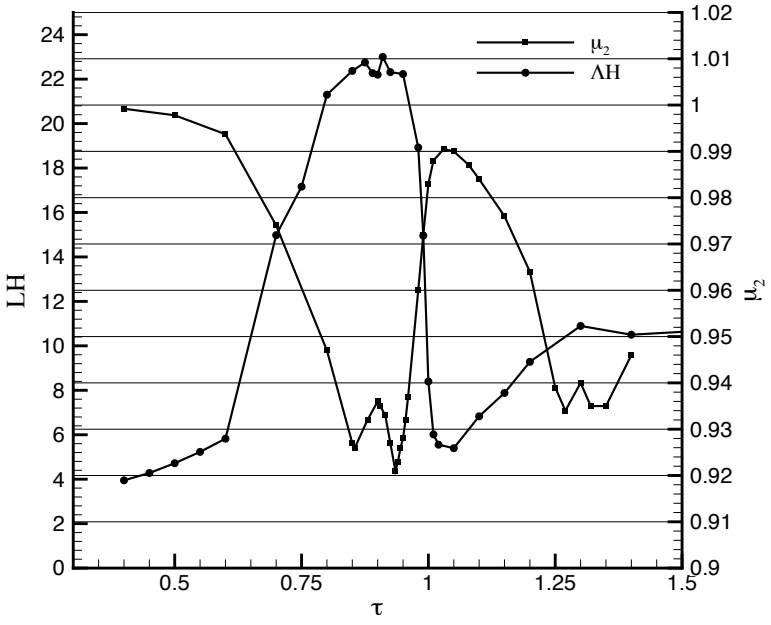

(*b*)

Figure 4.8: (*a*) Relationship between long-term homogenization in terms of LH and topological entropy h_t for variations in τ. (*b*) LH and μ_2, the second eigenvalue of the Markov matrix, as a function of τ.

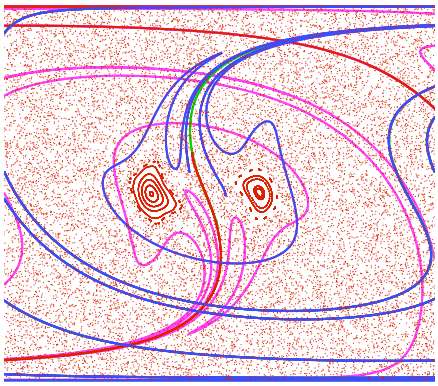

Figure 4.9: Invariant manifolds of the central set of hyperbolic points for $\tau = 1.05$ on top of the Poincaré section. Segments of the manifolds form the boundaries of the ghost rod; two elliptic islands are seen with an elliptic point inside each.

5

Transport and mixing via lobe dynamics

In the previous chapter, the topological chaos and mixing are studied in the lid-driven cavity flow based on the stretching of material lines, the homogenization of a scalar and the action of almost invariant sets playing the role of ghost stirrers as well as obstacles in the way of mixing. Mixing in a dynamical system is closely connected to the concept of transport [51, 80]. In the view of lobe dynamics [59, 77, 7, 78] the phase space consists of different regions and in order for mixing to happen the passive particles should be 'transported' between the regions. Studying the structure of these regions, their boundaries and the mechanism of transport through these boundaries helps to understand the details of different phenomena that are observed and measured in the previous chapter.

As it is illustrated in section 4.2, in systems with $\tau \geq 1$, the periodic points of the Poincaré map play the role of ghost rods in stirring the flow. Section 4.5 showed that some ghost rods can also act like obstacles and imped the mixing. From the point of view of lobe dynamics, periodic orbits play another important role in transport: segments of their stable and unstable manifolds define boundaries of different regions in the phase space. The particles can cross these boundaries and transfer from a region to the neighboring region only under special circumstances and via special gateways (lobes) [77, 7]. In this chapter this fact is used to explain the homogenization around

the ghost rods and their important effect on the mixing behavior of systems with different τ.

Lobe dynamics has been used to explain the transport and mixing in different dynamical systems. Some examples are: Stokes flow of the eccentric journal bearing [38], flows with aperiodic time-dependency like Rossby wave flow [44], the inviscid flow of an oscillating vortex pair [58], oceanographic, coastal and atmospheric flows (see for example [55, 16, 36, 79]). Transport via lobes is not confined to mixing problems. For example in dynamical astronomy, transport between different regions of phase space can be studied quite similarly [19].

The transport between regions of phase space is studied by Wiggins in [77]. Following him, let p_i and p_j denote two hyperbolic periodic points of the flow and $W^s(p_i)$ and $W^u(p_j)$ denote the stable manifold of p_i and the unstable manifold of p_j respectively. Fig. 5.1 is the generic figure when $i \neq j$. A point $q \epsilon W^s(p_i) \bigcap W^u(p_j)$ is called a *primary intersection point (pip)* if it is the only intersection between $S(p_i, q)$ and $U(p_j, q)$; where $S(p_i, q)$ is the segment of $W^s(p_i)$ between p_i and q, and $U(p_j, q)$ is the segment of $W^u(p_j)$ between p_j and q. All intersection points in Fig. 5.1 comply with this definition so all of them can be deemed as pips. However one of them is chosen as *the pip*, q_0. $S(p_i, q_0) \bigcup U(p_j, q_0)$ defines the boundary of two regions R_1 and R_2. The motion of points across this boundary is the topic of discussion here. As it is proved in [77], under one iteration of the flow the only points that can transfer from R_1 to R_2 are those inside the *lobe* $L_{1,2}(1)$ shown in Fig. 5.1. Similarly, the only points that can transfer from region R_2 to R_1 under one iteration of the flow are those inside the *lobe* $L_{2,1}(1)$. The Stokes flow of Eq. 4.7 is area-preserving so the lobe area is always mapped to another lobe of the same area. Therefore the transport of material per iteration of the flow between the regions R_1 and R_2 can be simply equated to the lobe area.

In order for homogenization to happen, the particles need to get caught in one of the lobes so that they can be transported to other parts of the domain. In the

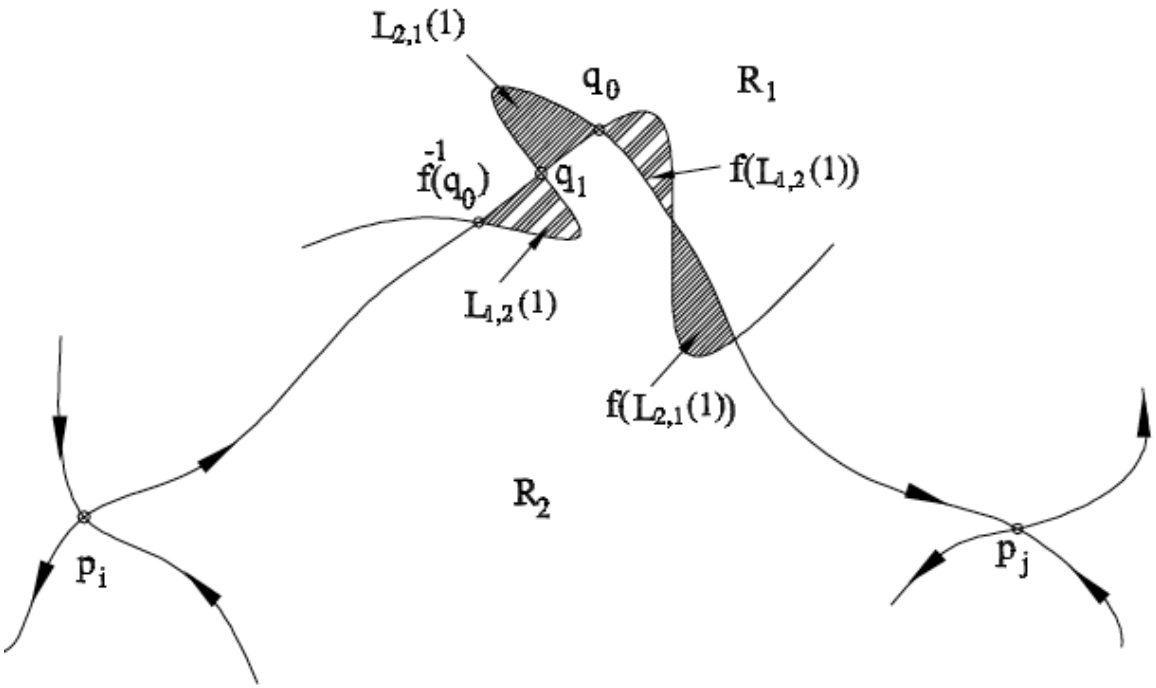

Figure 5.1: Schematic figure of invariant manifolds of two periodic points p_i and p_j, the pip and the lobes.

next section, this mechanism of transport is explained for the cavity flow. Analysis of section 4.3.2 showed that the rate of homogenization for systems with different τ shows a great deal of variations. For some ranges of τ the rate is slower than the ideal exponential rate while an exponential rate is anticipated especially in the absence of no-slip walls [30]. More details on the no-slip wall effect and the similar effect of lobes are discussed in section 5.3. For some ranges of τ the rate of homogenization is close to algebraic and in a few cases it consists of two different intervals with different exponential rates of CV decay. In chapter 4, these variations are explained based on the amount of topological chaos and the role of almost invariant sets. However the dynamical reasons causing these phenomena were not explained. Lobe dynamics describes the fluctuations in the rate of mixing from a highly exponential rate to a slower, two-rate trend, then to a minimum and after that to an exponential trend, from the view point of geometric mechanics.

5.1 Describing ghost rods and homogenization through lobe dynamics

This section explains the sub-exponential two-rate decay homogenization around the minimum at $\tau = 1.05$ via lobe dynamics. At $\tau = 1.05$ the pairs of periodic points born at $\tau = 1$ have become separated enough to appropriately illustrate the structure of the lobes and details of the ghost rod. Also this is after this point that the mixing rate starts to grow until it reaches the pure exponential trend at $\tau = 1.3$. In section 4.5 AIS showed their important role in mixing, both as ghost stirrers and as leaky or invariant obstacles in the way of mixing. Here a closer look is taken at the details of the structure of these ghost rods. Fig. 5.2 (left) shows the step by step homogenization of a scalar initially outside of the ghost rod region. Before $n = 10$ periods, the scalar gets distributed mainly in the region outside the ghost rods. Between the $n = 10$ and $n = 15$ it gains a fairly homogenous state outside the ghost rods while it reaches

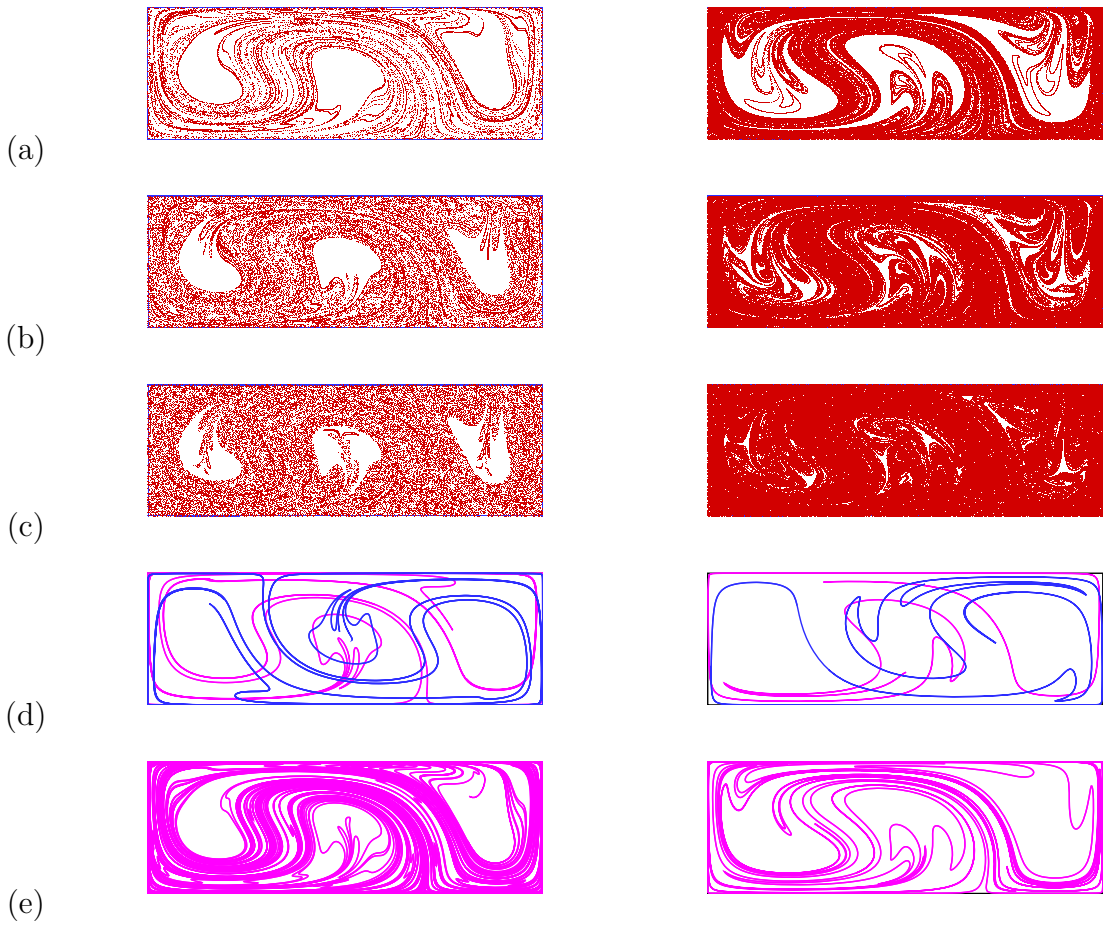

Figure 5.2: Rows (a) to (c) show homogenization of a scalar in the flow with $\tau = 1.05$ (left) and $\tau = 1.15$ (right) for 10, 15 and 20 periods of flow, respectively. Row (d) shows unstable manifold of p_1 (in pink) and stable manifold of p_2 (in blue) which form the boundaries of the ghost rod as well as the lobes as gateways into the ghost rod. Row (e) shows the unstable manifold of p_1 for more periods of the flow. Comparison to the homogenization images (a) through (c) shows that the unstable manifolds act as boundaries for the scalar transport.

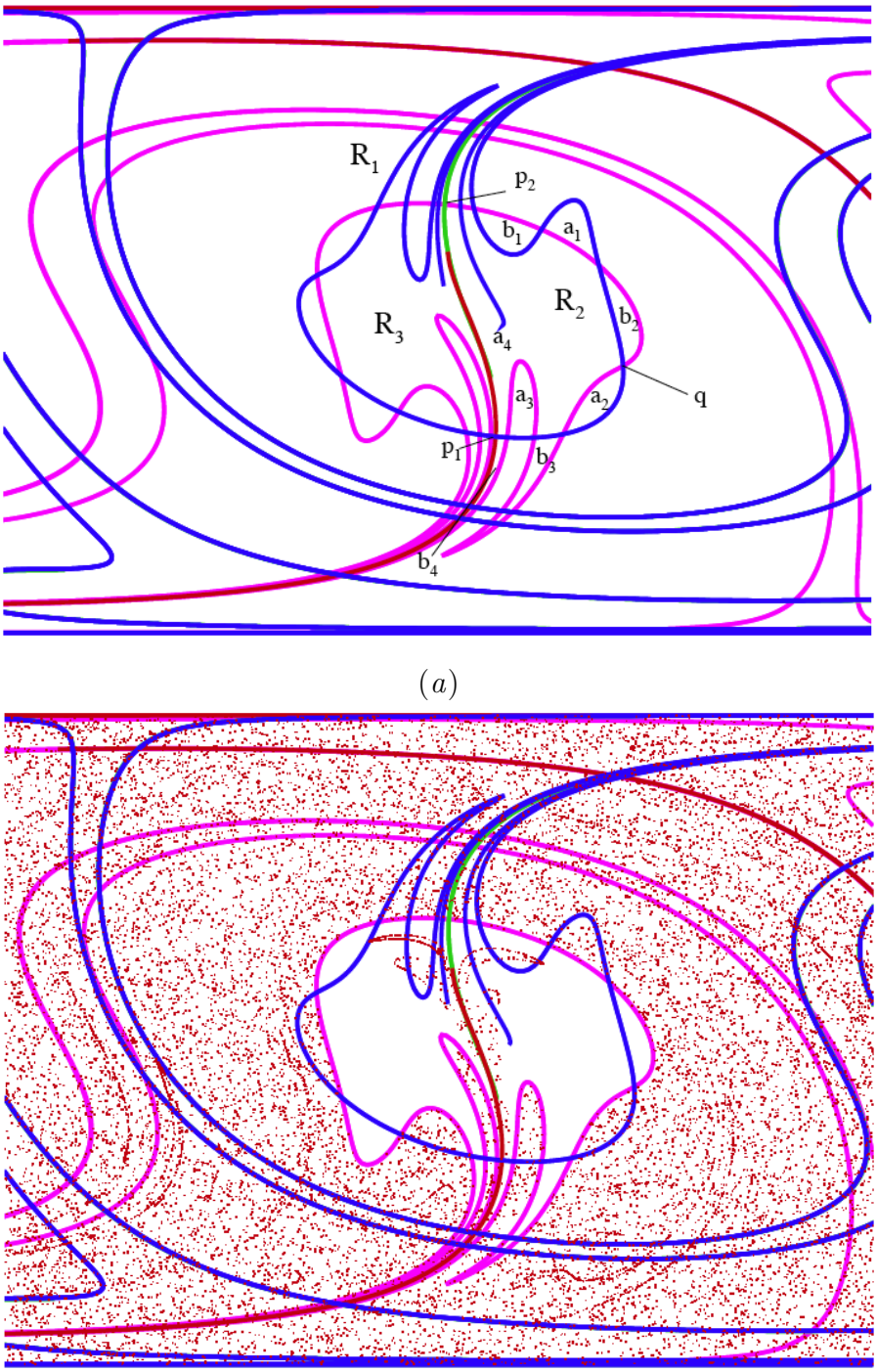

(a)

(b)

Figure 5.3: (a) invariant manifolds of p_1 and p_2 in a closer look. The stable manifold of p_2 (green) and unstable manifold of p_1 (red) form the border between R_2 and R_3 while the stable manifold of p_1 (blue) and unstable manifold of p_2 (pink) form the border between R_1 and either of R_2 or R_3. The transport between different regions of the phase space happens through the lobes (e.g. a_1, b_1, etc.) as the text explains. (b) A scalar initially in R_1 homogenized for 20 periods of the flow (less than 7 periods of the map $\mathbf{f}$). The unstable manifold of p_2 forms a boundary across which the scalar does not pass.

the boundaries of the ghost rods. After this stage, the scalar can slowly find its way inside the ghost rods. It is important to note that there is a 'communication' between the ghost-rod area and the rest of the domain meaning that the scalar not only fills the ghost rods slowly but it also leaves them at the same pace causing an overall homogenization at a slower pace than before. This is clearly in agreement with the bent in the CV decay diagram (Fig. 5.5, $\tau = 1.05$) that is followed by decay at a slower rate.

Each ghost rod includes a set of two hyperbolic and two elliptic periodic points. A comparison between images (c) and (e) in Fig. 5.2 illustrates that the scalar is actually following the unstable manifolds of the hyperbolic points and enters the ghost-rod region lobe by lobe following these manifolds. In a closer look, Fig. 5.3 shows the invariant manifolds of the central set of two hyperbolic points for $\tau = 1.05$. The following observations connect lobe dynamics to the AIS and homogenization in system with $\tau = 1.05$ (Note that the manifolds and lobes are based on a period-three hyperbolic point so the map $\mathbf{f}$ (as defined in Fig. 5.1) is the Poincaré map of the flow defined at any point $\mathbf{x_0}$ by: $\mathbf{f}(\mathbf{x_0}) = \mathbf{x}(\mathbf{x_0}, 3\tau)$, $\mathbf{x}$ being the fluid flow defined by Eqs. 4.7. Therefore, one iteration of the map is equivalent to three periods of the flow.):

1. Following the generic illustration of lobes in Fig. 5.1 and comparing to the AIS image of Fig. 4.7, *the pip* is point q, defining the border between R_1 and R_2 to be the segment of the unstable manifold of p_2 (the pink line) from p_2 to q plus the segment of the stable manifold of p_1 from q to p_1. Similar argument for the left part of the manifolds defines the boundary between R_1 and R_3. Comparison between the AIS image of Fig. 4.7 and this image shows that $R_2 + R_3$ is the same as the central AIS or the *ghost rod* as defined in chapter 4 using the set-oriented approach and R_1 is the larger AIS consisting the fluid domain excluding the ghost rods.

2. A scalar, homogenized in R_1 cannot cross the unstable manifold of p_2 so that the manifold (pink line) acts as the only important borderline for the scalar. Thus in order to enter the AIS, the scalar has to travel through the channels determined

by the manifold. Fig. 5.3 (right) shows that the scalar is eventually finding its way inside the ghost rod. The manifold continues to be the border of scalar all the time, however the rest of the manifold is not shown to keep the figure tidy.

3. Different simulations are accomplished to see the scalar transport by initiating a dense box of particles inside different lobes and tracking their positions:

Lobe a_1 is mapped to lobe a_2 in one iteration of the map $\mathbf{f}$, meaning that all the scalar in lobe a_1 ends up in lobe a_2. Over the next iteration it is mapped to a_3, then a_4 ... and the scalar slowly finds its way inside the ghost rod and fills the area lobe by lobe. In later iterations, the lobes get thinner and fill all the area inside the ghost rod except the tiny elliptic islands shown in Fig. 5.7. Lobe b_1 is mapped to b_2, then b_3 then b_4 which is a very thin and long lobe and acts like a gateway for the scalar to escape from the ghost rod. These extremely thin and long lobes exist all over the region R_1 and are the channels in which the materials travel and the transport happens. This can be said that lobes a_i are the gateways into the ghost rod and lobes b_i are the gateway for the scalar to leave the ghost rod.

The rate of transport between each pair of regions R_i and R_j is always one lobe per period of the map. Therefore this is the shape of the lobe that plays the main role in determining the rate of transport and mixing. When the scalar is initially located in region R_1 far from the AIS, it gets well distributed in the entire R_1 region through the extremely long and thin lobes in less than 4 iteration of the map. (Note that this flow ($\tau = 1.05$) is the slowest system in $0.7 < \tau < 2$ range.) Then it gets close to the boundaries of the ghost rod. The scalar then needs a very longer time to fill inside the ghost rod. This is how CV decay slows down after about 11 periods of the flow and the decay continues with a second slower rate. Again we emphasize that the scalar not only has to enter the ghost rods (which happens at a slower rate than homogenization in R_1) but it also has to 'communicate' with them i.e. it enters and leaves the ghost rods continuously causing a global slower decay. As a result, CV decay is slower even when it is calculated over a window contained in R_1.

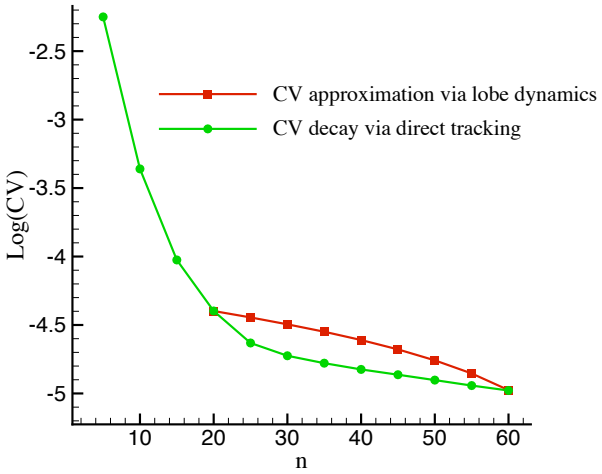

Figure 5.4: Estimation of CV decay for $\tau = 1.05$ using transport via lobes.

These observations can be confirmed by estimating the rate of CV decay via transport through lobes based on the above assumptions. The homogenization images (Fig. 5.2) show that after 20 periods of the flow, the domain is composed of two main parts that are shown in the image with red (the scalar homogenized outside the ghost rods) and white (the empty regions inside the ghost rods). We denote the areas corresponding to these parts by A_{out} and A_{in} respectively. All the scalar is distributed fairly homogenously in A_{out} part after this time so that $c_{out} \approx \bar{c}\frac{A_{out}}{A_{in}+A_{out}}$, while A_{in} is essentially empty of the scalar so that $c_{in} \approx 0$. Therefore CV for $n \geq 20$ can be estimated as:

$$CV = \frac{1}{N_b}\sum_{in}(c_{in} - \bar{c})^2 + \sum_{out}(c_{out} - \bar{c})^2 = \frac{A_{in}}{(N_b - 1)A_{out}} \tag{5.1}$$

in which N_b is the number of bins for CV calculation. The rate of change of CV is:

$$\frac{dCV}{dn} = \frac{A}{(N_b - 1)A_{out}^2}\frac{dA_{in}}{dn} \tag{5.2}$$

in which $-\frac{dA_{in}}{dn}$ is the rate of transport of the scalar into A_{in} and is equal to the area of one lobe (Note that there are three A_{in}'s, but the total transport takes place in

one period of the map which is equal to three period of the flow. Thus the transport per period of the flow is one lobe area.). For $\tau = 1.05$ the area of one lobe evaluated using Green's theorem is about 0.02 which is %0.15 of the whole domain. Area of the three ghost rods, combined, is %15.0 of the domain. Fig. 5.4 compares the diagrams of CV decay and $-\frac{dCV}{dn}$ obtained from lobe dynamics estimation with the diagrams obtained from the direct method of CV calculation. The estimated rates using lobe dynamics is close to the direct simulation. Around $n = 20$ the scalar in A_{out} is not well-homogenized so the assumption of a homogenous state is inaccurate but for larger n the accuracy increases.

4. Segments of the stable manifold of p_2 (green line) and unstable manifold of p_1 (red line) also generate lobes through which the transport between R_2 and R_3 takes place. However, these lobes are much smaller and not visible in Fig. 5.3.

In summary it can be said that the material in both AIS 'leak' inside the other AIS via the lobes that are defined by segments of the invariant manifolds of the hyperbolic periodic points. The lobes make it possible to accurately predict where the material will go in any number of iterations. Calculation of the lobe areas can give the transport rate between the two AIS and this can be used to explain the rate of homogenization. The bent in CV decay diagram takes place about $n = 11$ periods. This is the time that takes for the material to reach the vicinity of the periodic points through the lobes. The overall decay of concentration variance remains exponential when the penetration inside the ghost rods starts but the exponent is smaller.

The transport always happens through the manifolds but the difference between the vicinity of periodic points and the rest of the domain is in the shape of the lobes. Far from periodic points the lobes are extremely thin and long so that in one period of flow, the scalar gets spread in a broad area while in the vicinity of the periodic points the lobes are thick and short and the material only travel from one lobe to another lobe of similar size. Because of the 'communication' between inside the ghost

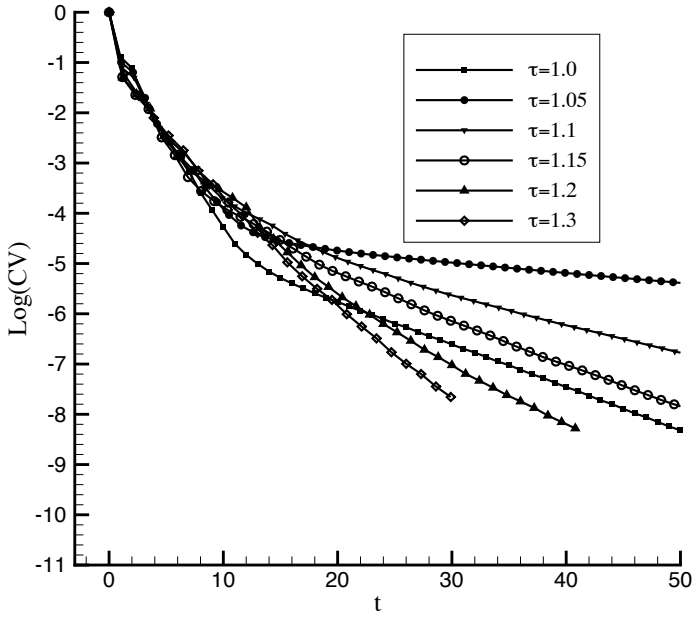

Figure 5.5: Variations in CV decay for τ between 1 and 1.3.

Table 5.1: Estimated area of one lobe for different τ stated as percentage of the whole domain area. A_{12} is the area of one lobe between R_1 and R_2 and A_{23} is the area of one lobe between R_2 and R_3.

τ	A_{12}	A_{23}
1.05	%0.15	%0.0
1.15	%1.4	%0.46
1.30	%5.0	%1.0

rods and the rest of the domain, concentration variance decays slower when the scalar reaches this vicinity.

5.2 Variations in ghost rods and trends of homogenization

As discussed in the previous chapter and the CV diagrams of Fig. 5.5 illustrate for τ in [1 1.3] range as well, the homogenization trend varies even though the periodic points exist for all systems with $\tau > 1$. The ghost-rod structure of system with

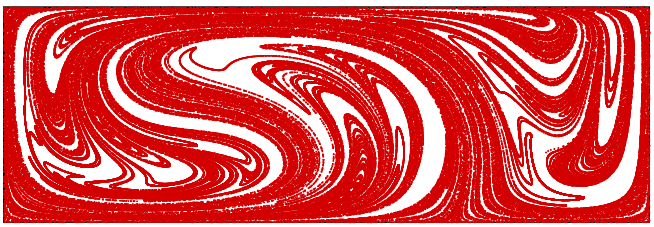

(a)

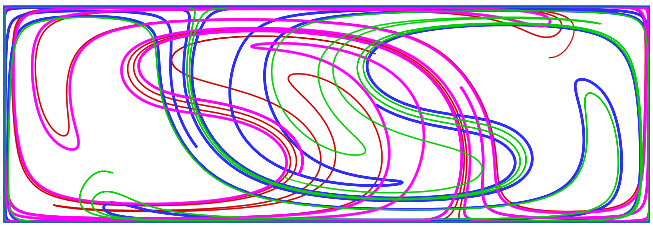

(b)

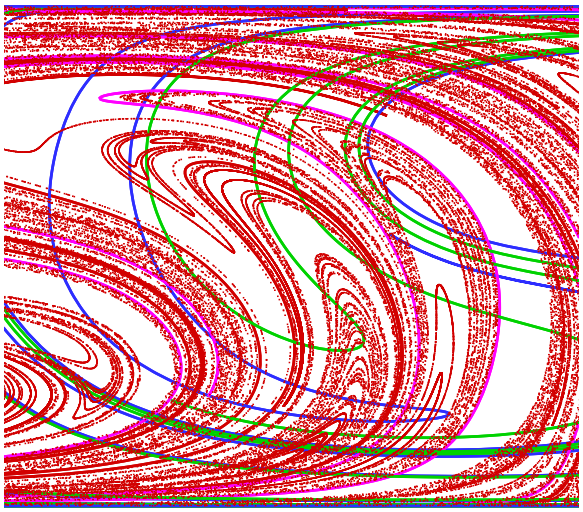

(c)

Figure 5.6: $\tau = 1.3$; (a) scalar homogenization for 8 periods of the flow; (b) the invariant manifolds of the central pair of hyperbolic points; (c) a closer look at the homogenization and manifolds around the central ghost rod(s).

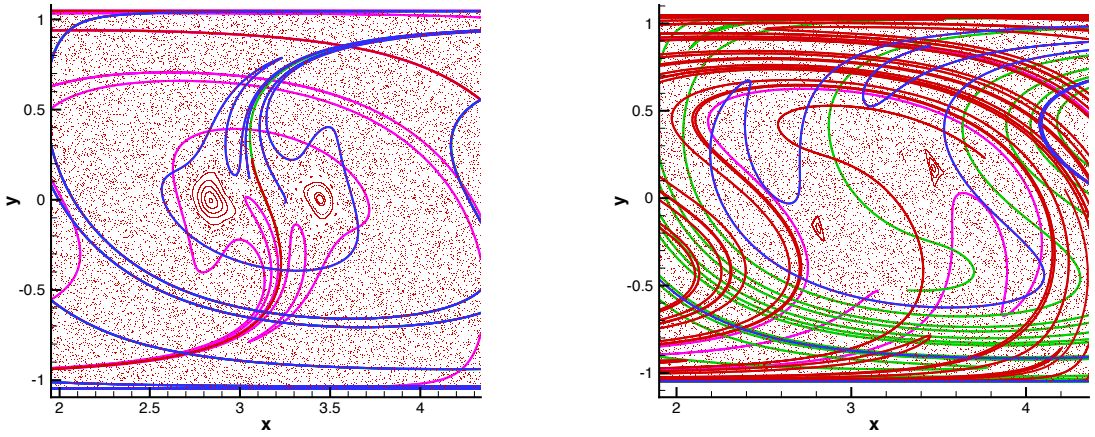

(a) (b)

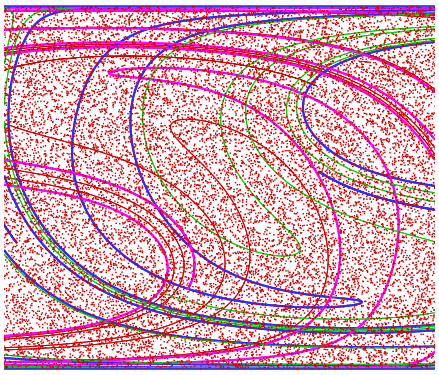

(c)

Figure 5.7: Invariant manifolds of the set of two hyperbolic points for (a) $\tau = 1.05$; (b) $\tau = 1.15$; (c) $\tau = 1.30$. Blue and green lines are the stable manifold of the lower and upper point and red and pink lines are the unstable manifolds of them respectively. They build the boundaries of the ghost rods; For $\tau = 1.05$ and 1.15 there is one elliptic point surrounded by an elliptic island at each side of the center of the ghost rod but there is no visible island for $\tau = 1.3$.

$\tau = 1.05$ was studied in the previous section. This structure leads to the minimum rate of mixing. The decay diagram clearly consists of two parts with different rates. As τ increases, the decay becomes faster but the two-rate decay is seen in a smoother shape for $\tau < 1.15$. For $\tau = 1.2$ the bent does not exist anymore and for $\tau = 1.3$ the homogenization is pure exponential.

A natural question here is: what does happen to the lobes when τ changes? Homogenization of the scalar for $\tau = 1.15$ can be compared to that for $\tau = 1.05$ in Fig. 5.2. The structure of the ghost rod is similar. However the scalar enters this area smoothly without slowing down the homogenization. In other words the AIS is bigger but leakier for larger τ (Fig. 4.7). The pair of hyperbolic points exist for $1 < \tau < 1.3$. They are born at $\tau = 1$ with a zero-distance between them. As τ increases, they separate more. Their location can be seen in Fig. 5.7 at the intersection of the invariant manifolds. It is evident that as the periodic points move away from each other, the lobes get larger. Also as the ghost rods grow, the lobes between regions R_2 and R_3 (two sides of a ghost rod) play a more important role in mixing inside this big region. A comparison to the homogenization images makes it clear that larger lobes facilitate the mixing by making the AIS leakier. See table 5.1 for a comparison of lobe areas. As illustrated in the previous section, the rate of transport of the scalar in and out of the AIS depends on the size of the lobes. The 'communication' between the two AIS through large lobes does not slow down the mixing so that a pure exponential homogenization is observed for $\tau \geq 1.3$.

5.3 Slow decay of concentration variance due to lobe dynamics

It has been shown theoretically that in the case of a fully hyperbolic phase space and considering the existence of diffusion, concentration variance decays exponentially with time [54]. However, as CV diagrams for the rod-stirring systems (chapter 3)

and the cavity flow (chapter 4) show, in most cases the decay rate is not exponential and ranges from pure exponential to slower than algebraic. Gouillart *et al.* [30] argue that for the mixing systems where the boundary of the fluid domain is stationary if the chaotic region is extended to the wall, under the no-slip boundary condition the homogenization slows down. The parabolic periodic point at the wall slows down the dynamics and this slow dynamics contaminates the whole domain. As a result the decay of concentration variance is algebraic. This is related to an important distinction between the 4-rod system A and the 3-rod system B of section 3.2. In the 3-rod system the chaotic region is extended up to the boundary of the domain which is a no-slip wall, while in the 4-rod system a regular ring isolates the chaotic region from the boundary. Poincaré section of system B shows that the fluid particles close to the wall exhibit slow, close-to-regular motion (Fig. 3.14, the first row). In such systems, poorly stretched fluid particles are pulled down into the core of the domain along the unstable manifold of a parabolic periodic point (fixed point of the Poincaré map). This phenomenon generates the "parabolic injection cusp" [72] which can be seen in Fig. 3.14 for system B. Fig. 3.8 shows that decay of the concentration variance is close to algebraic. The injection cusps in system A is hyperbolic, therefore it does not suffer from the decelerating effect of the no-slip wall. Still as it can be seen in Fig. 2.5 the stirring itself does not exhibit an exponential decay. Hence we predict the possibility of other sources causing a slower than exponential decay of concentration variance.

Similarly, our observations of mixing in the cavity flow of this chapter showed that in the range of $1 < \tau < 1.2$ the homogenization is sub-exponential while the no-slip wall argument does not apply here either. The vertical boundaries of the cavity flow are not no-slip walls because they are streamlines of the flow and there is no parabolic point associated with them. The horizontal boundaries are no-slip walls but they are not stationary so that there is no slow dynamics associated with them either. The absence of stationary no-slip walls makes it possible to have exponential

homogenization for a large range of τ as CV diagrams of section 4.3.2 illustrate. In section 4.5 the sub-exponential homogenization of $1 < \tau < 1.2$ is associated with the high-eigenvalue almost cyclic region surrounding the periodic points. Through the AIS analysis, slow-dynamic areas around the periodic points can be detected that slow down the mixing in the whole domain.

Lobe dynamics analysis of this chapter explained these observations through calculation of the rate of transport. For $1 < \tau < 1.2$ the particular structure of the invariant manifolds of the periodic points that are the boundaries of the AIS, make the transport and communication between the two dominant AIS slow. Hence when the scalar reaches the vicinity of the periodic points and boundaries of the 'hard' ghost rods, the communication between this region and the rest of the domain contaminates the mixing in the entire domain with the slow transport. The decay gradually grows for $\tau > 1.05$ when the periodic points move away from each other causing the lobes to get larger. For $\tau = 1.3$, the decay approaches an exponential trend and the eigenvalue is low while the periodic points still exist. The particular configuration of hyperbolic periodic points causing particular shapes and sizes of lobes acts as another cause of sub-exponential homogenization in some chaotic laminar flows while stationary no-slip walls are absent.

6

Protocol optimization based on the homogenization of a scalar

A fluid mixing system can be optimized for achieving different objectives or minimizing different cost functions that can be defined based on a variety of mixing measures. For example, the objective can be obtaining the highest stretching rate or entropy [24, 76, 63], fastest or maximum homogenization [8, 47, 74, 42] or smallest regular area that is possible for the system (See section 3.1.4 where the size of islands is minimized by varying the geometry of the 3-rod example systems). The objective can be defined in terms of minimizing a cost function, for example the energy (section 3.1.4) or time expenditure or the number of operations [24] needed to get a specific rate of stretching or homogenization.

The parameter or property of system that is tuned to find the optimized state also varies in different methods. It can be the fluid velocity field [47], the geometry (e.g. in [34]) or topology of motion of the stirrers [24], location of the initial blob of passive particles or the initial distribution of the two mixing fluids that gives the optimum mixing.

The third important aspect of an optimization scheme is the constraints and limitations that are imposed by the mixing system or the application. For example, the stirring protocols can be limited geometrically or topologically, the distances between rods and boundaries (which is related to amount of the generated shear stress in the

fluid) may be constrained by lower or upper bounds and the number of rods may be limited.

The stretching rate of material lines (or equivalently the topological entropy) can be a criteria if the objective of the system is generating the fastest possible stretching. Finn *et al.* [24] optimize n-rod stirring systems from a topological point of view i.e. based on the theoretical value of topological entropy obtained from the braiding. They use two different cost functions to find the optimum topology of motion of n stirring rods. The first one is the number of generators (braid letters as defined in sections 1.3 and 3.1). In this case the optimized protocol is the one generating the largest topological entropy per braid letter which, as it is proven in [24], has the maximum value of the logarithm of the golden ratio: $\log(\frac{1+\sqrt{5}}{2})$. Second cost function used in that work is the number of operations defined as follows: when different braid generators are accomplished simultaneously, they are counted as a single operator. In this case the optimized protocol is the one generating the largest topological entropy per operation which is proved to have the maximum value of the logarithm of the silver ratio: $\log(1+\sqrt{2})$.

In [46], homogenization of a passive scalar advected by a Stokes flow is the objective of mixing optimization. The velocity field is induced by a finite set of spatially distributed force fields. Using an optimal control approach, the authors look for the optimum force field that gives the lowest action integral (time integral of the kinetic energy of the fluid body). The mixing measure used in this study is the mix-norm reported in chapter 2.

This chapter studies the problem of optimization that looks for the optimum sequence of a finite set of stirring sub-protocols (the parameter to be tuned) that give the fastest homogenization of an initially condensed box of passive particles (the objective). Since the sequence of sub-protocols defines a mixing protocol in overall, this procedure can be called a protocol optimization. When the objective of a mixing device is homogenizing the mixture, the system's performance can be evaluated using

a concentration-based measure like the concentration variance (CV) or the mix-norm (chapter 2). Only the CV is measured in this study but it is straightforward to generalize the approach to any concentration-based measure. CV is equivalent to the cost function which its value is aimed to be minimized for a predefined number of sub-protocols. As an example the method is performed on the 3-rod system of chapter 3. However, the approach is applicable to any mixing system that its protocol can be formed from a sequence of sub-protocols. The sequence is tuned to give the optimum mixing based on the chosen mixing measure.

6.1 Protocol optimization for the 3-rod system

For a stirring flow, the rates of stretching and homogenization change spatially (Fig. 6.1). In other words a protocol has different stirring effects on different points in the fluid domain. When there is the option to choose from different possible protocols, a good choice depends on the spatial distribution of the scalar at that specific instant of time. It is possible to apply this fact to optimize the stirring protocols in several ways, two of which are explained here and applied to the main 3-rod system of chapter 3 as a case study.

Suppose a stirring device is capable of performing any protocol (sub-protocol) form a set of n different protocols so that in a specific time interval $\triangle t$, the system obeys only one of them. For the next time interval again one of the sub-protocols is chosen. In the *basic optimization scheme*, based on the distribution of the passive scalar at any time step the sub-protocol that will result in a more homogenous state (according to a measure of homogenization) over the next time step is selected. Continuing this procedure for a finite number of time steps gives an overall stirring protocol for the mixing system. The *comprehensive optimization scheme* calculates a measure of homogenization for every possible overall protocol composed from the set of n sub-protocols and finds the combination that gives the most homogenous state.

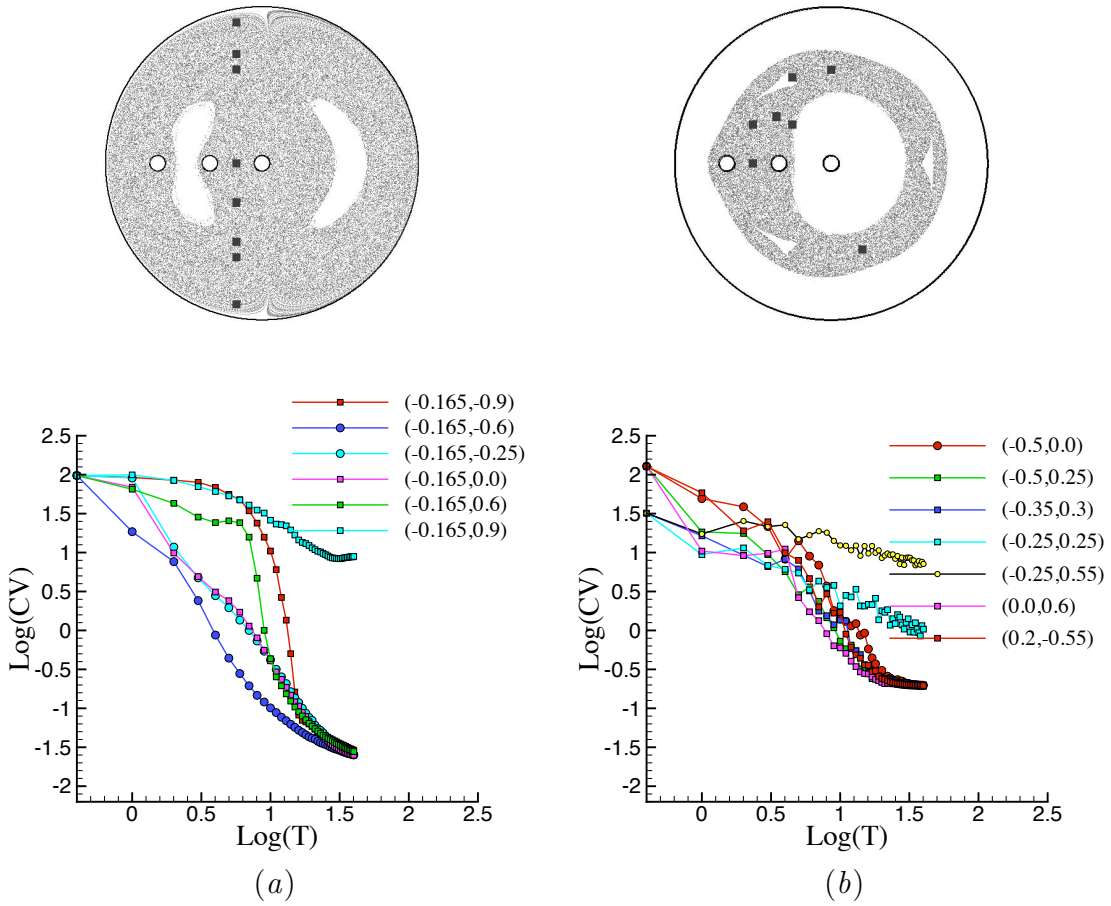

Figure 6.1: Effect of initial distribution of the scalar on the CV calculation for the sub-protocols (a) $PA1$ and (b) $FO1$. The legends on the CV diagrams indicate the initial location of the box of passive particles for each curve. The center of the domain is located at the origin and the domain's radius is 1.

The following problem is proposed to study how this approach works in optimizing the topology of motion of a 3-rod device. However the method and the whole procedure is applicable to any fluid flow which is capable of switching between different velocity fields in the process of mixing.

Suppose a 3-rod mixing device consists of the same mechanism as $PA1$ and $FO1$ of sections 3.1.1 and 3.1.3 (Fig. 6.1). One rod is fixed at the center of the domain. Another rod rotates clockwise on a circular path with its center of rotation located on the right side of the center. Center of rotation of the third rod is located on the left side of the fixed rod; however at the beginning of any period, $t = kT\ k = 0, 1, 2,$ there is the option to rotate it clockwise (as in the $FO1$ protocol) or counter-clockwise (as in the $PA1$ protocol). This option over several periods of stirring gives the sequence $P^{n1}F^{m1}P^{n2}F^{m2}$ in which P and F represent the $PA1$ and $FO1$ protocols and $n1, n2,$ and $m1, m2,$ can be any integer. The aim is to find the optimum set of integers $\{n1, n2, m1, m2, ...\}$ so that $n1 + n2 + ... + m1 + m2 + ... = N_p$, the total number of sub-protocols in the overall mixing protocol.

For the basic optimization scheme, the criterion for selection of P or F at any step is choosing the one that gives a more homogenous state after the next sub-period of the flow. To measure the homogenization, the concentration variance is evaluated using the Ulam matrix as explained in section 2.3. For this, we need to calculate the Ulam matrices for one period of the flow for each of these protocols: M_F and M_P. The concentration vector, $C = \{c_1, c_2, ..., c_{N_b}\}$, evolves as $C_{t+T} = M_F.C_t$ or $C_{t+T} = M_P.C_t$ based on the chosen protocol at time t. The resulting homogenization is then evaluated using the variance of elements of resulting concentration vector: $CV = \frac{1}{N_b}\Sigma_i^{N_b}(c_i - \bar{c})^2$.

The protocol resulting the lowest CV will be selected for this step of stirring. The final result of this optimization for a finite number of steps (sub-periods), N_p, is an overall mixing protocol. Fig. 6.2 and tables 6.1 through 6.3 show the results of this procedure for $N_p = 20$ for 3 different initial conditions.

For the comprehensive optimization, suppose a final protocol of N_p length is desired. A computer program is implemented which calculates $CV(N_p)$ (CV after N_p sub-periods) for every possible sequence $P^{n1}F^{m1}P^{n2}F^{m2}...$ so that $n1+n2+...+m1+m2+...=N_p$. $CV(N_p)$ is equal to the variance of the elements of the final concentration vector $(M_P^{n1}M_F^{m1}M_P^{n2}M_F^{m2}...).C_0$. Since in this example, there are two choices of sub-protocols (i. e. P and F), for an overall protocol including N_p sub-protocols ($P^{n1}F^{m1}P^{n2}F^{m2}...$), there are 2^{N_p} possibilities. For all i form 0 to $2^{N_p}-1$, protocol i consists of the sequence $p_1p_2p_3...p_{N_p}$ where p_j can be P or F protocol. To implement the search for the optimum protocol, this program uses base-2 (binary) numbers as indicators of the braid words for each possible overall protocol. For each i, it finds the binary number $(a_1a_2a_3...a_{N_p})_2 = i$ and considers $p_j = P$ if $a_j = 0$ and $p_j = F$ if $a_j = 1$. Then $CV(N_p)$ is calculated for each possible sequence $i, i = 0, 1, ..., 2^{N_p}-1$. The sequence giving the minimum $CV(N_p)$ is the optimum protocol.

Here is the example for $N_p = 3$; i.e. the procedure implemented to find the optimum sequence of $PA1$ and $FO1$ protocols with a total length of 3 sub-periods. There are $2^3 = 8$ possible overall protocols with a length of 3. They can be written in the form of base-2 numbers:

i (possibility)	i in binary form	Protocol	$CV(3)$
0	000	PPP	0.0055
1	001	PPF	0.0084
2	010	PFP	0.0136
3	011	PFF	0.0210
4	100	FPP	0.0826
5	101	PFP	0.0371
6	110	FFP	0.0636
7	111	FFF	0.0351

The last column shows CV after implementing the corresponding overall protocol on the same initial concentration with $CV(0) = 1$. Thus the optimum protocol for $N_p = 3$ for this choice of initial concentration is PPP with a final CV of 0.0055.

For larger N_p the total number of possibilities, 2^{N_p}, quickly becomes very large and the computation becomes heavy. Concentration calculation via Ulam matrix makes

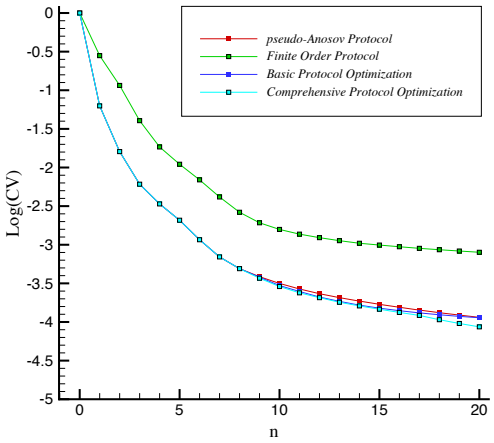

(IC_1)

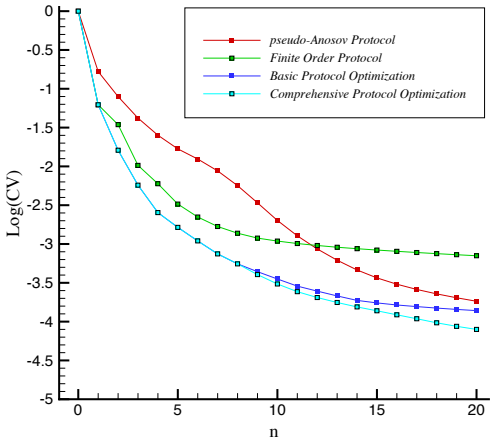

(IC_2)

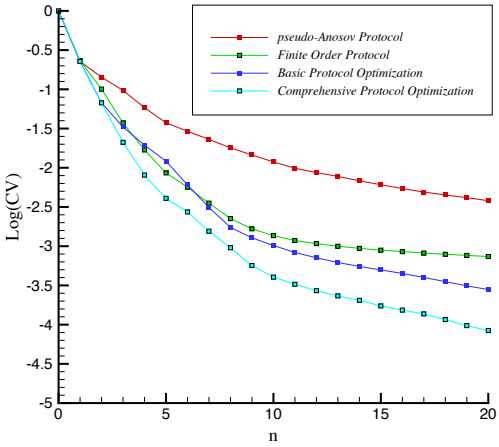

(IC_3)

Figure 6.2: CV diagrams showing the result of using the $PA1$ protocol, $FO1$ protocol, the protocol obtained from the basic optimization scheme and the protocol obtained from the comprehensive optimization scheme. Note that for each number of sub-periods (N_p) the comprehensive scheme gives a different overall protocol (see tables 6.1 through 6.3). The initial location of the scalar is $(-0.1, -0.6)$ for (IC_1), $(0, 0.5)$ for (IC_2) and $(-0.5, 0.25)$ for (IC_3).

this huge computation possible. Once the Ulam matrix for the primary protocols P and F are known, it is enough to multiply the corresponding matrices with the desired sequence and calculate the variance of the entries of the resulting concentration vector. Fig. 6.2 and tables 6.1 through 6.3 show the results of this procedure for $N_p = 1, 2, ..., 20$ (length of the overall protocol) for 3 different initial conditions.

Results of both basic and comprehensive optimization procedures depend on the initial concentration distribution, $\mathbf{C_0}$. Obviously the first choice of P or F sub-protocol depends on this distribution. Fig. 6.1 shows that each sub-protocol can perform strong or weak based on the initial distribution (See section 3.1.2 for details.). There are islands in different locations and the dynamics can be slow or fast in different regions of the space. For the same reason, the distribution of the scalar and the choices of the sub-protocols at the subsequent time steps also vary for different initial distribution.

The comprehensive optimization always leads to the minimum CV since it is not possible to get a lower CV under the problem's conditions. Therefore, it can be used as a base for evaluation of other results.

A protocol composed of only the finite order sub-protocol gives similar results for different choices of initial location of the scalar provided this location is not inside the regular region. The scalar gets homogenized inside the relatively small chaotic area with similar rates for different initial distributions. Noting that the use of Ulam matrix for concentration calculation allows for some diffusion in these computations, after this stage a slow decay of CV continues via diffusion both inside and outside the regular region. For 20 sub-periods of stirring, the resulting CV is about one order of magnitude larger than the optimized protocol.

A protocol composed of only the pseudo-Anosov protocol, as we also confirmed in the diffusion-free discussions of chapter 3, generally leads to smaller CV values than the finite order protocol. However despite the robustness in stretching results, the rate of homogenization varies and, as Fig. 6.2 shows, can be close to or far from

the optimum case. The third set of results corresponds to a scalar that is initially located in an elliptic island of $PA1$'s Poincaré section. This clearly makes the mixing performance considerably poor even in the presence of diffusion.

The fact that results of the basic optimization scheme are not globally optimum is worth investigating. This shows that in order to get the optimum $CV(N_p)$, the system needs to generate a state at the previous periods ($n < N_p$) that could be less homogenous than the maximum possible homogeneity for n. In other words, if $N_{p1} < N_{p2}$, in general the optimum protocol for N_{p1} periods cannot be used to get the optimum results for N_{p2} periods. However, the results of the basic optimization for the first and second initial conditions are fairly close to the optimum results. Initiating the scalar in the regular region of $PA1$ in the third case, affected the results of this optimization scheme as well. Noting the much higher cost of a comprehensive optimization procedure, it can be said that the 'basic' scheme is a reasonable approach if the scalar is not initially located in the islands of any of the sub-protocols.

This optimization procedure and the written program can be easily generalized to a bigger number of sub-protocols (choices of stirrer motions). If there were n choices of sub-protocols one would need to use base-n numbers to cover all the possibilities in order to search for the optimum sequence. It is also straightforward to use the procedure for other types of mixing systems. For a flow that the velocity field can be altered practically by changing the boundary conditions at specific time intervals, the Ulam matrix for the implementation of each velocity field over the time interval can be calculated. Then different overall protocols are constructed by different choices of sequence of the velocity fields and the optimum protocol can be found. Different concentration-based measures of mixing also can be employed. Once the concentration vector is determined using the appropriate Ulam matrix multiplications, computing any of these measures is straightforward.

Table 6.1: The optimum protocol obtained from the comprehensive optimization scheme for $N_p = 1$ to 20 sub-periods and the basic optimization scheme for $N_p = 20$ sub-periods for the first initial condition, IC_1.

N_p	Optimum protocol
1	P
2	P P
3	P P P
4	P P P P
5	P P P P P
6	P P P P P P
7	P P P P P P P
8	P P P P P P P P
9	P P P P P P P F F
10	P P P P P P P F F F
11	P P P P P P P F F F F
12	P P P P P P P F F F F F
13	P P P P P P P P F F F F P
14	P P P P P P P P P F P P F F
15	P F P P P P P P P P P P P F F
16	P F P P P P P P P P P P P P F F
17	P F P P P F P P P P P P P P P F F
18	P F P P P F P P P P P P P P P F F F
19	P F P P P F P P P P P P P P P P F F F
20	P F P P P F P P P P P P P P P P F F F F
Basic Opt.	P P P P P P P P F P F F F F F F F F F F

Table 6.2: The optimum protocol obtained from the comprehensive optimization scheme for $N_p = 1$ to 20 sub-periods and the basic optimization scheme for $N_p = 20$ sub-periods for the second initial condition, IC_2.

N_p	Optimum protocol
1	F
2	F P
3	F P P
4	F P P P
5	F P P P P
6	F P P P P P
7	F P P P P P P
8	F P P P P P P P
9	F F P P P P P F F
10	F F P P P P P P P F
11	F F P P P P P P P F P
12	F F P P P P F P P P P P
13	F F P P P P F P P P P F F
14	F F P P P P F P P P P P F F
15	F F P P P P P P P P P F F F
16	F F P P P F P P P P P P P F F
17	F F P P F P P P P P P P P F F F
18	F F P P F P P P P P P P P F F F F
19	F F P P F P P P P P P P P F F F F F
20	F F P P F P P P P P P P P F F F F F F
Basic Opt.	F P P P P P P P F F F F P F F F F F F

Table 6.3: The optimum protocol obtained from the comprehensive optimization scheme for $N_p = 1$ to 20 sub-periods and the basic optimization scheme for $N_p = 20$ sub-periods for the third initial condition, IC_3.

N_p	Optimum protocol
1	P
2	P F
3	F P P
4	F P P P
5	F P P P P
6	F P P P P P
7	F P P P P P P
8	F P P P P P P P
9	F P P P P F P P P
10	F P P P P F P P P P
11	F P F P P P P P P F F
12	F P F P P P P P P F F F
13	F P F P P P P P P F F F F
14	P F F F P P P P F P P P F F
15	P F F F P P P P P P F F F F P
16	P F F F P P P P P P F F F F P F
17	P F F F P P P P F P P P P F F F F
18	P P F P P P F P P P P P P P F F F F
19	P P F P P P F P P P P P P P F F F F F
20	P P F P P P F P P P P P P P F F F F F F
Basic Opt.	P F P P F P P P F F P P F P P P P P P P

7

Conclusions

As a progressively more popular and well-known method of mixing in laminar flows of various types, this dissertation discusses about using chaotic advection [3, 4] to mix low-Reynolds-number flows. This work contains observations of the relationship between line stretching (chaos) and scalar homogenization (mixing) as well as the extent to which the topological approach of Thurston-Nielsen (TN) theory can be practically used in the design and analysis of mixing systems. This is accomplished through study of line stretching and scalar homogenization in Stokes flows using:

- Topological chaos theory and TN theorem; braiding of the flow with rods and ghost rods,
- Numerical and experimental simulation of stretching and homogenization,
- Chaos measures (Lyapunov exponents and stretching rates) and mixing measures (concentration variance) with and without diffusion consideration,
- Sets: Almost Invariant Sets,
- Invariant manifolds: lobe dynamics,
- Optimization of stirring protocols based on the Ulam-matrix method of concentration calculation.

A recent and great development in this field is using Thurston-Nielsen (TN) theory to explain the chaos built in the flow based on the topology of boundary motions without considering details of the involving fluid mechanics [9]. This way the stretching

rate of material lines are analyzed and predicted both qualitatively and quantitatively from a topological point of view. In chapter 3, the practical application of TN theorem is studied in rod-stirring systems that are extracted from industrially common protocols. Comparing the theoretical predictions of topological chaos theory to numerical and experimental flow simulations, the practical implementation of the topological view in the design and optimization of an n-rod mixer is examined. It is illustrated that even though tuning the geometric parameters of the finite order protocol can lead to a surprisingly fast and energy-efficient mixing in systems deemed trivial (finite order) by TN theorem, the mixing characteristics are not robust. Perturbations change the stretching and mixing characteristics of these systems significantly so that the same topology can generate a very small chaotic region or make the entire domain chaotic and it can produce a fast or slow homogenization inside the chaotic region. This mainly happens because the stretching and mixing depend on the periodic orbits (ghost rods) of the flow which themselves depend on the details of fluid dynamics. On the other hand, in the protocols called Pseudo-Anosov by TN theorem, the mixing characteristics are mainly defined by the topology of motion of the solid rods, therefore they are more consistent and robust as long as the topology of motion is preserved. Overall comparison of the results shows that in average, the pseudo-Anosov systems show a more efficient mixing in terms of the final accessible homogenization, size of the mixing region (chaotic sea), the speed of homogenization and energy consumption. The study confirms that even though the periodic points are important players in producing complexity along with the solid rods, examining the topology of motion of (only) solid rods using the TN classification theorem prior to the numerical simulation of the fluid flow is greatly advantageous in the selection of appropriate mixing protocols.

In chapter 4, using a variation of the lid-driven cavity flow as an example system, the relationship between the stretching of material lines (chaos) and the homogenization of a scalar (mixing) in chaotic Stokes flows is examined. This study illustrated

the extent to which the stretching as a common chaos measure can be representative of real mixing. A remarkable correspondence between the decay of concentration variance and the time-rate of stretching is observed. This implies that prediction of the amount of stretching using the powerful TN classification theorem only based on the topology of motion of the stirrers can be considered as a practical indicator of the quality of mixing and a framework for analysis and design of chaotic-mixing systems. Once the parameters of the system are confined to a region of high stretching, the detailed design and optimization will need other more expensive tools, mainly by means of accurate simulation of scalar homogenization in the fluid flow.

In chapter 4 a set-oriented approach is used to describe the mixing. This approach proved to be an accurate method for prediction of mixing behavior of chaotic systems. A previous study [65] clarified that the almost invariant sets (AIS) are responsible for generating topological chaos in the double-lid-driven cavity flow especially when there are no periodic points performing as ghost rods. Here the leakiness of these AIS is found to be in a direct relationship with the rate of scalar homogenization. Highest rates of mixing is obtained when the stirrers are the leaky low-eigenvalue AIS instead of periodic points that are high-eigenvalue AIS. Rate of mixing closely follows the corresponding eigenvalue. Adding the fact that in the computation of the almost invariant sets it is necessary to track only less than 1% of the number of particles required for homogenization simulations, it is a considerably less expensive tool for study of mixing systems.

In chapter 5, the structure of these ghost rods and the variations of their behavior are explained based on transport via lobe dynamics [77]. Lobes are made of segments of invariant manifolds of the periodic points that are generators of the ghost rods. Using lobe dynamics, this chapter describes how the transport and homogenization of a scalar can be accurately modeled. This analysis uncovers some of the mystery of the AIS and ghost rods of the example system of chapter 4. It also explains the slow

mixing of some systems that otherwise are expected to follow the (fast) exponential trend.

In chapter 3, along with the discussions about the effect of geometric perturbations on a mixing protocol, a fixed topology of motion of physical rods is geometrically optimized. The resulting protocol produces adequate mixing in a rod-stirring system, i.e. negligible regular (unmixed) areas and fast decay of concentration variance while the energy consumption is kept at low levels. Chapter 6 presents two schemes for topological optimization of mixing protocols. These schemes can be used for a broad variety of mixing systems. As an example system the 3-rod stirring system of chapter 3 is used to observe the performance of the protocol optimization schemes.

In order to evaluate the mixing systems, measures of chaos and homogenization should be employed. In chapters 3 and 4 the extent to which the theoretical and numerical measures of chaos and stretching represent the real mixing is evaluated by comparing them to measures of homogenization based on decay of a scalar concentration. Chapter 2 covers a variety of the concentration-based measures, their practical method of calculation and the important parameters in these calculations. The implicit effect of diffusion, as an important factor in mixing, is explained as well.

The studies, measures and methods of this dissertation help in evaluation and understanding of chaotic mixing systems in nature and in industrial applications. They provide theoretical and numerical grounds for selection of the appropriate mixing protocol and design and optimization of mixing systems, examples of which can be seen throughout the dissertation.

Bibliography

[1] R. L. Adler, A. G. Konheim, and M. H. McAndrew. Topological entropy. *Trans. Am. Math. Soc.*, 114:309–319, 1965. 9

[2] D. V. Anosov. *Topological entropy In: Encyclopaedia of Mathematics*. Springer, 2001. 9

[3] H. Aref. Stirring by chaotic advection. *J. Fluid Mechanics*, 143:1–21, 1984. 2, 3, 8, 35, 66, 118

[4] H. Aref. The development of chaotic advection. *Phys. Fluids*, 14:1315–1326, 2002. 2, 3, 118

[5] V. I. Arnold. *Mathematical methods of classical mechanics*. Springer-Verlog, 1982. 9

[6] D-W. Sun B. Xia. Applications of computational fuid dynamics (cfd) in the food industry: a review. *Computer and Electronics in Agriculture*, 34:5–24, 2002. 1

[7] D. Beigie, A. Leonard, and S. Wiggins. Invariant manifold templates for chaotic advection. *Chaos, Solitons, Fractals*, 4:749–868, 1994. 12, 90

[8] F. Bottausci1, I. Mezic1, C. D. Meinhart1, and C. Cardonne. Mixing in the shear superposition micromixer: three-dimensional analysis. *Phil. Trans. R. Soc. Lond. A*, 362:1001–1018, 2004. 106

[9] P.L. Boyland, H. Aref, and M.A. Stremler. Topological fluid mechanics of stirring. *J. Fluid Mechanics*, 403:227–304, 2000. 4, 5, 6, 7, 32, 51, 63, 69, 86, 118

[10] J. P. Brody, P. Yager, R. E. Goldstein, and R. H. Austin. Biotechnology at low reynolds numbers. *Biophysical Journal*, 71:3430–3441, 1996. 1, 2

[11] C. M. Caruana. Micromixing creates a stir. *Chem. Eng. Prog.*, 96.(5):9–10, 2000. 2

[12] H. Chen and J. C. Meiners. Topologic mixing on a microfluidic chip. *Appl. Phys. Lett.*, 84:2193–2196, 2004. 2

[13] J. Chen. *Topological chaos and mixing in lid-driven cavities and rectangular channels*. PhD thesis, Virginia Tech, Blacksburg, Virginia, 2008. 4, 8

[14] J. Chen and M. A. Stremler. Topological chaos and mixing in a three-dimensional channel flow. *Physics of Fluids*, 21:021701, 2009. 7

[15] W-L. Chien, H. Rising, and J. M. Ottino. Laminar mixing and chaotic mixing in several cavity flows. *J. Fluid Mech.*, 170:355–377, 1986. 3, 4

[16] C. Coulliette and S. Wiggins. Intergyre transport in a wind-driven, quasi-geostrophic double gyre: An application of lobe dynamics. *Nonlinear Processes in Geophysics*, 8:69–94, 2001. 12, 91

[17] E. Henry D. Rothstein and J.P. Gollub. Persistent patterns in transient chaotic fluid mixing. *Nature*, 401:770–772, 1999. 17

[18] P.V. Danckwerts. The definition and measurement of some characteristics of mixtures. *Appl. Sci. Res.*, A3:279–296, 1952. 10, 17, 63

[19] M. Dellnitz, O. Junge, W. S. Koon, F. Lekien, M. W. Lo, J. E. Marsden, K. Padberg, R. Preis, S. D. Ross, and B. Thiere. Transport in dynamical astronomy and multibody problems. *Int. Journal Bifurcation and Chaos*, 15:699–727, 2005. 12, 70, 91

[20] C.R. Doering and J.-L. Thiffeault. Multiscale mixing efficiencies for steady sources. *Phys. Rev. E*, 74:025301, 2006. 19

[21] V. Eswaran and S. B. Pope. Direct numerical simulations of the turbulent mixing of a passive scalar. *Phys. Fluids*, 31:506–521, 1988. 1

[22] J. Evans, D. Liepmann, and A. P. Pisano. Planar, laminar mixer. *Proceedings of MEMS97*, pages 96–101, 1997. 4

[23] M. D. Finn, S. M. Cox, and H. M. Byrne. Mixing measures for a two-dimensional chaotic stokes flow. *J. Eng. Math.*, 48:129–155, 2004. 10

[24] M. D. Finn and J-L Thiffeault. Topological optimization of rod-stirring devices. *SIAM Review*, to appear, 2011. 4, 7, 106, 107

[25] M. D. Finn, J.-L. Thiffeault, and E. Gouillart. Topological chaos in spatially periodic mixers. *Physica D*, 221:92–100, 2006. 4, 7

[26] M.D. Finn and S.M. Cox. Stokes flow in a mixer with changing geometry. *J. Eng. Math.*, 41:75–99, 2001. 8

[27] M.D. Finn, S.M. Cox, and H.M. Byrne. Topological chaos in inviscid and viscous mixers. *J. Fluid Mechanics*, 493:345–361, 2003. 4, 8, 35, 36, 47, 131, 132

[28] C. H. Gibson. Fine structure of scalar fields mixed by turbulence: I. zero-gradient points and minimal gradient surfaces. *Phys. Fluids*, 11:2305–2315, 1968. 1

[29] K. J. Gooch, J. H. Kwon, T. Blunk, R. Langer, L. E. Freed, and G. Vunjak-Novakovic. Effects of mixing intensity on tissue-engineered cartilage. *Biotechnology and Bioengineering Journal*, 72:402–407, 2000. 1, 2

[30] E. Gouillart, O. Dauchot, B. Dubrulle, S. Roux, and J.-L. Thiffeault. Slow decay of concentration variance due to no-slip walls in chaotic mixing. *Phys. Rev. E*, 78:026211, 2008. 4, 11, 17, 37, 40, 63, 64, 82, 93, 104

[31] E. Gouillart, J.-L. Thiffeault, and M. D. Finn. Topological mixing with ghost rods. *Phys. Rev. E*, 73:036311, 2006. 4, 7, 11, 43, 63, 64, 69

[32] H. S. Gurm and D. G. Wentzel. On mixing in stellar interiors caused by magnetic fields. *Astrophysical Journal*, 149:293–298, 1967. 1

[33] T. Hall. Department of mathematical sciences, university of liverpool, May 2000. `http://www.liv.ac.uk/maths/PURE/MIN`$_S ET/CONTENT/members/T_H all.html$.52

[34] D. M. Hobbs and F. J. Muzio. Optimization of a static mixer using dynamical systems techniques. *Chem. Eng. Sci.*, 53:3199–3213, 1998. 106

[35] T. J. Johnson, D. Ross, and L. E. Locascio. Rapid microfluidic mixing. *Anal. Chem.*, 74:45–51, 2002. 2

[36] C. Jones and S. Winkler. Invariant manifolds and lagrangian dynamics in the ocean and atmosphere. *Handbook of Dynamical Systems*, 2:55–92, 2002. 12, 91

[37] S. W. Jones and H. Aref. Chaotic advection in pulsed sourcesink systems. *Phys. Fluids*, 31:469–486, 1988. 4

[38] T. J. Kaper and S. Wiggins. An analytical study of transport in stokes flows exhibiting large-scale chaos in the eccentric journal bearing. *J. Fluid Mech.*, 253:211–243, 1993. 4, 12, 91

[39] H. Lamb. *Hydrodynamics*. Cambridge University Press, sixth edition, 1932. 8, 34

[40] C. W. Leong and J. M. Ottino. Experiments on mixing due to chaotic advection in a cavity. *J. Fluid Mech.*, 209:463–499, 1989. 4

[41] Mixing Solutions Limited. The markets we serve, December 2009. `http://www.mixingsolutions.com`. 1

[42] Z. Lin, J.-L. Thiffeault, and C. Doering. Optimal stirring strategies for passive scalar mixing. *J. Fluid Mech.*, To appear, 2011. 106

[43] R. H. Liu, M. A. Stremler, K. V. Sharp, M. G. Olsen, J. G. Santiago, R. J. Adrian, H. Aref, and D. J. Beebe. Passive mixing in a three-dimensional serpentine microchannel. *J. Microelectromechanical Systems*, 9:190–197, 2000. 3, 4

[44] N. Malhotra and S. Wiggins. Geometric structures, lobe dynamics, and lagrangian transport in flows with aperiodic time-dependence, with applications to rossby wave flow. *J. Nonlinear Sci.*, 8:401–456, 1998. 12, 91

[45] G. Mathew, I. Mezic, and L. Petzold. A multiscale mixing measure for mixing. *Physica D*, 211:23–46, 2005. 10, 11, 18, 19, 63

[46] G. Mathew, I. Mezic, and L. Petzold. Optimal control of mixing in stokes fluid flows. *J. Fluid Mech.*, 580:261–281, 2007. 19, 107

[47] G. Mathew, I. Mezic, R. Serban, and L. Petzold. Optimization of mixing in an active micromixing device. *NSTI-Nanotech*, 1:300–303, 2004. 106

[48] V. V. Meleshko and A. M. Gomilco. Infinite systems for a biharmonic problem in a rectangle: further discussion. *Proc. R. Soc. London, Ser. A*, 460:807, 2004. 66, 133

[49] V. V. Meleshko and A. M. Gomilko. Infinite systems for a biharmonic problem in a rectangle. *Proc. R. Soc. Lond.*, 460:807–819, 2004. 8

[50] J. M. Ottino. Mixing, chaotic advection and turbulence. *Annu. Rev. Fluid Mech.*, 22:207–253, 1990. 2, 3, 5

[51] J.M. Ottino. *The kinematics of mixing: stretching, chaos and transport.* Cambridge University Press, first edition, 1989. 2, 3, 5, 9, 12, 90

[52] Y. B. Pesin. Characteristic lyapunov exponents and smooth ergodic theory. *Russian Math. Sutveys*, 32:55–114, 1977. 9

[53] J. H. Phelps and C. L. Tucker. Lagrangian particle calculations of distributive mixing: Limitations and applications. *Chem. Eng. Sci.*, 61:6826, 2006. 10, 17, 20, 24, 63, 74

[54] R. T. Pierrehumbert. Tracer microstructure in the large-eddy dominated regime. *Chaos, Solitons and Fractals*, 4:1091–1110, 1994. 40, 75, 103

[55] A. C. Poje and G. Haller. Geometry of cross-stream mixing in a double-gyre ocean model. *J. Phys. Oceanogr.*, 29:1649–1665, 1999. 12, 91

[56] C. Rauwendaal. *Mixing in polymer processing.* CRC Press, 1991. 1, 2

[57] K. I. Read. Experimental investigation of turbulent mixing by rayleigh-taylor instability. *Physica D*, 12:45–58, 1984. 1

[58] V. Rom-Kedar, A. Leonard, and S. Wiggins. An analytical study of transport, mixing and chaos in an unsteady vortical flow. *J. Fluid Mech.*, 214:347–394, 1990. 12, 91

[59] V. Rom-Kedar and S. Wiggins. Transport in two-dimensional maps. *ARCHIVE FOR RATIONAL MECHANICS AND ANALYSIS*, 109:293–298, 1990. 12, 90

[60] H. Shaw, J.-L. Thiffeault, and C. Doering. Stirring up trouble: Multi-scale mixing measures for steady scalar sources. *Phys. D*, 231(2):141–164, 2007. 18

[61] M. K. Singh, T. G. Kang, H. E. H. Meijer, and P. D. Anderson. The mapping method as a toolbox to analyze, design, and optimize micromixers. *Microfluid. Nanofluid.*, 5:313–325, 2008. 23, 74

[62] M. A. Stremler and J. Chen. Generating topological chaos in lid-driven cavity flow. *Physics of Fluids*, 19:103602, 2007. 4, 7, 11

[63] M. A. Stremler and B. A. Cola. A maximum entropy approach to optimal mixing in a pulsed sourcesink flow. *Phys. Fluids*, 18:011701, 2006. 4, 106

[64] M. A. Stremler, F. R. Haselton, and H. Aref. Designing for chaos: applications of chaotic advection at the microscale. *Phil. Trans. R. Soc. Lond. A*, 362:1019–1036, 2004. 4

[65] M. A. Stremler, S. D. Ross, and P. Kumar P. Grover. Topological chaos and periodic braiding of almost-cyclic sets. *Phys. Rev. Let.*, to appear, 2011. xiv, 4, 7, 8, 11, 63, 64, 65, 69, 70, 71, 84, 85, 86, 120

[66] M.A. Stremler. Mixing measures. *Encyclopedia of micro- and nanofluidics*, pages 1376–1382, 2008. 3, 10, 17, 63

[67] S. H. Strogatz. *Nonlinear dynamics and chaos: with applications to physics, biology chemistry and engineering.* Addison Wesley, 1994. 9

[68] A. D. Stroock, S. K. W. Dertinger1, A. Ajdari, H. A. Stone I. Mezic, and G. M. Whitesides. Chaotic mixers for microchannels. *Science*, 295:647–651, 2002. 2, 3

[69] D. THERRIAULT, S. R. WHITE, and J. A. LEWIS. Chaotic mixing in three-dimensional microvascular networks fabricated by direct-write assembly. *Nature Materials*, 2:265–271, 2003. 4

[70] J.-L. Thiffeault. Measuring topological chaos. *Phys. Rev. Lett.*, 94:084502, 2005. 7, 9

[71] J.-L. Thiffeault. Topology, braids and mixing in fluids. *Phil. Trans. R. Soc. Lond. A*, 364:3251–3266, 2006. 7

[72] J.-L. Thiffeault, M. D. Finn, E. Gouillart, and Toby Hall. Topology of chaotic mixing patterns. *Chaos*, 18:033123, 2008. 7, 11, 104

[73] J.-L. Thiffeault, E. Gouillart, and M. D. Finn. The size of ghost rods. *CISM International Centre for Mechanical Sciences*, 510:339–350, 2009. 7, 11

[74] J.-L. Thiffeault and G. A. Pavliotis. Optimizing the source distribution in fluid mixing. *Chem. Eng. Sci.*, 57:2719–2725, 2002. 106

[75] Thurston. On the geometry and dynamics of dieomorphisms of surfaces. *Bull. Am. Math. Soc.*, 19:417–433, 1988. 5

[76] A. Vikhansky. Enhancement of laminar mixing by optimal control methods. *Chem. Eng. Sci.*, 57:2719–2725, 2002. 106

[77] S. Wiggins. *Chaotic transport in dynamical systems*. Springer-Verlag, first edition, 1991. 12, 13, 90, 91, 120

[78] S. Wiggins. *Introduction to applied nonlinear dynamical systems and chaos*. Springer, 2003. 12, 90

[79] S. Wiggins. The dynamical systems approach to lagrangian transport in oceanic flows. *Annu. Rev. Fluid Mech.*, 37:295–328, 2005. 12, 91

[80] S. Wiggins and J. M. Ottino. Foundations of chaotic mixing. *Phil. Trans. R. Soc. Lond. A*, 362:937–970, 2004. 7, 12, 90

[81] D. A. Zumbrunnen and S. Inamdar. Novel sub-micron highly multi-layered polymer films formed by continuous flow chaotic mixing. *Chem. Eng. Sci.*, 56:3893–3897, 2001. 4

Appendices

Appendix A

Numerical solution of the Stokes flow of a rod-stirring device with stationary outer boundary

The solution is adopted from [27] for the Stokes flow of rod-stirring device of Fig. 1.1 with a fixed outer boundary. The streamfunction $\psi(z, \overline{z})$ satisfies the biharmonic equation $\nabla^4 \psi = 0$. The solution satisfies the no-slip boundary conditions at the stationary outer boundary

$$u + iv = 0 \, on \, |z| = 1, \tag{A.1}$$

and on the boundary of the moving rods

$$u + iv = U_j + iV_j + i\Omega_j(z - p_j) \, on \, |z - p_j| = a_j, \tag{A.2}$$

where p_j, $U_j + V_j$ and Ω_j are the instantaneous location, translational velocity and angular velocity of the j^{th} rod in complex coordinates $j = 1, 2, ..., m$. A.1 is satisfied using the circle theorem for the biharmonic equation. Placing rotlet and Stokeslet singularities, and using the Laurent series, Finn *et al.* [27] obtain the following solution

for the streamfunction

$$\psi = \sum_{j=1}^{m} \left\{ b_{j,1} \left[\frac{1}{4}\overline{z} log \frac{q_j|z-p_j|^2}{p_j|z-q_j|^2} + \frac{|z|^2-a^2}{4|p_j|^2|z-q_j|^2}(\overline{p}_j\overline{z}(z-p_j) - a^2(\overline{z}+\overline{p}_j)) \right] \right.$$
$$\left. + \sum_{k=2}^{n} b_{j,k} \left[\overline{z}(z-p_j)^{1-k} + ((p_j+(k-1)z)\overline{z} - a^2k)(-p_j)^{-k}\overline{z}^k(\overline{z}-\overline{q}_j)^{-k} \right] \right\}$$
$$+ \sum_{j=1}^{m} \left\{ c_{j,1} \left[\frac{1}{4}\overline{z} log \frac{q_j|z-p_j|^2}{p_j|\overline{z}-\overline{q}_j|^2} + \frac{(|z|^2-a^2)(|z|^2-|q_j|^2)}{4a^2|z-q_j|^2} \right] \right.$$
$$\left. + \sum_{k=2}^{n} c_{j,k} \left[(z-p_j)^{1-k} + ((p_j+(k-1)z)\overline{z} - a^2k)(-p_j)^{-k}\overline{z}^{k-1}(\overline{z}-\overline{q}_j)^{-k} \right] \right\}, \tag{A.3}$$

in which over-bar means the complex conjugate. In order to avoid the singularity at the origin, the following constraint should be also imposed

$$Im \sum_{j=1}^{m} c_{j,1} = 0. \tag{A.4}$$

The velocity field can be calculated from the streamfunction using

$$u + iv = -2i\frac{\partial \psi}{\partial \overline{z}}. \tag{A.5}$$

The total power input to the stirring device is then determined by [27]

$$P = \sum_{j=1}^{m} (F_j^x U_j + F_j^y V_j + M_j \Omega_j), \tag{A.6}$$

in which F_j^x and F_j^y are the real and imaginary parts of the force F_j exerted by the j_{th} rod on the fluid that is readily given by

$$F_j = 4\pi\mu i b_{j,1}, \tag{A.7}$$

and M_j is the moment exerted by the j^{th} rod on the fluid given by

$$F_j = 4\pi\mu c_{j,1} - Im(F_j\overline{p}_j), \tag{A.8}$$

where μ is the dynamic viscosity of the fluid ad i is the imaginary unit.

Appendix B

Numerical solution of the Stokes flow of the double-lid-driven cavity flow

Following [48] an analytical solution for the velocity field can be found assuming a ψ of the form:

$$\psi(x,y,t) = \sum_{n=1}^{2}(U_n C_n f_n(y)\sin(\frac{n\pi}{a}(x+\phi))) \tag{B.1}$$

Plugging this into the biharmonic equation $\nabla^4\psi = 0$ leads to

$$C_n = \frac{a^2}{2n\pi^2 b}\left[\frac{a}{2n\pi b}\sinh(\frac{2n\pi b}{a})+1\right]^{-1}, \tag{B.2}$$

and

$$f_n(y) = \frac{2\pi y}{a}\cosh(\frac{n\pi b}{a})\sinh(\frac{n\pi y}{a}) - \frac{2\pi b}{a}\sinh(\frac{n\pi b}{a})\cosh(\frac{n\pi y}{a}). \tag{B.3}$$

Then the velocity field is obtained from

$$u(x,y,t) = \frac{\partial\psi}{\partial y} = \sum_{n=1}^{2}\left\{U_n C_n \frac{2\pi}{a}\sin(\frac{n\pi}{a}(x+\phi))\Big[\cosh(\frac{n\pi b}{a})\sinh(\frac{n\pi y}{a}) + \frac{2n\pi^2}{a^2}\cosh(\frac{n\pi b}{a})\cosh(\frac{n\pi y}{a}) - \frac{2n\pi^2 b}{a^2}\sinh(\frac{n\pi b}{a})\sinh(\frac{n\pi y}{a})\Big]\right\}, \tag{B.4}$$

and

$$v(x,y,t) = -\frac{\partial\psi}{\partial x} = -\sum_{n=1}^{2}\left\{\frac{n\pi}{a}U_n C_n f_n(y)\cos(\frac{n\pi}{a}(x+\phi))\right\}. \tag{B.5}$$